# Chapter 4

# Turbulence Energy Equation Models

As computers have increased in power since the 1960's, turbulence models based upon the equation for the turbulence kinetic energy have become the cornerstone of modern turbulence modeling research. This chapter discusses two types of turbulence energy equation models, viz., **One-Equation Models** and **Two-Equation Models**, with most of the emphasis on the latter. These models both retain the Boussinesq eddy-viscosity approximation, but differ in one important respect. One-equation models are **incomplete** as they relate the turbulence length scale to some typical flow dimension. By contrast, two-equation models provide an equation for the turbulence length scale or its equivalent and are thus **complete**.

The chapter begins with a derivation and discussion of the turbulence energy equation. We proceed to a general discussion of one-equation models including examples of how such models fare for several flows. Next, we introduce two-equation models with specific details of the two most commonly used models. Our first applications are to the same free shear flows considered in Chapter 3. Then, our attention focuses upon a very powerful tool, singular perturbation theory, that we use to analyze model-predicted features of the turbulent boundary layer. We apply the two-equation model to attached wall-bounded flows and compare to corresponding algebraic-model predictions. We discuss the issue of asymptotic consistency approaching a solid boundary, and the ability of two-equation models to predict transition from laminar to turbulent flow. Our final applications are to separated flows. The concluding section discusses the range of applicability of one- and two-equation models.

## 4.1 The Turbulence Energy Equation

Turbulence energy equation models have been developed to incorporate nonlocal and flow history effects in the eddy viscosity. Prandtl (1945) postulated computing a characteristic velocity scale for the turbulence, $v_{mix}$, thus obviating the need for assuming that $v_{mix} \sim \ell_{mix}|\partial U/\partial y|$ [c.f. Equation (3.15)]. He chose the kinetic energy (per unit mass) of the turbulent fluctuations, $k$, as the basis of his velocity scale, i.e.,

$$k = \frac{1}{2}\overline{u_i' u_i'} = \frac{1}{2}(\overline{u'^2} + \overline{v'^2} + \overline{w'^2}) \tag{4.1}$$

Thus, in terms of the density, $\rho$, a turbulence length scale, $\ell$, and $k$, dimensional arguments dictate that the eddy viscosity is given by

$$\mu_T = \text{constant} \cdot \rho k^{1/2} \ell \tag{4.2}$$

Note that we drop subscript "mix" in this chapter for convenience, and to avoid confusion with the mixing length used in algebraic models.

The question now arises as to how we determine $k$. The answer is provided by taking the trace of the Reynolds stress tensor, which yields the following.

$$\tau_{ii} = -\rho\overline{u_i' u_i'} = -2\rho k \tag{4.3}$$

Thus, the trace of the Reynolds stress tensor is proportional to the kinetic energy per unit volume of the turbulent fluctuations. The quantity $k$ should strictly be referred to as **specific turbulence kinetic energy** ("specific" meaning "per unit mass"), but is often just called **turbulence kinetic energy**.

In Chapter 2 we derived a differential equation describing the behavior of the Reynolds stress tensor, $\tau_{ij}$, i.e., Equation (2.34). We can derive a corresponding equation for $k$ by taking the trace of the Reynolds stress equation. Noting that the trace of the tensor $\Pi_{ij}$ vanishes for incompressible flow, contracting Equation (2.34) leads to the following **transport equation** for the turbulence kinetic energy.

$$\rho\frac{\partial k}{\partial t} + \rho U_j \frac{\partial k}{\partial x_j} = \tau_{ij}\frac{\partial U_i}{\partial x_j} - \rho\epsilon + \frac{\partial}{\partial x_j}\left[\mu\frac{\partial k}{\partial x_j} - \frac{1}{2}\rho\overline{u_i' u_i' u_j'} - \overline{p' u_j'}\right] \tag{4.4}$$

The quantity $\epsilon$ is the **dissipation per unit mass** and is defined by the following correlation.

$$\epsilon = \nu\overline{\frac{\partial u_i'}{\partial x_k}\frac{\partial u_i'}{\partial x_k}} \tag{4.5}$$

The various terms appearing in Equation (4.4) represent physical processes occurring as the turbulence moves about in a given flow. The sum

of the two terms on the left-hand side, i.e., the **unsteady term** and the **convection**, is the familiar Eulerian derivative of $k$ that gives the rate of change of $k$ following a fluid particle. The first term on the right-hand side is known as **Production**, and represents the rate at which kinetic energy is transferred from the mean flow to the turbulence. Rewritten as $\tau_{ij}S_{ij}$, this term is seen to be the rate at which work is done by the mean strain rate against the turbulent stresses. **Dissipation** is the rate at which turbulence kinetic energy is converted into thermal internal energy, equal to the mean rate at which work is done by the fluctuating part of the strain rate against the fluctuating viscous stresses. The term involving $\mu\partial k/\partial x_j$ is called **Molecular Diffusion**, and represents the diffusion of turbulence energy caused by the fluid's natural molecular transport process. We refer to the triple velocity correlation term as **Turbulent Transport**, and regard it as the rate at which turbulence energy is transported through the fluid by turbulent fluctuations. The last term on the right-hand side of the equation is called **Pressure Diffusion**, another form of turbulent transport resulting from correlation of pressure and velocity fluctuations.

The unsteady term, convection and molecular diffusion are exact while production, dissipation, turbulent transport and pressure diffusion involve unknown correlations. To **close** this equation, we must specify $\tau_{ij}$, dissipation, turbulent transport and pressure diffusion.

The conventional approach to closure of the $k$ equation was initiated by Prandtl (1945) who established arguments for each term in the equation. This term-by-term modeling approach amounts to performing **drastic surgery** on the exact equation, replacing unknown correlations with closure approximations. This process is by no means rigorous. The closure approximations are no better than the turbulence data upon which they are based. Our hope is that we can find universally valid closure approximations that make accurate solutions possible. We will discuss this point in greater detail when we introduce two-equation models.

**Reynolds-Stress Tensor:** For the class of turbulence models considered in this chapter, we assume the Boussinesq approximation is valid. Thus, we say that the Reynolds stress tensor is given by

$$\tau_{ij} = 2\mu_T S_{ij} - \frac{2}{3}\rho k\delta_{ij} \tag{4.6}$$

where $S_{ij}$ is the mean strain-rate tensor. Note that the second term on the right-hand side of Equation (4.6) is needed to obtain the proper trace of $\tau_{ij}$. That is, since $S_{ii} = 0$ for incompressible flow, contracting Equation (4.6) yields $\tau_{ii} = -2\rho k$ in accord with Equation (4.3).

**Turbulent Transport and Pressure Diffusion:** The standard approximation made to represent turbulent transport of scalar quantities in a turbulent flow is that of gradient-diffusion. In analogy to molecular transport processes, we say that $-\overline{u_j'\phi'} \sim \mu_T \partial\Phi/\partial x_j$. Unfortunately, there is no corresponding straightforward analog for the pressure diffusion term. For want of definitive experimental data, the pressure diffusion term has generally been grouped with the turbulent transport, and the sum assumed to behave as a gradient-transport process. Fortunately, recent DNS results [e.g., Mansour, Kim and Moin (1988)] indicate that the term is quite small for simple flows. Thus, we assume that

$$\frac{1}{2}\rho\overline{u_i'u_i'u_j'} + \overline{p'u_j'} = -\frac{\mu_T}{\sigma_k}\frac{\partial k}{\partial x_j} \tag{4.7}$$

where $\sigma_k$ is a closure coefficient. Note that Equation (4.7) simply defines $\sigma_k$. As stressed by Bradshaw (1992), this statement applies to all turbulence closure coefficients. At this point, no approximation has entered although, of course, we hope the model is realistic enough that $\sigma_k$ can be chosen to be constant.

**Dissipation:** The manner in which we determine the dissipation is not unique amongst turbulence energy equation models. It suffices at this point to note that we still have two unknown parameters, which are the turbulence length scale, $\ell$, and the dissipation, $\epsilon$. If both properties are assumed to be strictly functions of the turbulence independent of natural fluid properties such as molecular viscosity, purely dimensional arguments [Taylor (1935)] show that

$$\epsilon \sim k^{3/2}/\ell \tag{4.8}$$

Hence, we still need a prescription for the length scale of the turbulence in order to close our system of equations. In the following sections, we will explore the various methods that have been devised to determine the length scale.

Combining Equations (4.4) and (4.7), we can write the modeled version of the turbulence kinetic energy equation that is used in virtually all turbulence energy equation models. The equation assumes the following form,

$$\rho\frac{\partial k}{\partial t} + \rho U_j\frac{\partial k}{\partial x_j} = \tau_{ij}\frac{\partial U_i}{\partial x_j} - \rho\epsilon + \frac{\partial}{\partial x_j}\left[(\mu + \mu_T/\sigma_k)\frac{\partial k}{\partial x_j}\right] \tag{4.9}$$

where $\tau_{ij}$ is given by Equation (4.6).

## 4.2 One-Equation Models

To complete closure of the turbulence kinetic energy equation, Prandtl postulated that the dissipation assumes the form quoted in Equation (4.8). Introducing a closure coefficient that we will call $C_D$, the dissipation is

$$\epsilon = C_D k^{3/2}/\ell \tag{4.10}$$

and the turbulence length scale remains the only unspecified part of the model. Given twenty years of experience with the mixing-length model, Prandtl had sufficient confidence that he could generalize established prescriptions for the turbulence length scale $\ell$. Of course, $\ell \propto \ell_{mix}$ only if the ratio of production to dissipation is constant. To see this, note that in a thin shear layer, production balancing dissipation means we have $\partial U/\partial y = (-\overline{u'v'})^{1/2}/\ell_{mix}$. Hence, we obtain $(-\overline{u'v'})^{3/2}/\ell_{mix} = C_D k^{3/2}/\ell$ so that $\ell \propto \ell_{mix}$ if $-\overline{u'v'}/k =$ constant. Thus, the first **One-Equation Model** appears as follows:

$$\rho\frac{\partial k}{\partial t} + \rho U_j \frac{\partial k}{\partial x_j} = \tau_{ij}\frac{\partial U_i}{\partial x_j} - C_D\rho\frac{k^{3/2}}{\ell} + \frac{\partial}{\partial x_j}\left[(\mu + \mu_T/\sigma_k)\frac{\partial k}{\partial x_j}\right] \tag{4.11}$$

where $\tau_{ij}$ is given by Equation (4.6) and the eddy viscosity is

$$\mu_T = \rho k^{1/2}\ell \tag{4.12}$$

Note that at this point we make an implicit assumption regarding the "constant" in Equation (4.2), which has been set equal to one. That is, there is no a priori reason why $\mu_T$ should depend only upon $k$ and $\ell$, i.e., no reason why "constant" should really be constant. In reality, $\mu_T$ is the ratio of a turbulence quantity (e.g., $-\rho\overline{u'v'}$) to a mean flow quantity (e.g., $\partial U/\partial y + \partial V/\partial x$). Consequently, $\mu_T$ will not, in general, precisely follow mean-flow scales such as $U_e$ and $\delta^*$ or turbulence scales such as $k$ and $\ell$. Only in **equilibrium flows** for which production and dissipation balance are mean-flow and turbulence scales proportional — and then either can be used for $\mu_T$. Otherwise, an unknown mix of scales is needed.

Emmons (1954) proposed essentially the same model in an independent research effort. Before the model can be used in applications, the length scale, $\ell$, and the closure coefficients $\sigma_k$ and $C_D$ must be specified. Emmons (1954) and Glushko (1965) applied this model to several flows with some degree of success using $\sigma_k = 1$ and $C_D$ ranging between 0.07 and 0.09. Their length scale distributions were similar to those used for the mixing-length model. Wolfshtein (1967) found that by introducing damping factors in the dissipation and eddy viscosity similar to the Van Driest

factor [Equation (3.105)], more satisfactory results can be obtained with this model for low-Reynolds-number flows. More recently, Goldberg (1991) has refined the model even further.

Although more complex than an algebraic model, the Prandtl-Emmons-Glushko one-equation model is certainly straightforward and elegant. As originally postulated it involves two closure coefficients and one closure function (the length scale). Even with Wolfshtein's low-Reynolds-number corrections, the number of closure coefficients increases by only two so that the model actually has fewer closure coefficients than the Baldwin-Lomax and Johnson-King models. For attached flows, the Goldberg model has five closure coefficients, two damping functions, and a closure function for the length scale. Goldberg's number of closure coefficients and empirical functions more than doubles for separated flows.

Bradshaw, Ferriss and Atwell (1967) formulated a one-equation model that avoids introducing a gradient-diffusion approximation. Rather than introduce the Boussinesq approximation, they argue that for a wide range of flows, the ratio of the Reynolds shear stress, $\tau_{xy}$, to the turbulence kinetic energy, $k$, is constant. Measurements [Townsend (1976)] indicate that for boundary layers, wakes and mixing layers the ratio is very nearly the same and given by

$$\tau_{xy} \approx 0.3\rho k \tag{4.13}$$

Building upon this presumably universal result, Bradshaw, Ferriss and Atwell formulated a one-equation model based on the turbulence kinetic energy. A novel feature of their formulation is that the equations are hyperbolic for boundary layers rather than parabolic. This is a direct consequence of introducing Equation (4.13) in modeling the $k$ equation's turbulent transport term rather than a gradient-diffusion approximation. The resulting equations are thus solved using the method of characteristics. Figure 4.1 compares computed and measured skin friction for Flow 3300 of the 1968 AFOSR-IFP-Stanford Conference on the Computation of Turbulent Boundary Layers. As shown, the differences between theory and experiment are much less than those obtained using the Cebeci-Smith and Baldwin-Lomax models [see Figure 3.16]. Overall, the Bradshaw-Ferriss-Atwell model's skin friction for boundary layers in adverse pressure gradient was closest of the various models tested in the 1968 Conference to measured values.

One-equation models have been formulated that are based on something other than the turbulence energy equation. Nee and Kovasznay (1968), for example, postulated a phenomenological transport equation for the kinematic eddy viscosity, $\nu_T = \mu_T/\rho$. The equation involves terms similar to those appearing in Equation (4.11). The model has four closure coefficients

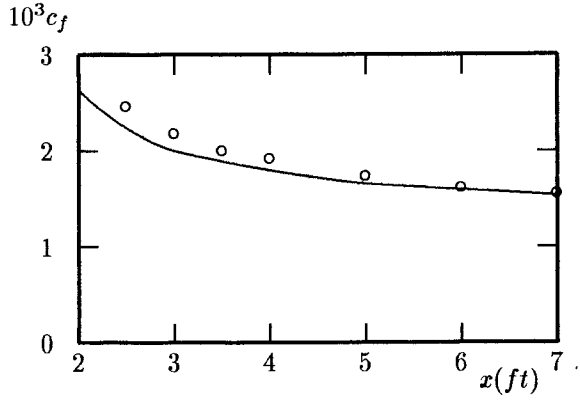


Figure 4.1: Comparison of computed and measured skin friction for Bradshaw Flow C; —— Bradshaw-Ferriss-Atwell; o Bradshaw.

and requires prescription of the turbulence length scale.

More recently, Baldwin and Barth (1990) and Spalart and Allmaras (1992) have devised even more elaborate model equations for the eddy viscosity. The Baldwin-Barth model, for example, includes seven closure coefficients, two empirical damping functions and a function describing the turbulence length scale. The Baldwin-Barth model is as follows.

**Kinematic Eddy Viscosity**

$$\nu_T = C_\mu \nu \tilde{R}_T D_1 D_2 \tag{4.14}$$

**Turbulence Reynolds Number**

$$\frac{\partial}{\partial t}\left(\nu\tilde{R}_T\right) + U_j \frac{\partial}{\partial x_j}\left(\nu\tilde{R}_T\right) = (C_{\epsilon 2} f_2 - C_{\epsilon 1})\sqrt{\nu \tilde{R}_T P} + (\nu + \nu_T/\sigma_\epsilon)\frac{\partial^2(\nu\tilde{R}_T)}{\partial x_k \partial x_k} - \frac{1}{\sigma_\epsilon}\frac{\partial \nu_T}{\partial x_k}\frac{\partial(\nu\tilde{R}_T)}{\partial x_k} \tag{4.15}$$

**Closure Coefficients**

$$C_{\epsilon 1} = 1.2, \quad C_{\epsilon 2} = 2.0, \quad C_\mu = 0.09, \quad A_o^+ = 26, \quad A_2^+ = 10 \tag{4.16}$$

$$\frac{1}{\sigma_\epsilon} = (C_{\epsilon 2} - C_{\epsilon 1})\sqrt{C_\mu}/\kappa^2, \qquad \kappa = 0.41 \tag{4.17}$$

**Auxiliary Relations**

$$P = \nu_T \left[\left(\frac{\partial U_i}{\partial x_j} + \frac{\partial U_j}{\partial x_i}\right)\frac{\partial U_i}{\partial x_j} - \frac{2}{3}\frac{\partial U_k}{\partial x_k}\frac{\partial U_k}{\partial x_k}\right] \tag{4.18}$$

$$D_1 = 1 - e^{-y^+/A_o^+} \quad \text{and} \quad D_2 = 1 - e^{-y^+/A_2^+} \tag{4.19}$$

$$f_2 = \frac{C_{\epsilon 1}}{C_{\epsilon 2}} + \left(1 - \frac{C_{\epsilon 1}}{C_{\epsilon 2}}\right)\left(\frac{1}{\kappa y^+} + D_1 D_2\right) \cdot \left[\sqrt{D_1 D_2} + \frac{y^+}{\sqrt{D_1 D_2}}\left(\frac{D_2}{A_o^+} e^{-y^+/A_o^+} + \frac{D_1}{A_2^+} e^{-y^+/A_2^+}\right)\right] \tag{4.20}$$

The Spalart-Allmaras model is also written in terms of the eddy viscosity. The model includes eight closure coefficients and three damping functions. Its defining equations are as follows.

**Kinematic Eddy Viscosity**

$$\nu_T = \tilde{\nu} f_{v1} \tag{4.21}$$

**Eddy Viscosity Equation**

$$\frac{\partial \tilde{\nu}}{\partial t} + U_j \frac{\partial \tilde{\nu}}{\partial x_j} = c_{b1} \tilde{S} \tilde{\nu} - c_{w1} f_w \left(\frac{\tilde{\nu}}{d}\right)^2 + \frac{1}{\sigma} \frac{\partial}{\partial x_k}\left[(\nu + \tilde{\nu}) \frac{\partial \tilde{\nu}}{\partial x_k}\right] + \frac{c_{b2}}{\sigma} \frac{\partial \tilde{\nu}}{\partial x_k} \frac{\partial \tilde{\nu}}{\partial x_k} \tag{4.22}$$

**Closure Coefficients**

$$c_{b1} = 0.1355, \quad c_{b2} = 0.622, \quad c_{v1} = 7.1, \quad \sigma = 2/3 \tag{4.23}$$

$$c_{w1} = \frac{c_{b1}}{\kappa^2} + \frac{(1 + c_{b2})}{\sigma}, \quad c_{w2} = 0.3, \quad c_{w3} = 2, \quad \kappa = 0.41 \tag{4.24}$$

**Auxiliary Relations**

$$f_{v1} = \frac{\chi^3}{\chi^3 + c_{v1}^3}, \qquad f_{v2} = 1 - \frac{\chi}{1 + \chi f_{v1}}, \qquad f_w = g\left[\frac{1 + c_{w3}^6}{g^6 + c_{w3}^6}\right]^{1/6} \tag{4.25}$$

$$\chi = \frac{\tilde{\nu}}{\nu}, \qquad g = r + c_{w2}(r^6 - r), \qquad r = \frac{\tilde{\nu}}{\tilde{S} \kappa^2 d^2} \tag{4.26}$$

$$\tilde{S} = S + \frac{\tilde{\nu}}{\kappa^2 d^2} f_{v2}, \qquad S = \sqrt{2 \Omega_{ij} \Omega_{ij}} \tag{4.27}$$

The tensor $\Omega_{ij} = \frac{1}{2}(\partial U_i/\partial x_j - \partial U_j/\partial x_i)$ is the rotation tensor and $d$ is distance from the closest surface. Although not listed here, the model even includes a transition correction that introduces four additional closure coefficients and two more empirical functions.

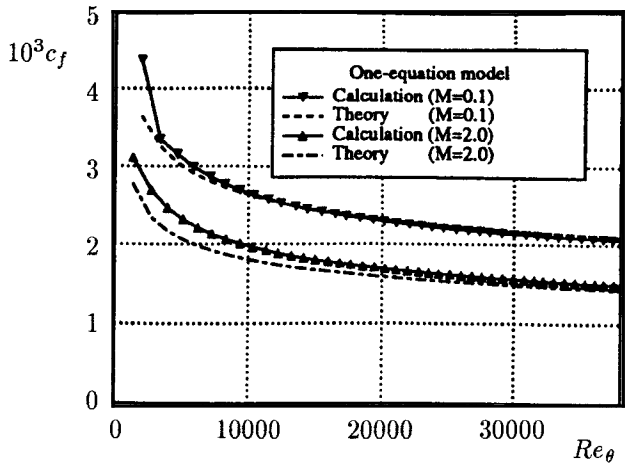


Figure 4.2: Comparison of computed and measured flat-plate boundary layer skin friction at Mach 0.1 and Mach 2.0; Baldwin-Barth model. [From Baldwin and Barth (1990).]

Figure 4.2 illustrates how well the Baldwin-Barth model reproduces correlations of measured skin friction [see Hopkins and Inouye (1971)] for constant-pressure boundary layers.

Figures 4.3 and 4.4 show how the Baldwin-Barth model fares for the two key flows considered by Menter (1992b). For both flows, the Baldwin-Barth model skin friction deviates from measured values even more than the Baldwin-Lomax model (see Figures 3.15 and 3.17). Although not shown, the Spalart-Allmaras model yields $c_f$ for the Samuel-Joubert case that lies about as far above the measurements as the Baldwin-Barth $c_f$ lies below [see Spalart and Allmaras (1992)].

In summary, only a modest advantage is gained in using a one-equation model rather than a mixing-length model. While the recent developments by Goldberg, Baldwin and Barth and Spalart and Allmaras show improved predictive capability (relative to early one-equation models) for some flows, their track record remains spotty. On the one hand, the Goldberg, Baldwin-Barth and Spalart-Allmaras models have achieved closer agreement with measurements for a limited number of separated flows than is possible with algebraic models. On the other hand, the Baldwin-Lomax model appears to be superior to the Baldwin-Barth model for the relatively simple Samuel-Joubert flow and for Driver's separated flow. While these newer models appear promising for separated flows, more research and testing is needed.

Given all of these facts, we clearly have not yet arrived at anything

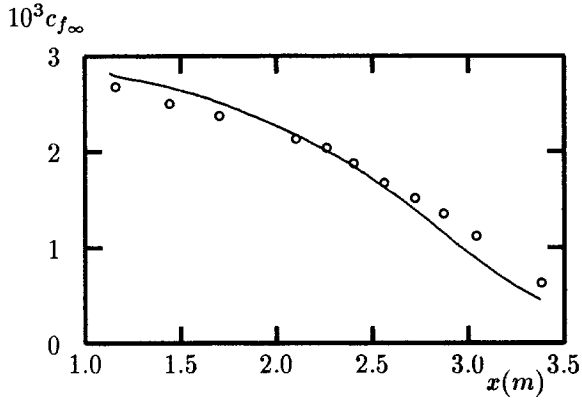


Figure 4.3: Computed and measured skin friction for Samuel-Joubert's adverse pressure gradient flow; —— Baldwin-Barth; o Samuel-Joubert.

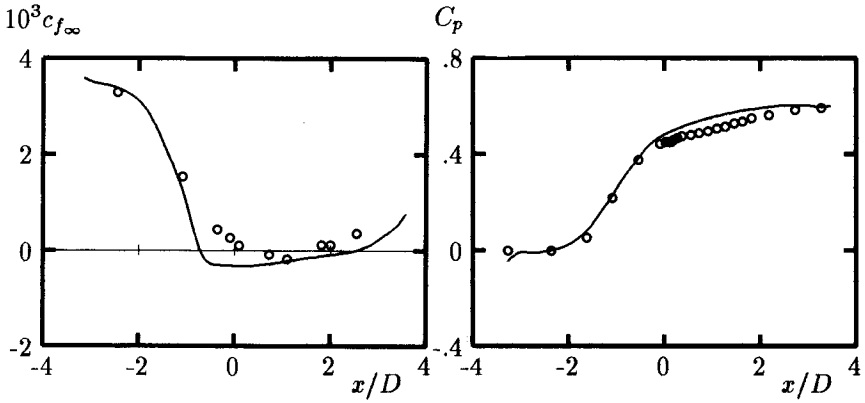


Figure 4.4: Computed and measured flow properties for Driver's separated flow; —— Baldwin-Barth; o Driver.

resembling a universal turbulence model. While there is a smaller need for adjustment from flow to flow than with the mixing-length model, abrupt changes from wall-bounded to free shear flows (e.g., flow at a trailing edge of an airfoil) cannot be easily accommodated. In general, one-equation models share a few of the failures as well as most of the successes of the mixing-length model. To reach a more-nearly universal model, especially for separated flows, we must seek a model in which transport effects on the turbulence length scale are also accounted for. The rest of this chapter is devoted to investigating models that indeed include transport effects on the turbulence length scale.

## 4.3 Two-Equation Models

**Two-Equation Models** of turbulence have served as the foundation for much of the turbulence model research during the past two decades. For example, almost all of the computations done for the 1980-81 AFOSR-HTTM-Stanford Conference on Complex Turbulent Flows used two-equation turbulence models. These models provide not only for computation of $k$, but also for the turbulence length scale or equivalent. Consequently, two-equation models are **complete**, i.e., can be used to predict properties of a given turbulent flow with no prior knowledge of the turbulence structure. They are, in fact, the simplest complete model of turbulence.

The starting point for virtually all two-equation models is the Boussinesq approximation, Equation (4.6), and the turbulence kinetic energy equation in the form of Equation (4.9). As pointed out at the end of Section 4.1, there is a non-uniqueness in the way we determine the dissipation, $\epsilon$, or equivalently, the turbulence length scale, $\ell$.

Kolmogorov (1942), for example, pointed out that a second transport equation is needed to compute the so-called **specific dissipation rate**, $\omega$. This quantity has dimensions of $(\text{time})^{-1}$. On dimensional grounds, the eddy viscosity, turbulence length scale and dissipation can be determined from

$$\mu_T \sim \rho k/\omega, \quad \ell \sim k^{1/2}/\omega, \quad \epsilon \sim \omega k \tag{4.28}$$

Chou (1945) proposed modeling the exact equation for $\epsilon$. In terms of this formulation, the eddy viscosity and turbulence length scale are

$$\mu_T \sim \rho k^2/\epsilon, \quad \ell \sim k^{3/2}/\epsilon \tag{4.29}$$

Rotta (1951) first suggested a transport equation for the turbulence length scale and later (1968) proposed an equation for the product of $k$ and $\ell$. In either case,

$$\mu_T \sim \rho k^{1/2}\ell, \quad \epsilon \sim k^{3/2}/\ell \tag{4.30}$$

More recently, Zeierman and Wolfshtein (1986) introduced a transport equation for the product of $k$ and a **turbulence dissipation time**, $\tau$, which is essentially the reciprocal of Kolmogorov's $\omega$. Also, Speziale, Abid and Anderson (1990) have postulated an equation for $\tau$. For these models,

$$\mu_T \sim \rho k \tau, \quad \ell \sim k^{1/2}\tau, \quad \epsilon \sim k/\tau \tag{4.31}$$

Regardless of the choice of the second variable in our two-equation model, we see a recurring theme. Specifically, the dissipation, eddy viscosity and length scale are all related on the basis of dimensional arguments. Historically, dimensional analysis has been one of the most powerful tools available for deducing and correlating properties of turbulent flows. However, we should always be aware that while dimensional analysis is extremely useful, it unveils nothing about the physics underlying its implied scaling relationships. The physics is in the choice of variables.

One of the key conclusions of the 1980-81 AFOSR-HTTM-Stanford Conference on Complex Turbulent Flows was that the greatest amount of uncertainty about two-equation models lies in the transport equation complementing the equation for $k$. Further, it was even unclear about what the most appropriate choice of the second dependent variable is. In the decade following the Conference, interesting developments have occurred, most notably with the $k$-$\omega$ model that help clear up some, but not all, of the uncertainty.

Before proceeding to details of two-equation models, it is worthwhile to pause and note the following. As with one-equation models, there is no fundamental reason that $\mu_T$ should depend only upon turbulence parameters such as $k$, $\ell$, $\epsilon$ or $\omega$. In general, the ratio of individual Reynolds stresses to mean strain rate components depends upon both mean-flow and turbulence scales. Thus, two-equation turbulence models are no more likely than one-equation models to apply universally to turbulent flows, and can be expected to be inaccurate for many non-equilibrium turbulent flows.

### 4.3.1 The $k$-$\omega$ Model

As noted above, Kolmogorov (1942) proposed the first two-equation model of turbulence. Kolmogorov chose the kinetic energy of the turbulence as one of his turbulence parameters and, like Prandtl (1945), modeled the differential equation governing its behavior. His second parameter was the dissipation per unit turbulence kinetic energy, $\omega$. In his $k$-$\omega$ model, $\omega$ satisfies a differential equation similar to the equation for $k$. With no prior knowledge of Kolmogorov's work, Saffman (1970) formulated a $k$-$\omega$ model that would prove superior to the Kolmogorov model. As part of the Imperial

College efforts on two-equation models, Spalding [see Launder and Spalding (1972)] offered an improved version of the Kolmogorov model that removed some of its flaws. Shortly after formulation of Saffman's model and continuing to the present time, Wilcox et al. [Wilcox and Alber (1972), Saffman and Wilcox (1974), Wilcox and Traci (1976), Wilcox and Rubesin (1980), and Wilcox (1988a)] have pursued further development and application of $k$-$\omega$ turbulence models in earnest. Coakley (1983) has developed a $k^{1/2}$-$\omega$ model. In their critical review of two-equation turbulence models, Speziale, Abid and Anderson (1990) also propose a $k$-$\omega$ model.

In formulating his model, Kolmogorov referred to $\omega$ as "the rate of dissipation of energy in unit volume and time." To underscore its physical relation to the "'external scale' of turbulence, $\ell$," he also called it "some mean 'frequency' determined by $\omega = ck^{1/2}/\ell$, where $c$ is a constant." On the one hand, the reciprocal of $\omega$ is the time scale on which dissipation of turbulence energy occurs. While the actual process of dissipation takes place in the smallest eddies, the rate of dissipation is the rate of transfer of turbulence kinetic energy to the smallest eddies. Hence, this rate is set by the properties of the large eddies, and thus scales with $k$ and $\ell$, wherefore $\omega$ is indirectly associated with dissipative processes. On the other hand, in analogy to molecular viscosity, we expect the eddy viscosity to be proportional to the product of length and velocity scales characteristic of turbulent fluctuations, which is consistent with Kolmogorov's argument that $\omega \sim k^{1/2}/\ell$. Of course, we should keep in mind that analogies between molecular and turbulent processes are not trustworthy, and Kolmogorov's argument is essentially an exercise in dimensional analysis, not fundamental physics.

The development of the Kolmogorov model (1942) is quite brief and doesn't even establish values for all of the closure coefficients. Since little formal development of the equations is given, we can only speculate about how this great turbulence researcher may have arrived at his model equations. Since he makes no specific reference to any exact equations, it seems unlikely that he attempted to close the $k$ equation or other moments of the Navier Stokes equation term by term. Rather, as the great believer in the power of dimensional analysis that he was, it is easy to imagine that Kolmogorov's original reasoning may have gone something like this (note that for the sake of clarity the arguments below are in terms of kinematic eddy viscosity, $\nu_T = \mu_T/\rho$).

- Since $k$ already appears in the postulated constitutive relation [Equation (4.6)], it is plausible that $\nu_T \propto k$.
- The dimensions of $\nu_T$ are (length)$^2$/(time) while the dimensions of $k$ are (length)$^2$/(time)$^2$.

- Consequently $\nu_T/k$ has dimensions (time).
- Turbulence dissipation $\epsilon$ has dimensions (length)$^2$/(time)$^3$.
- Consequently $\epsilon/k$ has dimensions 1/(time).
- We can close Equations (4.6) and (4.9) by introducing a variable with dimensions (time) or 1/(time).

The next step is to postulate an equation for $\omega$. In doing so, the avenue that Kolmogorov took was to recognize that there are a fairly small number of physical processes commonly observed in the motion of a fluid. The most common processes are unsteadiness, convection (often referred to as advection), diffusion, dissipation, dispersion and production. Combining physical reasoning with dimensional analysis, Kolmogorov postulated the following equation for $\omega$.

$$\rho\frac{\partial\omega}{\partial t} + \rho U_j\frac{\partial\omega}{\partial x_j} = -\beta\rho\omega^2 + \frac{\partial}{\partial x_j}\left[\sigma\mu_T\frac{\partial\omega}{\partial x_j}\right] \tag{4.32}$$

We have taken some notational liberties in writing Equation (4.32), and $\beta$ and $\sigma$ are two new closure coefficients. This equation has three particularly noteworthy features. **First**, there is no analog to the $k$-equation's turbulence production term. The absence of a production term is consistent with Kolmogorov's notion that $\omega$ is associated with the smallest scales of the turbulence, and thus has no direct interaction with the mean motion. Note that his logic is flawed on this issue as the large-scale, energy-bearing eddies are primarily responsible for determining the appropriate time scale of the turbulence, and the rate of dissipation itself. **Second**, the equation is written in terms of $\omega$ rather than $\omega^2$. As will be shown when we analyze the defect layer in Subsection 4.6.2, Kolmogorov's decision to write his equation in terms of $\omega$ was a somewhat prophetic choice. **Third**, there is no molecular diffusion term so that this equation applies strictly to high-Reynolds-number flows and cannot be integrated through the viscous sublayer as it stands.

In subsequent development efforts, the interpretation of $\omega$ has behaved a bit like the turbulent fluctuations it is intended to describe. Saffman (1970) described $\omega$ as "a frequency characteristic of the turbulence decay process under its self-interaction." He stated further, "The rough idea is that $\omega^2$ is the mean square vorticity of the 'energy containing eddies' and [$k$] is the kinetic energy of the motion induced by this vorticity." Spalding [Launder and Spalding (1972)] and Wilcox and Alber (1972) identify $\omega$ as the RMS fluctuating vorticity, which is also known as **enstrophy**. Wilcox and Rubesin (1980), Wilcox (1988a) and Speziale et al. (1990) regard $\omega$ as

the ratio of $\epsilon$ to $k$, i.e., the rate of dissipation per unit turbulence kinetic energy.

The form of the equation for $\omega$ has changed as the $k$-$\omega$ model has evolved over the past five decades. A production term has been added by all model developers subsequent to Kolmogorov. Like Kolmogorov, Wilcox (1988a) and Speziale et al. (1990) write the equation for $\omega$ in terms of $\omega$. By contrast, most other $k$-$\omega$ models known to this author use an equation for $\omega^2$. Because it has been tested more extensively than any other $k$-$\omega$ model, we present the Wilcox (1988a) model as the state-of-the-art formulation.

**Eddy Viscosity**

$$\mu_T = \rho k/\omega \tag{4.33}$$

**Turbulence Kinetic Energy**

$$\rho\frac{\partial k}{\partial t} + \rho U_j\frac{\partial k}{\partial x_j} = \tau_{ij}\frac{\partial U_i}{\partial x_j} - \beta^*\rho k\omega + \frac{\partial}{\partial x_j}\left[(\mu + \sigma^*\mu_T)\frac{\partial k}{\partial x_j}\right] \tag{4.34}$$

**Specific Dissipation Rate**

$$\rho\frac{\partial \omega}{\partial t} + \rho U_j\frac{\partial \omega}{\partial x_j} = \alpha\frac{\omega}{k}\tau_{ij}\frac{\partial U_i}{\partial x_j} - \beta\rho\omega^2 + \frac{\partial}{\partial x_j}\left[(\mu + \sigma\mu_T)\frac{\partial \omega}{\partial x_j}\right] \tag{4.35}$$

**Closure Coefficients**

$$\alpha = 5/9, \quad \beta = 3/40, \quad \beta^* = 9/100, \quad \sigma = 1/2, \quad \sigma^* = 1/2 \tag{4.36}$$

**Auxiliary Relations**

$$\epsilon = \beta^*\omega k \quad \text{and} \quad \ell = k^{1/2}/\omega \tag{4.37}$$

### 4.3.2 The $k$-$\epsilon$ Model

By far, the most popular two-equation model is the $k$-$\epsilon$ model. The earliest development efforts based on this model were those of Chou (1945), Davidov (1961) and Harlow and Nakayama (1968). The central paper however, is that by Jones and Launder (1972) that, in the turbulence modeling community, has nearly reached the status of the Boussinesq and Reynolds papers. That is, the model is so well known that it is often referred to as the **Standard $k$-$\epsilon$ model** and reference to the Jones-Launder paper is often omitted. Actually, Launder and Sharma (1974) "retuned" the model's closure coefficients and most researchers use the form of the model presented in the 1974 paper.

Again, we begin with Equations (4.6) and (4.9). In formulating the $k$-$\epsilon$ model, the idea is to derive the exact equation for $\epsilon$ and to find suitable closure approximations for the exact equation governing its behavior. Recall that $\epsilon$ is defined by Equation (4.5). The exact equation for $\epsilon$ is derived by taking the following moment of the Navier-Stokes equation.

$$\overline{2\nu \frac{\partial u_i'}{\partial x_j} \frac{\partial}{\partial x_j} [\mathcal{N}(u_i)]} = 0 \tag{4.38}$$

where $\mathcal{N}(u_i)$ is the Navier-Stokes operator defined in Equation (2.26). After a considerable amount of algebra, the following equation for $\epsilon$ results.

$$\begin{aligned} \rho \frac{\partial \epsilon}{\partial t} + \rho U_j \frac{\partial \epsilon}{\partial x_j} = & -2\mu \left[ \overline{u_{i,k}' u_{j,k}'} + \overline{u_{k,i}' u_{k,j}'} \right] \frac{\partial U_i}{\partial x_j} - 2\mu \, \overline{u_k' u_{i,j}'} \frac{\partial^2 U_i}{\partial x_k \partial x_j} \\ & -2\mu \, \overline{u_{i,k}' u_{i,m}' u_{k,m}'} - 2\mu \, \nu \, \overline{u_{i,km}' u_{i,km}'} \\ & + \frac{\partial}{\partial x_j} \left[ \mu \frac{\partial \epsilon}{\partial x_j} - \mu \, \overline{u_j' u_{i,m}' u_{i,m}'} - 2\nu \, \overline{p_{,m}' u_{j,m}'} \right] \end{aligned} \tag{4.39}$$

This equation is far more complicated than the turbulence kinetic energy equation and involves several new unknown double and triple correlations of fluctuating velocity, pressure and velocity gradients. The terms on the three lines of the right-hand side of Equation (4.39) are generally regarded as **Production of Dissipation**, **Dissipation of Dissipation**, and the sum of **Molecular Diffusion of Dissipation** and **Turbulent Transport of Dissipation**, respectively. These correlations are essentially impossible to measure with any degree of accuracy so that there is presently little hope of finding reliable guidance from experimentalists regarding suitable closure approximations. Recent DNS studies such as the work of Mansour, Kim and Moin (1988) have helped gain some insight on the exact $\epsilon$ transport equation for low-Reynolds-number flows. However, the database for establishing closure approximations similar to those used for the $k$ equation remains very sparse.

Many researchers have proceeded undaunted by the lack of a rational basis for establishing closure approximations with a feeling of security that using Equation (4.39) as their foundation adds rigor to their approach. The strongest claim that can actually be made is that the conventional closure approximations used for Equation (4.39) are dimensionally correct. But this is not very different from the Kolmogorov (1942) and Saffman (1970) approaches that are guided almost exclusively by physical reasoning and dimensional analysis. An important point we should keep in mind is to **avoid modeling the differential equations rather than the physics of turbulence**. That is not to say we should avoid any reference to the

differential equations, for then we might formulate a model that violates a fundamental physical feature of the Navier-Stokes equation. Rather, we should avoid deluding ourselves into thinking that the **drastic surgery** approach to something as complex as Equation (4.39) is any more rigorous than dimensional-analysis arguments.

As a final comment, even if we had demonstrably accurate closure approximations for the exact $\epsilon$ transport equation, there is a serious question of their relevance to our basic closure problem. That is, the length or time scale required is that of the energy-containing, Reynolds-stress-bearing eddies rather than the dissipating eddies represented by the exact $\epsilon$ equation. So, we must ask whether the modeled $\epsilon$ equation represents the dissipation as such [as Equation (4.39) does], or whether it is actually an empirical equation for the rate of energy transfer from the large eddies (equal, of course, to the rate of dissipation in the small eddies). The answer seems clear since the closure approximations normally used parametrize the various terms in the modeled $\epsilon$ equation as functions of large-eddy scales (our use of dimensional analysis does this implicitly). As a consequence, the relation between the modeled equation for $\epsilon$ and the exact equation is so tenuous as to not need serious consideration.

The **Standard $k$-$\epsilon$ model** is as follows.

**Eddy Viscosity**

$$\mu_T = \rho C_\mu k^2/\epsilon \tag{4.40}$$

**Turbulence Kinetic Energy**

$$\rho\frac{\partial k}{\partial t} + \rho U_j\frac{\partial k}{\partial x_j} = \tau_{ij}\frac{\partial U_i}{\partial x_j} - \rho\epsilon + \frac{\partial}{\partial x_j}\left[(\mu + \mu_T/\sigma_k)\frac{\partial k}{\partial x_j}\right] \tag{4.41}$$

**Dissipation Rate**

$$\rho\frac{\partial \epsilon}{\partial t} + \rho U_j\frac{\partial \epsilon}{\partial x_j} = C_{\epsilon 1}\frac{\epsilon}{k}\tau_{ij}\frac{\partial U_i}{\partial x_j} - C_{\epsilon 2}\rho\frac{\epsilon^2}{k} + \frac{\partial}{\partial x_j}\left[(\mu + \mu_T/\sigma_\epsilon)\frac{\partial \epsilon}{\partial x_j}\right] \tag{4.42}$$

**Closure Coefficients**

$$C_{\epsilon 1} = 1.44, \quad C_{\epsilon 2} = 1.92, \quad C_\mu = 0.09, \quad \sigma_k = 1.0, \quad \sigma_\epsilon = 1.3 \tag{4.43}$$

**Auxiliary Relations**

$$\omega = \epsilon/(C_\mu k) \quad \text{and} \quad \ell = C_\mu k^{3/2}/\epsilon \tag{4.44}$$

### 4.3.3 Other Two-Equation Models

Two-equation models based on the turbulence length scale, $\ell$, and the turbulence time scale, $\tau$, have received less attention than the $k$-$\omega$ and $k$-$\epsilon$ models. Generally speaking, the level of agreement between measurements and predictions made with other models is comparable to $k$-$\omega$ and $k$-$\epsilon$ predictions for simple constant-pressure flows, but these models have not been pursued to any great extent. This subsection presents a brief overview of some of the length-scale and time-scale models. More details can be found in the various papers referenced in the discussion.

The proposed foundation for Rotta's (1968) $k$-$k\ell$ model is the **two-point velocity correlation tensor**. The correlation functions we have dealt with thus far are known as **single-point correlations** and involve products of fluctuating properties at a single point in the flow, $\mathbf{x}$. In a two-point correlation, we consider two points in the flow, say $\mathbf{x}$ and $\mathbf{x}+\mathbf{r}$, and do our time average. The two-point velocity correlation tensor is defined as

$$R_{ij}(\mathbf{x}, t; \mathbf{r}) = \overline{u_i'(\mathbf{x}, t)\, u_j'(\mathbf{x}+\mathbf{r}, t)} \tag{4.45}$$

The turbulence kinetic energy is simply one half the trace of $R_{ij}$ with a displacement $\mathbf{r} = \mathbf{0}$. Rotta's second variable is the product of $k$ and the **integral scale**, $\ell$, which is the integral of $R_{ii}$ over all displacements, $r = |\mathbf{r}|$. Thus Rotta's variables are given by

$$k = \frac{1}{2} R_{ii}(\mathbf{x}, t; \mathbf{0}) \tag{4.46}$$

$$k\ell = \frac{3}{16} \int_{-\infty}^{\infty} R_{ii}(\mathbf{x}, t; r)\, dr \tag{4.47}$$

As with attempts to model the exact dissipation equation, no particular advantage has been gained by introducing the double velocity correlation tensor. While an exact equation for $k\ell$ can indeed be derived, Rotta (1968) still must perform drastic surgery on the exact equation. For example, using standard closure approximations based largely on the strength of dimensional analysis, the following modeled version of the exact $k\ell$ equation results.

$$\begin{aligned} \rho \frac{\partial}{\partial t}(k\ell) + \rho U_j \frac{\partial}{\partial x_j}(k\ell) &= C_{L1} \rho \ell \tau_{ij} \frac{\partial U_i}{\partial x_j} - C_{L2} \rho k^{3/2} \\ &+ \frac{\partial}{\partial x_j} \left[ \mu \frac{\partial}{\partial x_j}(k\ell) + (\mu_T/\sigma_{L1}) \ell \frac{\partial k}{\partial x_j} + (\mu_T/\sigma_{L2}) k \frac{\partial \ell}{\partial x_j} \right] \end{aligned} \tag{4.48}$$

For this model, $k$ and $\mu_T$ are given by Equations (4.11) and (4.12). Rodi and Spalding (1970) and Ng and Spalding (1972) developed this model further. More recently, Smith (1990) has pursued development of the $k$-$k\ell$ model. Ng and Spalding found that for wall-bounded flows, the closure coefficient $C_{L2}$ must vary with distance from the surface. They propose the following set of closure coefficients.

$$C_{L1} = 0.98, \quad C_{L2} = 0.059 + 702(\ell/y)^6, \quad C_D = 0.09, \quad \sigma_k = \sigma_{L1} = \sigma_{L2} = 1 \tag{4.49}$$

On a similar tack, Zeierman and Wolfshtein (1986) base their model upon the **autocorrelation tensor** that involves the time average of fluctuating quantities at the same point in space but at different times. Thus, they work with the tensor

$$\mathcal{R}_{ij}(\mathbf{x}, t; t') = \overline{u_i'(\mathbf{x}, t) u_j'(\mathbf{x}, t + t')} \tag{4.50}$$

The turbulence kinetic energy is half the trace of $\mathcal{R}_{ij}$ with $t' = 0$, while the **integral time scale** is proportional to the integral of $\mathcal{R}_{ii}$ over all possible values of $t'$. Thus,

$$k = \frac{1}{2}\mathcal{R}_{ii}(\mathbf{x}, t; 0) \tag{4.51}$$

$$k\tau = \frac{1}{4}\int_{-\infty}^{\infty} \mathcal{R}_{ii}(\mathbf{x}, t; t')\, dt' \tag{4.52}$$

The Zeierman-Wolfshtein $k$-$k\tau$ model is as follows.

**Eddy Viscosity**

$$\mu_T = \rho C_\mu k\tau \tag{4.53}$$

**Turbulence Kinetic Energy**

$$\rho\frac{\partial k}{\partial t} + \rho U_j \frac{\partial k}{\partial x_j} = \tau_{ij}\frac{\partial U_i}{\partial x_j} - \rho\frac{k}{\tau} + \frac{\partial}{\partial x_j}\left[(\mu + \mu_T/\sigma_k)\frac{\partial k}{\partial x_j}\right] \tag{4.54}$$

**Integral Time Scale**

$$\rho\frac{\partial}{\partial t}(k\tau) + \rho U_j \frac{\partial}{\partial x_j}(k\tau) = C_{\tau 1}\,\tau\,\tau_{ij}\frac{\partial U_i}{\partial x_j} - C_{\tau 2}\rho k + \frac{\partial}{\partial x_j}\left[(\mu + \mu_T/\sigma_\tau)\frac{\partial}{\partial x_j}(k\tau)\right] \tag{4.55}$$

**Closure Coefficients**

$$C_{\tau 1} = 0.173, \quad C_{\tau 2} = 0.225, \quad C_\mu = 0.09, \quad \sigma_k = 1.46, \quad \sigma_\tau = 10.8 \tag{4.56}$$

**Auxiliary Relations**

$$\omega = 1/(C_\mu \tau), \quad \epsilon = k/\tau \quad \text{and} \quad \ell = C_\mu k^{1/2} \tau \tag{4.57}$$

Note that because the eddy viscosity is proportional to $k\tau$, Equation (4.55) can also be regarded as an equation for $\mu_T$.

Speziale, Abid and Anderson (1990) have taken a different approach in devising a $k$-$\tau$ model. Specifically, they introduce the formal change of dependent variables $\epsilon = k/\tau$ and transform the Standard $k$-$\epsilon$ model. The resulting equation for $\tau$ is as follows.

$$\begin{aligned} \rho \frac{\partial \tau}{\partial t} + \rho U_j \frac{\partial \tau}{\partial x_j} &= (1 - C_{\epsilon 1}) \frac{\tau}{k} \tau_{ij} \frac{\partial U_i}{\partial x_j} + (C_{\epsilon 2} - 1)\rho \\ &\quad + \frac{\partial}{\partial x_j} \left[ (\mu + \mu_T/\sigma_{\tau 2}) \frac{\partial \tau}{\partial x_j} \right] \\ + \frac{2}{k}(\mu + \mu_T/\sigma_{\tau 1}) \frac{\partial k}{\partial x_k} \frac{\partial \tau}{\partial x_k} &- \frac{2}{\tau}(\mu + \mu_T/\sigma_{\tau 2}) \frac{\partial \tau}{\partial x_k} \frac{\partial \tau}{\partial x_k} \end{aligned} \tag{4.58}$$

Speziale, Abid and Anderson use the following revised set of closure coefficient values for their $k$-$\tau$ model that make it a bit different from the Standard $k$-$\epsilon$ model.

$$C_{\epsilon 1} = 1.44, \quad C_{\epsilon 2} = 1.83, \quad C_\mu = 0.09, \quad \sigma_k = \sigma_{\tau 1} = \sigma_{\tau 2} = 1.36 \tag{4.59}$$

In summary, the models listed above are representative of the various two-equation models that have been devised since Kolmogorov's (1942) $k$-$\omega$ model. While other models have been created, the intent of this text is to study models in a generic sense, as opposed to creating an encyclopedia of turbulence models. In the following sections we investigate several aspects of two-equation models including: (a) details on how the closure-coefficient values are chosen; (b) surface boundary conditions for wall-bounded flows; and, (c) applications to a variety of flows.

## 4.4 Closure Coefficients

All of the two-equation models have closure coefficients that have been introduced in replacing unknown double and triple correlations with algebraic expressions involving known turbulence and mean-flow properties. The Wilcox $k$-$\omega$ model, for example, has five, viz., $\alpha$, $\beta$, $\beta^*$, $\sigma$ and $\sigma^*$. If our theory were exact, we could set the values of these coefficients from first principles much as we use the kinetic theory of gases to determine the viscosity coefficient in Stokes' approximation for laminar flows. Unfortunately, the theory is not exact, but rather a model developed mainly on the

strength of dimensional analysis. Consequently, the best we can do is to set the values of the closure coefficients to assure agreement with observed properties of turbulence.

This section describes the manner in which the closure coefficients have been determined for the Wilcox $k$-$\omega$ model. There is no loss of generality in doing this however, since **these same general arguments have been used in establishing the values of the closure coefficients in most two-equation models.** The Problems section at the end of the chapter examines some of the (relatively minor) differences among the various models.

We can establish the ratio of $\beta^*$ to $\beta$ by applying the model to decaying homogeneous, isotropic turbulence. In this kind of turbulence, there are no spatial gradients of any mean-flow properties wherefore Equations (4.34) and (4.35) simplify to

$$\frac{dk}{dt} = -\beta^* \omega k \quad \text{and} \quad \frac{d\omega}{dt} = -\beta \omega^2 \tag{4.60}$$

from which the asymptotic solution for $k$ is readily found to be

$$k \sim t^{-\beta^*/\beta} \tag{4.61}$$

Experimental observations [Townsend (1976)] indicate that $k \sim t^{-n}$ where $n = 1.25 \pm 0.06$ for decaying homogeneous, isotropic turbulence. Choosing $\beta^*/\beta = 6/5$ sets the ratio at the lower end of the range of accepted values.

Values for the coefficients $\alpha$ and $\beta^*$ can be established by examining the **log layer**. Recall from Section 3.4 that the log layer is defined as the portion of the boundary layer sufficiently distant from the surface that molecular viscosity is negligible relative to eddy viscosity, yet close enough for convective effects to be negligible. In the limiting case of an incompressible constant-pressure boundary layer, defining $\nu_T = \mu_T/\rho$, the mean-momentum equation and the equations for $k$ and $\omega$ simplify to

$$\left.\begin{aligned} 0 &= \frac{\partial}{\partial y}\left[\nu_T \frac{\partial U}{\partial y}\right] \\ 0 &= \nu_T \left(\frac{\partial U}{\partial y}\right)^2 - \beta^* \omega k + \sigma^* \frac{\partial}{\partial y}\left[\nu_T \frac{\partial k}{\partial y}\right] \\ 0 &= \alpha \left(\frac{\partial U}{\partial y}\right)^2 - \beta \omega^2 + \sigma \frac{\partial}{\partial y}\left[\nu_T \frac{\partial \omega}{\partial y}\right] \end{aligned}\right\} \tag{4.62}$$

We will justify the limiting form of these equations when we use perturbation methods to analyze the log layer in Subsection 4.6.1. We seek the

conditions under which these simplified equations yield a solution consistent with the law of the wall. As can be easily verified, Equations (4.62) possess such a solution, viz.,

$$U = \frac{u_\tau}{\kappa}\ell ny + \text{constant}, \qquad k = \frac{u_\tau^2}{\sqrt{\beta^*}}, \qquad \omega = \frac{u_\tau}{\sqrt{\beta^*}\kappa y} \tag{4.63}$$

where $u_\tau$ is the conventional friction velocity and $\kappa$ is Kármán's constant. There is one constraint imposed in the solution to Equations (4.62), namely, a unique relation exists between the implied value of Kármán's constant and the various closure coefficients. Specifically, the following equation must hold.

$$\alpha = \beta/\beta^* - \sigma\kappa^2/\sqrt{\beta^*} \tag{4.64}$$

Additionally, according to our solution the Reynolds shear stress, $\tau_{xy}$, is constant and equal to $\rho u_\tau^2$. Inspection of Equations (4.63) shows that this implies $\tau_{xy} = \sqrt{\beta^*}\rho k$ in the log layer. A variety of measurements [Townsend (1976)] indicate the ratio of $\tau_{xy}$ to $\rho k$ is about 3/10 in the log layer. This is the same ratio Bradshaw, Ferriss and Atwell (1967) used in formulating their one-equation model [c.f. Equation (4.13)]. Thus, the predicted log-layer solution is consistent with experimental observations provided we select $\beta^* = 9/100$.

We must work a bit harder to determine the values of $\sigma$ and $\sigma^*$. As we will see in Subsections 4.6.2 and 4.6.3, detailed analysis of the defect layer and the sublayer indicates that the optimum choice is $\sigma = \sigma^* = 1/2$. Finally, Equation (4.64) shows that selecting $\alpha = 5/9$ is consistent with Coles' value for the Kármán constant of 0.41.

Other arguments have been used to determine closure coefficients prior to any applications or computer optimization. Saffman (1970), for example, uses estimates based on vortex-stretching processes in simple shear and pure extension to effectively establish bounds on a coefficient similar to $\alpha$. He also requires that the length scale, $\ell$, be discontinuous at a turbulent-nonturbulent interface and finds that his model requires $\sigma = \sigma^* = 1/2$ to guarantee such behavior.

Zeierman and Wolfshtein (1986) use the fact that very close to separation, measurements [Townsend (1976)] indicate the law of the wall is replaced by

$$U \to \frac{1}{0.24}\sqrt{\frac{y}{\rho}\frac{dp}{dx}} \quad \text{as} \quad y \to 0 \tag{4.65}$$

They also observe from measurements of Laufer (1950) and Clark (1968) that, for flow near the center of a channel, the turbulence kinetic energy

and velocity are closely approximated by

$$\left.\begin{aligned} k/k_o &\approx 1 + 6.67(y/R)^2 \\ U/U_o &\approx 1 - 0.242(y/R)^2 \\ u_\tau^2 &\approx 0.048 U_o k_o^{1/2} \end{aligned}\right\} \quad \text{as} \quad y \to R \tag{4.66}$$

In conclusion, the specific arguments selected for determination of the closure coefficients are a free choice of the developer. For example, using arguments based on homogeneous turbulence **and** boundary layers assumes we have a degree of universality that may be grossly optimistic. That is, we are implicitly assuming our model is valid for grid turbulence, boundary layers, and many flows in between. Dropping this argument in favor of another boundary-layer argument may yield a model optimized for boundary layers but restricted to such flows. Ideally, we would find arguments that isolate each closure coefficient. Often, more than one is involved [e.g., Equation (4.64)]. In any event, for the sake of clarity, the arguments should be as simple as possible.

## 4.5 Application to Free Shear Flows

Our first applications will be for free shear flows. As with the mixing-length model, we seek similarity solutions to determine far-field behavior for the plane wake, mixing layer, plane jet and round jet. There are two noteworthy changes in our approach to obtaining a solution for free shear flows. **First**, for the mixing layer and the jets we can choose our similarity variable to be $\eta = y/x$. That is, with no loss of generality, we can set all scaling constants such as $A$ in Equations (3.70) and (3.71) equal to one. We had to carry such scaling coefficients for the mixing-length model because, by hypothesis, the mixing length is proportional to the width of the layer, which is proportional to the coefficient $A$. With two-equation models, the turbulence length scale is determined as part of the solution so that the way in which we scale the similarity variable $\eta$ is of no consequence. **Second**, while the rest of the methodology is the same, the addition of two extra differential equations complicates the problem somewhat. Because they are the most widely used two-equation models, we confine our attention to the $k$-$\omega$ and $k$-$\epsilon$ models. With the standard boundary-layer/shear-layer approximations, the equations of motion become:

$$\frac{\partial U}{\partial x} + \frac{1}{y^j}\frac{\partial}{\partial y}\left[y^j V\right] = 0 \tag{4.67}$$

$$\rho U \frac{\partial U}{\partial x} + \rho V \frac{\partial U}{\partial y} = \frac{1}{y^j}\frac{\partial}{\partial y}\left[y^j \tau_{xy}\right] \tag{4.68}$$

$$\tau_{xy} = \mu_T \frac{\partial U}{\partial y} \tag{4.69}$$

**$k$-$\omega$ Model:**

$$\left.\begin{aligned} &\rho U \frac{\partial k}{\partial x} + \rho V \frac{\partial k}{\partial y} = \tau_{xy} \frac{\partial U}{\partial y} - \beta^* \rho \omega k + \frac{1}{y^j} \frac{\partial}{\partial y} \left[ y^j \sigma^* \mu_T \frac{\partial k}{\partial y} \right] \\ &\rho U \frac{\partial \omega}{\partial x} + \rho V \frac{\partial \omega}{\partial y} = \alpha \frac{\omega}{k} \tau_{xy} \frac{\partial U}{\partial y} - \beta \rho \omega^2 + \frac{1}{y^j} \frac{\partial}{\partial y} \left[ y^j \sigma \mu_T \frac{\partial \omega}{\partial y} \right] \\ &\mu_T = \rho k / \omega \end{aligned}\right\} \tag{4.70}$$

**$k$-$\epsilon$ Model:**

$$\left.\begin{aligned} &\rho U \frac{\partial k}{\partial x} + \rho V \frac{\partial k}{\partial y} = \tau_{xy} \frac{\partial U}{\partial y} - \rho \epsilon + \frac{1}{y^j} \frac{\partial}{\partial y} \left[ y^j \frac{\mu_T}{\sigma_k} \frac{\partial k}{\partial y} \right] \\ &\rho U \frac{\partial \epsilon}{\partial x} + \rho V \frac{\partial \epsilon}{\partial y} = C_{\epsilon 1} \frac{\epsilon}{k} \tau_{xy} \frac{\partial U}{\partial y} - C_{\epsilon 2} \rho \frac{\epsilon^2}{k} + \frac{1}{y^j} \frac{\partial}{\partial y} \left[ y^j \frac{\mu_T}{\sigma_\epsilon} \frac{\partial \epsilon}{\partial y} \right] \\ &\mu_T = C_\mu \rho k^2 / \epsilon \end{aligned}\right\} \tag{4.71}$$

The similarity solution for the various free shear flows can be written in the following compact form.

**Far Wake:**

$$\left.\begin{aligned} &U(x,y) = U_\infty - \sqrt{\frac{D}{\rho x}}\, \mathcal{U}(\eta), \quad k(x,y) = \frac{D}{\rho x} K(\eta) \\ &\omega(x,y) = \frac{U_\infty}{x} W(\eta) \quad \epsilon(x,y) = \frac{D U_\infty}{\rho x^2} E(\eta) \\ &\eta = y \sqrt{\frac{\rho U_\infty^2}{D x}} \end{aligned}\right\} \tag{4.72}$$

**Mixing Layer:**

$$\left.\begin{aligned} &U(x,y) = U_1 \mathcal{U}(\eta), \quad k(x,y) = U_1^2 K(\eta) \\ &\omega(x,y) = \frac{U_1}{x} W(\eta), \quad \epsilon(x,y) = \frac{U_1^3}{x} E(\eta) \\ &\eta = \frac{y}{x} \end{aligned}\right\} \tag{4.73}$$

**Jet:**

$$\left.\begin{aligned} U(x,y) &= \frac{J^{1/2}}{x^{(j+1)/2}}\mathcal{U}(\eta), \quad k(x,y) = \frac{J}{x^{(j+1)}}K(\eta) \\ \omega(x,y) &= \frac{J^{1/2}}{x^{(j+3)/2}}W(\eta), \quad \epsilon(x,y) = \frac{J^{3/2}}{x^{(3j+5)/2}}E(\eta) \\ \eta &= \frac{y}{x} \end{aligned}\right\} \tag{4.74}$$

Substituting these self-similar representations into the mean momentum equation yields the following transformed equation.

$$\mathcal{V}\frac{d\mathcal{U}}{d\eta} - \frac{1}{\eta^j}\frac{d}{d\eta}\left[\eta^j N\frac{d\mathcal{U}}{d\eta}\right] = S_u\mathcal{U} \tag{4.75}$$

where the function $N(\eta)$ is the transformed eddy viscosity, $j = 1$ for the round jet, and $j = 0$ for the other three cases. The two terms on the left-hand side of Equation (4.75) are essentially vertical convection and diffusion. The term on the right-hand side is a source term that originates from the streamwise convection of momentum; Table 4.1 lists the coefficient $S_u$ and the normal velocity-like function, $\mathcal{V}(\eta)$, for each of the free shear flows considered. The transformed $k$, $\omega$ and $\epsilon$ equations are:

***k*-$\omega$ Model:**

$$\left.\begin{aligned} \mathcal{V}\frac{dK}{d\eta} - \frac{1}{\eta^j}\frac{d}{d\eta}\left[\eta^j\sigma^* N\frac{dK}{d\eta}\right] &= S_k K + N\left(\frac{d\mathcal{U}}{d\eta}\right)^2 - \beta^* WK \\ \mathcal{V}\frac{dW}{d\eta} - \frac{1}{\eta^j}\frac{d}{d\eta}\left[\eta^j\sigma N\frac{dW}{d\eta}\right] &= S_w W + \alpha\frac{W}{K}N\left(\frac{d\mathcal{U}}{d\eta}\right)^2 - \beta W^2 \\ N &= \frac{K}{W} \end{aligned}\right\} \tag{4.76}$$

***k*-$\epsilon$ Model:**

$$\left.\begin{aligned} \mathcal{V}\frac{dK}{d\eta} - \frac{1}{\eta^j}\frac{d}{d\eta}\left[\eta^j\frac{N}{\sigma_k}\frac{dK}{d\eta}\right] &= S_k K + N\left(\frac{d\mathcal{U}}{d\eta}\right)^2 - E \\ \mathcal{V}\frac{dE}{d\eta} - \frac{1}{\eta^j}\frac{d}{d\eta}\left[\eta^j\frac{N}{\sigma_\epsilon}\frac{dE}{d\eta}\right] &= S_e E + C_{\epsilon 1}\frac{E}{K}N\left(\frac{d\mathcal{U}}{d\eta}\right)^2 - C_{\epsilon 2}\frac{E^2}{K} \\ N &= C_\mu\frac{K^2}{E} \end{aligned}\right\} \tag{4.77}$$

Table 4.1: Free Shear Flow Parameters

| Flow | $S_u$ | $S_k$ | $S_w$ | $S_e$ | $j$ | $\mathcal{V}(\eta)$ |
|---|---|---|---|---|---|---|
| Far Wake | $\frac{1}{2}$ | 1 | 1 | 2 | 0 | $-\frac{1}{2}\eta$ |
| Mixing Layer | 0 | 0 | $\mathcal{U}$ | $\mathcal{U}$ | 0 | $-\int_0^\eta \mathcal{U}(\eta')\, d\eta'$ |
| Plane Jet | $\frac{1}{2}\mathcal{U}$ | $\mathcal{U}$ | $\frac{3}{2}\mathcal{U}$ | $\frac{5}{2}\mathcal{U}$ | 0 | $-\frac{1}{2}\int_0^\eta \mathcal{U}(\eta')\, d\eta'$ |
| Round Jet | $\mathcal{U}$ | $2\mathcal{U}$ | $2\mathcal{U}$ | $4\mathcal{U}$ | 1 | $-\frac{1}{\eta}\int_0^\eta \mathcal{U}(\eta')\eta'\, d\eta'$ |

The $k$, $\omega$ and $\epsilon$ equations contain convective terms, diffusion terms, and additional source terms corresponding to streamwise convection, production and dissipation. Table 4.1 lists the convective source term coefficients, $S_k$, $S_w$ and $S_e$.

Boundary conditions on the velocity are the same as in Chapter 3. We must also specify boundary conditions for $K$, $W$ and $E$. Solutions to all two-equation model equations feature sharp turbulent-nonturbulent interfaces for free shear flows, i.e., interfaces at which derivatives of flow properties are discontinuous. Consequently, the most sensible boundary conditions in the freestream are those corresponding to non-turbulent flow, i.e., $K(\eta)$, $W(\eta)$ and $E(\eta)$ all vanish approaching the edge of the shear layer. As it turns out, $k$-$\epsilon$ model solutions are unaffected by finite values of $K$ and $E$ in the freestream while $k$-$\omega$ model solutions are very sensitive to the freestream value of $W$. Subsection 7.2.2 gives complete details on the nature of two-equation model behavior near turbulent/nonturbulent interfaces. The boundary conditions that appear most appropriate for $K$, $W$ and $E$ are as follows.

**Wake and Jet:**

$$K'(0) = W'(0) = E'(0) = 0 \tag{4.78}$$

**Wake, Jet and Mixing Layer:**

$$K(\eta) \to 0, \quad W(\eta) \to W_\infty, \quad \text{and} \quad E(\eta) \to 0 \quad \text{as} \quad |\eta| \to \infty \tag{4.79}$$

Table 4.2: Free Shear Flow Spreading Rate

| Flow | $k$-$\omega$ Model | $k$-$\epsilon$ Model | Measured |
|---|---|---|---|
| Far Wake | .301-.500 | .256 | .365 |
| Mixing Layer | .103-.141 | .098 | .115 |
| Plane Jet | .090-.136 | .109 | .100-.110 |
| Round Jet | .073-.371 | .120 | .086-.095 |

The conventional definition of **spreading rate for the wake** is the value of $\eta$ given in Equation (4.72) where the velocity defect is half its maximum value. Similarly **for the plane and round jet, the spreading rate** is the value of $y/x$ where the velocity is half its centerline value. **For the mixing layer, the spreading rate** is usually defined as the difference between the values of $y/x$ where $(U - U_2)^2/(U_1 - U_2)^2$ is 9/10 and 1/10. Table 4.2 compares computed and measured spreading rates for the $k$-$\omega$ and $k$-$\epsilon$ models. A range of values is quoted for the $k$-$\omega$ model corresponding to values of $W_\infty$ ranging from 0 to 1 for the far wake and mixing layer, 0 to 10 for the plane jet, and 0 to 100 for the round jet. Using larger values of $W_\infty$ for these flows causes numerical difficulties, so these values appear to cover the permissible values for $W_\infty$. The largest spreading rate corresponds to $W_\infty = 0$.

These results show that having a **complete** model guarantees nothing regarding accuracy. Overall, the $k$-$\epsilon$ model behaves best from a computational point of view because of its insensitivity to freestream boundary conditions. However, its predicted spreading rate is 30% lower than measured for the far wake, 15% lower than measured for the mixing layer, and between 25% to 40% higher than measured for the round jet. Only for the plane jet does its predicted spreading rate fall within the range of measured values.

Using $W_\infty = 0$, the $k$-$\omega$ model consistently predicts spreading rates larger than measured. Specifically, computed spreading rates exceed corresponding measurements by 37%, 23%, 24% and 291% for the far wake, mixing layer, plane jet and round jet, respectively. There are values of $W_\infty$ that yield spreading rates much closer to the measured values. Specifically, using $W_\infty = 0.4$ for the far wake, $W_\infty = 0.5$ for the mixing layer, $W_\infty = 5$ for the plane jet, and $W_\infty = 50$ for the round jet yields spreading rates of .358, .115, .101 and .095, respectively. Figures 4.5 through 4.8 compare computed and measured velocity profiles obtained using these values for $W_\infty$. However, since there is no obvious reason for the choice of $W_\infty$, this

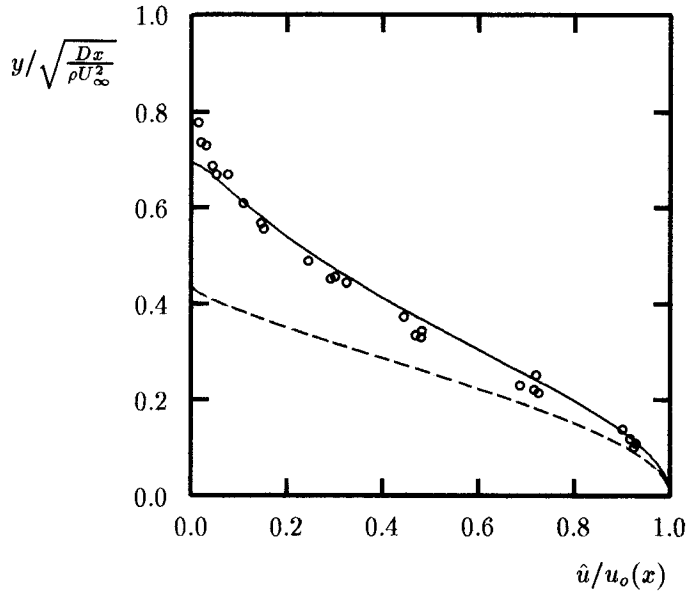


Figure 4.5: Comparison of computed and measured velocity profiles for the far wake; —— $k$-$\omega$ model; - - - $k$-$\epsilon$ model; o Fage and Falkner.

amounts to having an adjustable parameter in the model. Clearly, this is not much of an improvement over the mixing-length model predictions of Chapter 3. As a final comment, we can reasonably expect that the optimum values of $W_\infty$ used with the $k$-$\omega$ model for the self-preserving cases should give good results for non-self-preserving cases.

Menter (1992c) has developed a $k$-$\omega$ model that has no sensitivity to the freestream value of $\omega$. He accomplishes this by including a **cross-diffusion** term in the $\omega$ equation. That is, Menter writes the $\omega$ equation as follows.

$$\rho\frac{\partial\omega}{\partial t}+\rho U_j\frac{\partial\omega}{\partial x_j}=\alpha\frac{\omega}{k}\tau_{ij}\frac{\partial U_i}{\partial x_j}-\beta\rho\omega^2+\frac{\partial}{\partial x_j}\left[(\mu+\sigma\mu_T)\frac{\partial\omega}{\partial x_j}\right]$$
$$+\sigma_d\frac{\rho}{\omega}\frac{\partial k}{\partial x_j}\frac{\partial\omega}{\partial x_j} \qquad (4.80)$$

The term proportional to $\sigma_d$ in Equation (4.80) is Menter's cross-diffusion term. The effect of this term is to replace the entrainment velocity, $v$, in the $\omega$ equation by $(v-\sigma_d\omega^{-1}\partial k/\partial y)$. Since $k$ decreases approaching the shear layer edge (assuming $\sigma_d>0$), the net effect is to make the effective entrainment velocity positive (or at least less negative). As a result, $\omega$ diffuses from the turbulent region into the nonturbulent region, which is

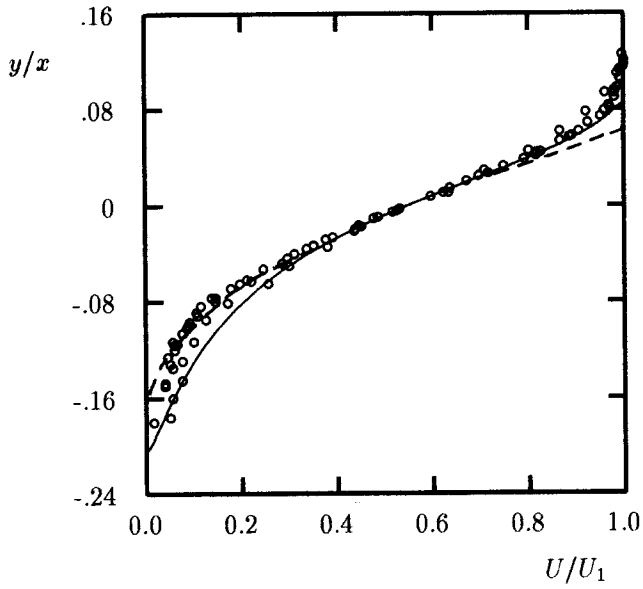


Figure 4.6: Comparison of computed and measured velocity profiles for the mixing layer; —— $k$-$\omega$ model; - - - $k$-$\epsilon$ model; o Liepmann and Laufer.

the opposite of what happens with the $k$-$\omega$ model. Thus, the freestream value of $\omega$ has no effect on the solution.

Menter also introduces a "blending function" that makes $\sigma_d = 0$ close to solid boundaries, while $\sigma_d \rightarrow 2\sigma$ away from such boundaries. Additionally, his blending function causes all of the model's closure coefficients to assume the values in Equation (4.36) near solid boundaries, and to asymptotically approach values similar to those used with the $k$-$\epsilon$ model otherwise. The net result is a model that behaves very much like the Wilcox (1988a) $k$-$\omega$ model for wall-bounded flows, and that is nearly identical to the $k$-$\epsilon$ model for free shear flows.

The author has research in progress at the time of this writing that indicates it may be sufficient to let:

$$\sigma_d = \begin{cases} 0, & \dfrac{\partial k}{\partial x_j}\dfrac{\partial \omega}{\partial x_j} \leq 0 \\ \sigma, & \dfrac{\partial k}{\partial x_j}\dfrac{\partial \omega}{\partial x_j} > 0 \end{cases} \tag{4.81}$$

Additionally, the value of $\sigma^*$ must assume a value larger than 0.5. As we will see in Subsection 4.6.2, it is important to suppress this cross-diffusion

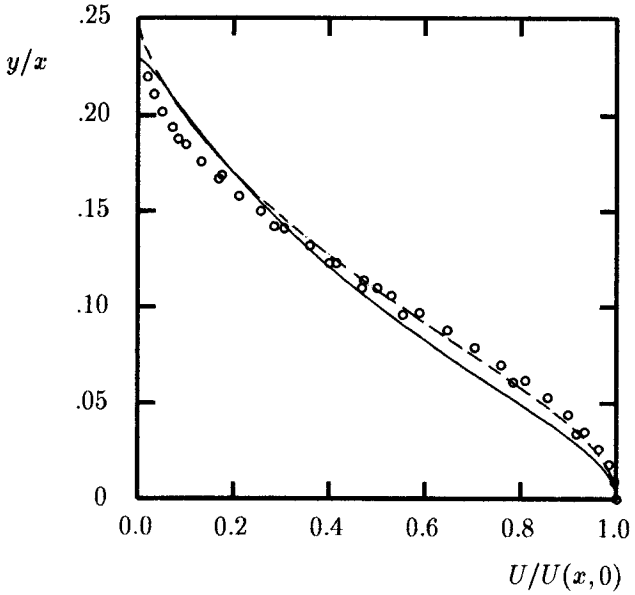


Figure 4.7: Comparison of computed and measured velocity profiles for the plane jet; —— $k$-$\omega$ model; - - - $k$-$\epsilon$ model; o Wygnanski and Fiedler.

term close to solid boundaries for wall-bounded flows. Just as Menter's blending function causes $\sigma_d$ to approach 0 near a solid boundary, so does Equation (4.81) since $k$ increases and $\omega$ decreases in the viscous sublayer. As with Menter's approach, this modification to the $\omega$ equation eliminates the model's sensitivity to the freestream value of $\omega$. However, while simpler than Menter's blending function approach, this straightforward modification yields shear layer spreading rates that are a bit farther from measurements than those predicted by the $k$-$\epsilon$ model. Other values of the $k$-$\omega$ model's closure coefficients exist that yield closer agreement with measured spreading rates, but that also compromise the model's accuracy for wall-bounded flows. Consequently, research continues in quest of an optimum formulation.

Pope (1978) has proposed a modification to the $\epsilon$ equation that resolves the so-called **round-jet/plane-jet anomaly**. That is, while experimental measurements indicate the spreading rate for the round jet is less than that of the plane jet, two-equation turbulence models predict the opposite. In Pope's modification, the **Dissipation of Dissipation** term in the $\epsilon$

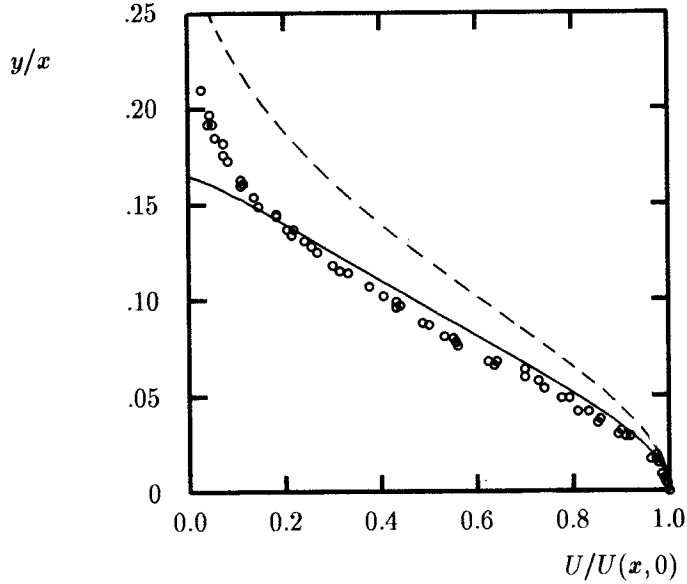


Figure 4.8: Comparison of computed and measured velocity profiles for the round jet; —— $k$-$\omega$ model; - - - $k$-$\epsilon$ model; o Bradbury.

equation is replaced by

$$C_{\epsilon 2}\frac{\epsilon^2}{k} \rightarrow [C_{\epsilon 2} - C_{\epsilon 3}\chi]\frac{\epsilon^2}{k} \tag{4.82}$$

where $\chi$ is a "nondimensional measure of vortex stretching" given by

$$\left.\begin{aligned} \chi &= \tilde{\omega}_{ij}\tilde{\omega}_{jk}\tilde{s}_{ki} \\ \tilde{s}_{ij} &= \frac{1}{2}\frac{k}{\epsilon}(U_{i,j} + U_{j,i}) \\ \tilde{\omega_{ij}} &= \frac{1}{2}\frac{k}{\epsilon}(U_{i,j} - U_{j,i}) \end{aligned}\right\} \tag{4.83}$$

Using $C_{\epsilon 3} = 0.79$ reduces the $k$-$\epsilon$ model's predicted spreading rate to 0.86, consistent with measurements. However, as pointed out by Rubel (1985), the Pope correction has an adverse effect on model predictions for the so-called **radial jet**, which we have not discussed here. This is the case of two jets of equal strength colliding and spreading radially. Without the Pope correction, the $k$-$\epsilon$ model predicts a radial-jet spreading rate of 0.095 which is close to the measured range of 0.096 to 0.110 [see Tanaka

and Tanaka (1976) and Witze and Dwyer (1976)]. Using the Pope correction for the radial jet reduces the $k$-$\epsilon$ model-predicted spreading rate to 0.040. Hence, as noted by Rubel, "the round jet/plane jet anomaly has been exchanged for a round jet/radial jet anomaly."

This concludes our analysis of free shear flows. In the following sections we turn our attention to wall-bounded flows. To demonstrate how two-equation models fare for such flows, we are going to use a powerful mathematical tool to analyze fine details of model-predicted structure of the turbulent boundary layer. In particular, we will use **perturbation methods** to analyze the various regions in the turbulent boundary layer.

## 4.6 Perturbation Analysis of the Boundary Layer

The differential equations for all but the simplest turbulence models are sufficiently complicated for most flows that closed-form solutions do not exist. This is especially true for boundary layers because of nonlinearity of the convection terms and the turbulent diffusion terms attending introduction of the eddy viscosity. Our inability to obtain closed-form solutions is unfortunate because such solutions are invaluable in design studies and for determining trends with a parameter such as Reynolds number, or more generally, for establishing laws of similitude. Furthermore, without analytical solutions, our ability to check the accuracy of numerical solutions is limited.

There is a powerful mathematical tool available to us to generate approximate solutions that are valid in special limiting cases, viz., **perturbation analysis**. The idea of perturbation analysis is to develop a solution in the form of an **asymptotic expansion** in terms of a parameter, the error being small for sufficiently small values of the parameter. Our desire in developing such an expansion is for the first few terms of the expansion to illustrate all the essential physics of the problem and to provide a close approximation to the exact solution. Fortunately, this is usually the case in fluid mechanics.

This section shows how perturbation analysis can be used to dissect model-predicted structure of the turbulent boundary layer. Appendix B introduces basic concepts of perturbation theory for the reader with no prior background in the field.

### 4.6.1 The Log Layer

We direct our focus to the turbulent boundary layer. Experimental observations provide a strong argument for using perturbation analysis. Specifically, Coles' description of the turbulent boundary layer as a "wake-like structure constrained by a wall" (see Figure 3.8) suggests that different scales and physical processes are dominant in the inner (near-wall) and outer (main body) of the layer. These are clearly concepts upon which perturbation analysis is based. Coles [see Coles and Hirst (1969)] makes an explicit connection with perturbation theory when he remarks:

> *"The idea that there are two distinct scales in a turbulent boundary layer is an old one, although quantitative expressions of this idea have evolved very slowly... To the extent that the outer velocity boundary condition for the inner (wall) profile is the same as the inner velocity boundary condition for the outer (wake) profile, the turbulent boundary layer is a singular perturbation problem of classical type. In fact, we can claim to have discovered the first two terms in a composite expansion, complete with logarithmic behavior."*

Often perturbation solutions are guided by dimensional considerations and a knowledge of physical aspects of the problem. For the turbulent boundary layer, we can draw from empirically established laws to aid us in developing our perturbation solution. We observe that close to a solid boundary, the **law of the wall** holds. We can write this symbolically as

$$U(x,y) = u_\tau(x) f(u_\tau y/\nu); \qquad u_\tau = \sqrt{\tau_w/\rho} \tag{4.84}$$

Similarly, the main body of the turbulent boundary layer behaves according to Clauser's (1956) well-known **defect law**, viz.,

$$U(x,y) = U_e(x) - u_\tau(x) F[y/\Delta(x)]; \qquad \Delta(x) = U_e \delta^*/u_\tau \tag{4.85}$$

The reader should keep in mind that Equation (4.85) only applies to a special class of boundary layers, i.e., boundary layers that are self preserving. Thus, we seek solutions where $F(y/\Delta)$ is independent of $x$. As we will see, the model equations predict existence of such solutions under precisely the same conditions Clauser discovered experimentally.

We develop the leading terms in a perturbation solution for the turbulent boundary layer in the following subsections. There are two small parameters in our problem, the first being the reciprocal of the Reynolds number. This is consistent with the standard boundary-layer approximations. The second small parameter is $u_\tau/U_e$. Clauser's defect law suggests

this parameter since the velocity is expressed as a (presumably) small deviation from the freestream velocity that is proportional to $u_\tau$. The analysis will lead to a relation between these two parameters.

The analysis in this section, which is patterned after the work of Bush and Fendell (1972) and Fendell (1972), shows in Subsection 4.6.3 that the inner expansion is of the form quoted in Equation (4.84) and is valid in the **viscous sublayer** (see Figure 3.7). We also show in Subsection 4.6.2 that the outer expansion is identical in form to Equation (4.85) and holds in the **defect layer**. Formal matching of the sublayer and defect-layer solutions occurs in an overlap region that is often described as the **log layer**. In fact, the common part of the inner and outer expansions is precisely the law of the wall. Thus, although it is not formally a separate layer, establishing flow properties in the log layer permits independent analysis of the sublayer and defect layer. It also forms the basis of surface boundary conditions for many two-equation turbulence models. We discuss the log layer in this subsection.

Before performing any analysis, we anticipate that we will be solving a **singular perturbation problem**. We expect this, but not because of a reduction in order of the differential equations. Rather, we have no hope of satisfying the no-slip condition with our outer solution because of the assumed form in the defect layer, i.e., velocity being a small perturbation from the freestream value. Likewise, the sublayer solution, if it is consistent with measurements, predicts velocity increasing logarithmically with distance from the surface as $y \to \infty$ so that we cannot satisfy the freestream boundary condition with our inner solution. This is the irregular behavior near boundaries alluded to in Appendix B where we define a singular perturbation problem.

We begin our analysis with the incompressible boundary layer equations. Conservation of mass and momentum are sufficient for establishing the form of the expansions, so that we have no need to introduce the model equations now. For two-dimensional flow, we have

$$\frac{\partial U}{\partial x} + \frac{\partial V}{\partial y} = 0 \tag{4.86}$$

$$U\frac{\partial U}{\partial x} + V\frac{\partial U}{\partial y} = -\frac{1}{\rho}\frac{dP}{dx} + \frac{\partial}{\partial y}\left[(\nu + \nu_T)\frac{\partial U}{\partial y}\right] \tag{4.87}$$

The easiest way to arrive at the **log-layer** equations is to derive the **sublayer** equations and then to determine the limiting form of the sublayer equations for $y^+ \to \infty$. Consistent with the normal boundary-layer concept that variations in the streamwise ($x$) direction are much less rapid than those in the normal ($y$) direction, we scale $x$ and $y$ differently. Letting $L$

denote a dimension characteristic of distances over which flow properties change in the $x$ direction, we scale $x$ and $y$ according to

$$\xi = x/L \qquad and \qquad y^+ = u_\tau y/\nu \tag{4.88}$$

The appropriate expansion for the streamfunction and kinematic eddy viscosity are

$$\psi_{inner}(x,y) \sim \nu[f_0(\xi,y^+) + \phi_1 f_1(\xi,y^+) + o(\phi_1)] \tag{4.89}$$

$$\nu_{T_{inner}}(x,y) \sim \nu[N_0(\xi,y^+) + \phi_1 N_1(\xi,y^+) + o(\phi_1)] \tag{4.90}$$

where the asymptotic sequence $\{1,\phi_1,\phi_2,\ldots\}$ is to be determined. Consequently, the streamwise velocity becomes

$$U(x,y) \sim u_\tau[\hat{u}_0(\xi,y^+) + \phi_1\hat{u}_1(\xi,y^+) + o(\phi_1)]; \qquad \hat{u}_n \equiv \frac{\partial f_n}{\partial y^+} \tag{4.91}$$

Substituting into the momentum equation, we obtain

$$\frac{\partial}{\partial y^+}\left[(1+N_0)\frac{\partial \hat{u}_0}{\partial y^+}\right] + O(\phi_1) = \frac{1}{Re_{\delta^*}}\left[\beta_T + O\left(\frac{\delta^*}{L}\right)\right] \tag{4.92}$$

where $Re_{\delta^*}$ is Reynolds number based on displacement thickness, and the quantity $\beta_T$ is the so-called **equilibrium parameter** [see Coles and Hirst (1969)] defined by

$$\beta_T \equiv \frac{\delta^*}{\tau_w}\frac{dP}{dx} \tag{4.93}$$

In general, we regard $\beta_T$ as being of order one. In fact, when we analyze the defect layer this will be the key parameter quantifying the effect of pressure gradient on our solution. Additionally, $Re_{\delta^*} \gg 1$ and $\delta^* \ll L$. Hence, we conclude that

$$\phi_1 = 1/Re_{\delta^*} \tag{4.94}$$

and

$$\frac{\partial}{\partial y^+}\left[(1+N_0)\frac{\partial \hat{u}_0}{\partial y^+}\right] = 0 \tag{4.95}$$

To enhance physical understanding of what we have just proven, it is worthwhile to return to dimensional variables. We have shown that, to leading order, the convective terms and the pressure gradient are small compared to the other terms in the sublayer so that the momentum equation simplifies to

$$\frac{\partial}{\partial y}\left[(\nu+\nu_T)\frac{\partial U}{\partial y}\right] = 0 \tag{4.96}$$

Integrating once tells us that the sum of the molecular and Reynolds shear stress is constant in the sublayer, i.e.,

$$(\mu + \mu_T)\frac{\partial U}{\partial y} = \tau_w \tag{4.97}$$

Equation (4.96) or (4.97) is the equation for the leading order term in the inner expansion for a turbulent boundary layer. As we will demonstrate in greater detail in Subsection 4.6.3, we can satisfy the no-slip condition ($U = 0$) at $y = 0$ while the solution as $y^+ \to \infty$ asymptotes to the law of the wall, i.e., velocity increasing logarithmically with distance from the surface. Another feature of the solution is that the eddy viscosity increases linearly with $y^+$ as $y^+ \to \infty$ so that the eddy viscosity becomes very large compared to the molecular viscosity. Consistent with this behavior, the molecular viscosity can be neglected in Equation (4.96) or (4.97) for the limiting case $y^+ \to \infty$. As noted above, we refer to the form of the differential equations in this limit as the **log-layer equations**. Thus, we conclude that in the log layer we can neglect convection, pressure gradient and molecular diffusion. The momentum equation thus simplifies to the following equation.

$$0 = \frac{\partial}{\partial y}\left[\nu_T \frac{\partial U}{\partial y}\right] \tag{4.98}$$

To the same degree of approximation, in the log layer, the $k$-$\omega$ model equations simplify to:

**$k$-$\omega$ Model:**

$$\left.\begin{aligned} 0 &= \nu_T \left(\frac{\partial U}{\partial y}\right)^2 - \beta^* \omega k + \sigma^* \frac{\partial}{\partial y}\left[\nu_T \frac{\partial k}{\partial y}\right] \\ 0 &= \alpha \left(\frac{\partial U}{\partial y}\right)^2 - \beta \omega^2 + \sigma \frac{\partial}{\partial y}\left[\nu_T \frac{\partial \omega}{\partial y}\right] \\ \nu_T &= k/\omega \end{aligned}\right\} \tag{4.99}$$

As can be shown by direct substitution, the solution to Equations (4.98) and (4.99) is

$$U = \frac{u_\tau}{\kappa} \ell n y + \text{constant}, \qquad k = \frac{u_\tau^2}{\sqrt{\beta^*}}, \qquad \omega = \frac{u_\tau}{\sqrt{\beta^*}\kappa y} \tag{4.100}$$

where the implied value of the Kármán constant, $\kappa$, is given by

$$\kappa^2 = \sqrt{\beta^*}(\beta/\beta^* - \alpha)/\sigma \tag{4.101}$$

Note that the term proportional to $\sigma^*$ disappears because $\partial k/\partial y = 0$. For the closure coefficient values specified by Wilcox [Equation (4.36)], we find $\kappa = 0.408$. We discussed the log-layer solution in Section 4.4 to illustrate how values for some of the closure coefficients have been selected. There are additional features of the solution worthy of mention. For example, the eddy viscosity varies linearly with distance from the surface and is given by

$$\nu_T = \kappa u_\tau y \tag{4.102}$$

This variation is equivalent to the mixing-length variation, $\ell_{mix} = \kappa y$. Also, the ratio of the Reynolds shear stress to the turbulence energy is constant, i.e.,

$$\tau_{xy} = \sqrt{\beta^*}\rho k \tag{4.103}$$

In a similar way, the $k$-$\epsilon$ model equations simplify to the following:

**$k$-$\epsilon$ Model:**

$$\left.\begin{aligned} 0 &= \nu_T \left(\frac{\partial U}{\partial y}\right)^2 - \epsilon + \frac{\partial}{\partial y}\left[\frac{\nu_T}{\sigma_k}\frac{\partial k}{\partial y}\right] \\ 0 &= C_{\epsilon 1} C_\mu k \left(\frac{\partial U}{\partial y}\right)^2 - C_{\epsilon 2}\frac{\epsilon^2}{k} + \frac{\partial}{\partial y}\left[\frac{\nu_T}{\sigma_\epsilon}\frac{\partial \epsilon}{\partial y}\right] \\ \nu_T &= C_\mu k^2/\epsilon \end{aligned}\right\} \tag{4.104}$$

The solution to Equations (4.98) and (4.104) is

$$U = \frac{u_\tau}{\kappa}\ell n y + \text{constant}, \qquad k = \frac{u_\tau^2}{\sqrt{C_\mu}}, \qquad \epsilon = \frac{u_\tau^3}{\kappa y} \tag{4.105}$$

where we again find an implied value for the Kármán constant, $\kappa$, viz.,

$$\kappa^2 = \sqrt{C_\mu}(C_{\epsilon 2} - C_{\epsilon 1})\sigma_\epsilon \tag{4.106}$$

Using the closure coefficient values for the Standard $k$-$\epsilon$ model [Equation (4.43)], the value of $\kappa$ is 0.433.

Keep in mind that the turbulent boundary layer consists of the sublayer and the defect layer. The sublayer is a thin near-wall region, while the defect layer constitutes most of the boundary layer. In the spirit of matched asymptotic expansions, the log layer is the overlap region which, in practice, often appears to be much thicker than the sublayer (see Figure 3.7). Part of our reason for focusing on this region of the boundary layer is of historical origin. Aside from the $k$-$\omega$ model, most two-equation

models fail to agree satisfactorily with experiment in the viscous sublayer unless the coefficients are made empirical functions of an appropriate turbulence Reynolds number. Consequently, the log-layer solution has often been used as a replacement for the no-slip boundary condition. Most $k$-$\epsilon$ model solutions, for example, are generated by enforcing the asymptotic behavior given in Equation (4.105). We must postpone further discussion of surface boundary conditions pending detailed analysis of the sublayer. Analysis of the log layer can also prove useful in determining leading-order effects of complicating factors such as surface curvature, coordinate-system rotation, and compressibility. As our most immediate goal, we have, in effect, done our matching in advance. Thus, we are now in a position to analyze the defect layer and the sublayer independent of one another. We turn first to the defect layer.

### 4.6.2 The Defect Layer

In this subsection we use singular perturbation methods to analyze model-predicted structure of the classical defect layer, including effects of pressure gradient. Our analysis includes three turbulence models, viz.: the Wilcox $k$-$\omega$ model; the Standard $k$-$\epsilon$ model; and the Wilcox-Rubesin (1980) $k$-$\omega^2$ model. First, we generate the perturbation solution. Next, we compare solutions for the three models in the absence of pressure gradient. Then, effects of pressure gradient are studied for the three models. Finally, as promised in Section 4.4, we justify the values chosen for $\sigma$ and $\sigma^*$ in the $k$-$\omega$ model.

To study the defect layer, we continue to confine our analysis to incompressible flow so that we begin with Equations (4.86) and (4.87). The perturbation expansion for the defect layer proceeds in terms of the ratio of friction velocity to the boundary-layer-edge velocity, $u_\tau/U_e$, and the dimensionless coordinates, $\xi$ and $\eta$, defined by

$$\xi = x/L \quad \text{and} \quad \eta = y/\Delta(x); \quad \Delta = U_e\delta^*/u_\tau \tag{4.107}$$

where $\delta^*$ is displacement thickness and $L$ is a characteristic streamwise length scale that is presumed to be very large compared to $\delta^*$. As in our approach to the log layer, we first establish the general form of the solution for the mean momentum equation. We expand the streamfunction and kinematic eddy viscosity as follows.

$$\psi_{outer}(x,y) \sim U_e\Delta\left[\eta - \frac{u_\tau}{U_e}F_1(\xi,\eta) + o\left(\frac{u_\tau}{U_e}\right)\right] \tag{4.108}$$

$$\nu_{T_{outer}}(x,y) \sim U_e\delta^*\left[N_0(\xi,\eta) + o(1)\right] \tag{4.109}$$

Observe that, as is so often the case in perturbation analysis, we needn't continue the expansions beyond the first one or two terms to capture most of the important features of the solution. For the specified streamfunction, the velocity becomes:

$$U(x,y) \sim U_e \left[1 - \frac{u_\tau}{U_e} U_1(\xi,\eta) + o\left(\frac{u_\tau}{U_e}\right)\right]; \quad U_1 = \frac{\partial F_1}{\partial \eta} \tag{4.110}$$

Substituting Equations (4.107) - (4.110) into the mean conservation equations [Equations (4.86) and (4.87)] yields the transformed momentum equation, viz.,

$$2\sigma_T \xi \frac{\partial U_1}{\partial \xi} = (\alpha_T - 2\beta_T - 2\omega_T)\eta \frac{\partial U_1}{\partial \eta} + (\beta_T - 2\omega_T) U_1 + \frac{\partial}{\partial \eta}\left[N_0 \frac{\partial U_1}{\partial \eta}\right] \tag{4.111}$$

where the parameters $\alpha_T$, $\beta_T$, $\sigma_T$ and $\omega_T$ are defined in terms of $\delta^*$, $u_\tau$ and skin friction, $c_f = 2(u_\tau/U_e)^2$, i.e.,

$$\alpha_T \equiv \frac{2}{c_f}\frac{d\delta^*}{dx}, \quad \beta_T \equiv \frac{\delta^*}{\tau_w}\frac{dP}{dx}, \quad \sigma_T \equiv \frac{\delta^*}{c_f x}, \quad \omega_T \equiv \frac{\delta^*}{c_f u_\tau}\frac{du_\tau}{dx} \tag{4.112}$$

Equation (4.111) must be solved subject to two boundary conditions. First, to satisfy the requirement that $U \to U_e$ as $y \to \infty$, necessarily

$$U_1 \to 0 \quad \text{as} \quad \eta \to \infty \tag{4.113}$$

Also, we must asymptote to the log-layer solution as $\eta \to 0$. One way to insure this is to insist that

$$\frac{\partial U_1}{\partial \eta} \to -\frac{1}{\kappa \eta} \quad \text{as} \quad \eta \to 0 \tag{4.114}$$

At this point, we have not greatly simplified our problem. Equation (4.111), like the original momentum equation, is a partial differential equation. The only simplification thus far is that molecular viscosity is negligible relative to the eddy viscosity. However, even this is not necessarily advantageous since the no-slip velocity boundary condition has been replaced by singular behavior approaching the surface. And, of course, we are now working in a transformed coordinate system $(\xi,\eta)$ rather than the familiar Cartesian coordinate system $(x,y)$. So why go to all this trouble? The answer is, we have only just begun.

Reexamination of the steps we have taken thus far should reveal a familiar tack; specifically, we appear to be developing a similarity solution. Indeed this is intentional, and inspection of Clauser's defect law [Equation (4.85)] shows that there has been method in our madness. Comparison

of Equation (4.85) with the assumed form of our perturbation expansion for $U$ given in Equation (4.110) shows that $U_1$ must be a function only of $\eta$. Thus, we now pose the question as to what conditions must be satisfied in order for a similarity solution to exist.

Clearly, the coefficients $\alpha_T$, $\beta_T$ and $\omega_T$ must be independent of $x$, for then the coefficients of all terms on the right-hand side of Equation (4.111) will be independent of $x$. The coefficient $\sigma_T$ is of no consequence since, if $U_1$ is independent of $x$, the left-hand side of Equation (4.111) vanishes regardless of the value of $\sigma_T$. The coefficient $\omega_T$ is also unimportant because, to leading order, it is zero. This becomes obvious if we now perform the formal matching of the defect-layer and sublayer solutions. As shown in the preceding section,

$$U_{inner}(\xi, y^+) \sim u_\tau \left[\frac{1}{\kappa}\ell n y^+ + B\right] \quad \text{as} \quad y^+ \to \infty \tag{4.115}$$

Assuming that a similarity solution exists so that $U_1$ depends only upon $\eta$, straightforward substitution into Equation (4.111) with a vanishing left-hand side shows that

$$U_1 \sim \frac{1}{\kappa}[-\ell n\eta + u_0 - u_1\eta\ell n\eta + \cdots] \quad \text{as} \quad \eta \to 0 \tag{4.116}$$

where the constants $u_0$, $u_1$, ... depend upon the complete solution which, in turn, depends upon what turbulence model is used. We now do a formal matching of the inner and outer expansions noting that $y^+ = \eta Re_{\delta^*}$ and $U_{outer}(\xi, \eta) \sim [U_e - u_\tau U_1(\eta) + \cdots]$. To match through first order, we require the following:

$$\left[\frac{1}{\kappa}\ell n y^+ + B\right] - \left[\frac{U_e}{u_\tau} + \frac{1}{\kappa}\ell n\eta - \frac{u_0}{\kappa}\right] \to 0 \quad \text{as} \quad y^+ \to \infty, \ \eta \to 0 \tag{4.117}$$

Hence, we conclude from matching that:

$$\frac{U_e}{u_\tau} = \left(B + \frac{u_0}{\kappa}\right) + \frac{1}{\kappa}\ell n Re_{\delta^*} \tag{4.118}$$

This is a useful result that enables us to compute the skin friction from our defect-layer solution, a point we will return to later. For our present purpose, Equation (4.118) provides us with an estimate of the orders of magnitude of $u_\tau$ and $c_f$, i.e.,

$$u_\tau \sim \frac{U_e}{\ell n Re_{\delta^*}} \quad \text{and} \quad c_f \sim \frac{1}{\ell n^2 Re_{\delta^*}} \quad \text{as} \quad Re_{\delta^*} \to \infty \tag{4.119}$$

As a consequence, estimating that $d\delta^*/dx \sim \delta^*/x$, we expect to have

$$\frac{du_\tau}{dx} \sim \frac{U_e}{Re_{\delta^*}\ell n^2 Re_{\delta^*}}\frac{\delta^*}{x} \sim \frac{U_e}{x\,\ell n^2 Re_{\delta^*}} \tag{4.120}$$

Substituting Equations (4.119) and (4.120) into the definition of $\omega_T$ [see Equation (4.112)], we arrive at the important result

$$\omega_T \sim \frac{\delta^*}{x}\ell n Re_{\delta^*} \sim o(1) \quad \text{as} \quad x \to \infty \tag{4.121}$$

The validity of the final estimate follows from the fact that $\ell n Re_{\delta^*}$ is transcendentally small compared to any power of $Re_{\delta^*}$, and $\delta^* \ll x$ as $x \to \infty$.

Thus, we can ignore the parameter $\omega_T$ in solving for $U_1$, although it will appear in the equation at some higher order. This leaves us with the reduced requirement for existence of a similarity solution that only $\alpha_T$ and $\beta_T$ are independent of $x$. However, we can also show that $\alpha_T$ and $\beta_T$ are uniquely related to leading order. To see this, we examine the classical momentum-integral equation that follows from integrating the mean-momentum equation across the boundary layer [c.f., Schlichting (1979)], viz.,

$$\frac{c_f}{2} = \frac{d\theta}{dx} - (2+H)\frac{\theta}{\rho U_e^2}\frac{dP}{dx} \tag{4.122}$$

where $\theta$ is momentum thickness and $H = \delta^*/\theta$ is the shape factor. In terms of $\alpha_T$ and $\beta_T$, the momentum-integral equation can be rewritten as

$$\alpha_T \frac{d\theta}{dx} = \left[1 + \frac{(2+H)}{H}\beta_T\right]\frac{d\delta^*}{dx} \tag{4.123}$$

If we evaluate the displacement and momentum thickness using our perturbation expansion for the velocity profile we find two important facts. First, evaluating the displacement thickness integral yields an integral constraint on our solution for $U_1$, $U_2$, etc. Second, we find to leading order that $\delta^*$ and $\theta$ are equal, i.e., the shape factor approaches 1 as $Re_{\delta^*} \to \infty$ and/or $u_\tau/U_e \to 0$. The proof of these facts is straightforward and thus left for the Problems section; the results are:

$$\int_0^\infty U_1(\eta)\, d\eta = 1 \tag{4.124}$$

$$\int_0^\infty U_n(\eta)\, d\eta = 0, \qquad n \geq 2 \tag{4.125}$$

and

$$H \sim 1 + O\left(\frac{u_\tau}{U_e}\right) \quad \text{as} \quad Re_{\delta^*} \to \infty, \ \frac{u_\tau}{U_e} \to 0 \tag{4.126}$$

Note that the perturbation solution for $U_1(\eta)$ provides sufficient information to determine the $O(u_\tau/U_e)$ term (see Problems section). Hence, Equation (4.123) yields the following relationship between $\alpha_T$ and $\beta_T$.

$$\alpha_T = 1 + 3\beta_T \tag{4.127}$$

Thus, the requirement for existence of a similarity solution to Equation (4.111) for large Reynolds number is simply that the **equilibrium parameter**, $\beta_T$, be constant. This is a very satisfactory state of affairs because it is consistent with experimental observations at finite (laboratory-scale) Reynolds numbers. That is, Clauser found that, above the viscous sublayer, turbulent boundary layers assume a self-similar form when the equilibrium parameter is constant. The problem we must solve to determine $U_1(\eta)$ is:

$$\frac{d}{d\eta}\left[N_0 \frac{dU_1}{d\eta}\right] + (1+\beta_T)\eta\frac{dU_1}{d\eta} + \beta_T U_1 = 0 \tag{4.128}$$

$$\frac{dU_1}{d\eta} \to -\frac{1}{\kappa\eta} \quad \text{as} \quad \eta \to 0 \quad \text{and} \quad U_1(\eta) \to 0 \quad \text{as} \quad \eta \to \infty \tag{4.129}$$

The integral constraint, Equation (4.124), must also be enforced. The dimensionless eddy viscosity, $N_0(\eta)$, depends upon the turbulence model selected. For our purposes, we will consider three different turbulence models, viz.: the Wilcox $k$-$\omega$ model [Equations (4.33)-(4.36)]; the Standard $k$-$\epsilon$ model [Equations (4.40)-(4.43)]; and the Wilcox-Rubesin (1980) $k$-$\omega^2$ model whose equations are as follows.

**Eddy Viscosity**

$$\mu_T = \rho k/\omega \tag{4.130}$$

**Turbulence Kinetic Energy**

$$\rho\frac{\partial k}{\partial t} + \rho U_j \frac{\partial k}{\partial x_j} = \tau_{ij}\frac{\partial U_i}{\partial x_j} - \beta^*\rho k\omega + \frac{\partial}{\partial x_j}\left[(\mu + \sigma^*\mu_T)\frac{\partial k}{\partial x_j}\right] \tag{4.131}$$

**Specific Dissipation Rate**

$$\rho\frac{\partial \omega^2}{\partial t} + \rho U_j \frac{\partial \omega^2}{\partial x_j} = \alpha\frac{\omega^2}{k}\tau_{ij}\frac{\partial U_i}{\partial x_j} - \left[\beta + 2\sigma\frac{\partial \ell}{\partial x_j}\frac{\partial \ell}{\partial x_j}\right]\rho\omega^3 \tag{4.132}$$

$$+\frac{\partial}{\partial x_j}\left[(\mu + \sigma\mu_T)\frac{\partial \omega^2}{\partial x_j}\right] \tag{4.133}$$

**Closure Coefficients**

$$\alpha = 10/9, \quad \beta = 3/20, \quad \beta^* = 9/100, \quad \sigma = 1/2, \quad \sigma^* = 1/2 \tag{4.134}$$

**Auxiliary Relations**

$$\epsilon = \beta^* \omega k \quad \text{and} \quad \ell = k^{1/2}/\omega \tag{4.135}$$

Making standard boundary-layer approximations for the model equations, we seek a perturbation solution for $k$, $\omega$ and $\epsilon$ of the following form.

$$\left.\begin{aligned} k &\sim \frac{u_\tau^2}{\sqrt{\beta^*}}[K_0(\eta) + o(1)] \\ \omega &\sim \frac{u_\tau}{\sqrt{\beta^*}\Delta}[W_0(\eta) + o(1)] \\ \epsilon &\sim \frac{u_\tau^3}{\Delta}[E_0(\eta) + o(1)] \end{aligned}\right\} \tag{4.136}$$

Note that for the $k$-$\epsilon$ model, $\beta^* = C_\mu$. For all three turbulence models, the transformed equation for $k$ can be written as

**All Models:**

$$\sigma^* \frac{d}{d\eta}\left[N_0 \frac{dK_0}{d\eta}\right] + (1+\beta_T)\eta \frac{dK_0}{d\eta} + \sqrt{\beta^*}\left[N_0 \left(\frac{dU_1}{d\eta}\right)^2 - E_0\right] = 0 \tag{4.137}$$

where, for the $k$-$\epsilon$ model, we note that $\sigma^* = 1/\sigma_k$. The second equation and auxiliary equations are specific to each model. The transformed equations are:

***k*-$\omega$ Model:**

$$\left.\begin{aligned} &\sigma \frac{d}{d\eta}\left[N_0 \frac{dW_0}{d\eta}\right] + (1+\beta_T)\eta \frac{dW_0}{d\eta} + (1+2\beta_T)W_0 \\ &+\sqrt{\beta^*}\left[\alpha \left(\frac{dU_1}{d\eta}\right)^2 - \frac{\beta}{\beta^*} W_0^2\right] = 0 \\ &N_0 = K_0/W_0 \quad \text{and} \quad E_0 = K_0 W_0 \end{aligned}\right\} \tag{4.138}$$

***k*-$\omega^2$ Model:**

$$\left.\begin{aligned} &\sigma \frac{d}{d\eta}\left[N_0 \frac{dW_0^2}{d\eta}\right] + (1+\beta_T)\eta \frac{dW_0^2}{d\eta} + 2(1+2\beta_T)W_0^2 \\ &+\sqrt{\beta^*}\left[\alpha W_0 \left(\frac{dU_1}{d\eta}\right)^2 - \left\{\frac{\beta}{\beta^*} + 2\sigma\left(\frac{dL_0}{d\eta}\right)^2\right\} W_0^3\right] = 0 \\ &N_0 = K_0/W_0, \quad E_0 = K_0 W_0, \quad \text{and} \quad L_0 = K_0^{1/2}/W_0 \end{aligned}\right\} \tag{4.139}$$

**$k$-$\epsilon$ Model:**

$$\left.\begin{aligned} &\sigma_\epsilon^{-1}\frac{d}{d\eta}\left[N_0\frac{dE_0}{d\eta}\right]+(1+\beta_T)\eta\frac{dE_0}{d\eta}+(1+2\beta_T)E_0 \\ &+\sqrt{C_\mu}\left[C_{\epsilon 1}K_0\left(\frac{dU_1}{d\eta}\right)^2-C_{\epsilon 2}\frac{E_0^2}{K_0}\right]=0 \\ &N_0=K_0^2/E_0 \quad \text{and} \quad E_0=K_0W_0 \end{aligned}\right\} \tag{4.140}$$

We must specify boundary conditions on $K_0$, $W_0$ and $E_0$ both in the freestream and approaching the surface. For non-turbulent flow in the freestream, we require that the turbulence parameters all vanish as $\eta \to \infty$. However, we also stipulate that these quantities approach zero in such a way that $N_0$ vanishes. Thus, the freestream boundary conditions are:

$$K_0(\eta)\to 0,\ \ W_0(\eta)\to 0,\ \ E_0(\eta)\to 0,\ \ U_1(\eta)\to 0 \ \text{ as } \ \eta\to\infty \tag{4.141}$$

As it turns out, we can also specify $W_0 = \sqrt{\beta^*}(1+2\beta_T)/\beta$ for the $k$-$\omega$ model and $W_0 = 2\sqrt{\beta^*}(1+2\beta_T)/\beta$ for the $k$-$\omega^2$ model. Regardless of the choice of $W_0$, neither model displays the excessive sensitivity to freestream values observed for the $k$-$\omega$ model in free shear flows.

Approaching the surface, we must formally match to the law of the wall. Matching is a bit different for each model but is nevertheless straightforward; details of the algebra will thus be omitted in the interest of brevity. The limiting forms used for $\eta \to 0$ follow.

$$\left.\begin{aligned} K_0(\eta) &\sim [1+k_1\eta\ell n\eta+\cdots] \\ E_0(\eta) &\sim \frac{1}{\kappa\eta}[1+e_1\eta\ell n\eta+\cdots] \\ W_0(\eta) &\sim \frac{1}{\kappa\eta}[1+w_1\eta\ell n\eta+\cdots] \\ U_1(\eta) &\sim \frac{1}{\kappa}[-\ell n\eta+u_0-u_1\eta\ell n\eta+\cdots] \end{aligned}\right\} \tag{4.142}$$

The coefficients $k_1$, $u_1$, $w_1$ and $e_1$ are as follows, where for notational consistency, we define

$$\alpha^* \equiv \sqrt{\beta^*} = \sqrt{C_\mu} \tag{4.143}$$

Also, we again write some of the results in terms of $\sigma^*$ with the understanding that $\sigma^* = 1/\sigma_k$ for the $k$-$\epsilon$ model.

**All Models:**

$$k_1 = \frac{\beta_T/\kappa}{\sigma^*\kappa^2/(2\alpha^*) - 1} \tag{4.144}$$

**$k$-$\omega$ Model:**

$$\left.\begin{aligned} u_1 &= \frac{[\beta/(\alpha\beta^*)][\sigma^*\kappa^2/(2\alpha^*)]}{1-\beta/(\alpha\beta^*)}\ k_1 \\ w_1 &= \frac{\sigma^*\kappa^2/(2\alpha^*)}{1-\beta/(\alpha\beta^*)}\ k_1 \end{aligned}\right\} \tag{4.145}$$

**$k$-$\omega^2$ Model:**

$$\left.\begin{aligned} u_1 &= \frac{[\beta/\alpha^*][\sigma^*\kappa^2/(2\alpha^*)] + \sigma\kappa^2}{2\alpha\alpha^*[1-\beta/(\alpha\beta^*)] + 2\sigma\kappa^2}\ k_1 \\ w_1 &= \frac{\alpha\alpha^*[\sigma^*\kappa^2/(2\alpha^*)] + \sigma\kappa^2}{2\alpha\alpha^*[1-\beta/(\alpha\beta^*)] + 2\sigma\kappa^2}\ k_1 \end{aligned}\right\} \tag{4.146}$$

**$k$-$\epsilon$ Model:**

$$\left.\begin{aligned} u_1 &= \frac{(1+\sigma^*\kappa^2/\alpha^*)C_{\epsilon 2} - C_{\epsilon 1}}{2(C_{\epsilon 1} - C_{\epsilon 2})}\ k_1 \\ e_1 &= \frac{(1+\sigma^*\kappa^2/\alpha^*)C_{\epsilon 1} - C_{\epsilon 2}}{2(C_{\epsilon 1} - C_{\epsilon 2})}\ k_1 \end{aligned}\right\} \tag{4.147}$$

Additionally, the coefficient $u_0$ is determined from the integral constraint for mass conservation, which is guaranteed by the integral constraint in Equation (4.124). Table 4.3 summarizes the equations for the leading-order terms in the defect-layer solution.

Before proceeding to discussion of the defect-layer similarity solution, there are two quantities of interest that follow from the leading order solution, viz., the skin friction, $c_f$, and Coles' **wake-strength parameter**, $\tilde{\pi}$. Recall that from matching defect-layer and sublayer velocity profiles, we deduced Equation (4.118). Noting that $c_f = 2(u_\tau/U_e)^2$, we conclude that

$$\sqrt{\frac{2}{c_f}} = (B + \frac{u_0}{\kappa}) + \frac{1}{\kappa}\ell n Re_{\delta^*} \tag{4.148}$$

The **composite law of the wall, law of the wake** profile according to Coles' meticulous correlation of experimental data [see Coles and Hirst (1969)] is given by

$$U^+ = \frac{1}{\kappa}\ell n y^+ + B + \frac{2\tilde{\pi}}{\kappa}\sin^2\left(\frac{\pi}{2}\frac{y}{\delta}\right) \tag{4.149}$$

Table 4.3: Summary of the Defect-Layer Equations

| | |
|---|---|
| Mass (Integral Constraint) | Equation (4.124) |
| Momentum | Equation (4.128) |
| Turbulence Kinetic Energy | Equation (4.137) |
| Specific Dissipation ($k$-$\omega$ Model) | Equation (4.138) |
| Specific Dissipation ($k$-$\omega^2$ Model) | Equation (4.139) |
| Dissipation ($k$-$\epsilon$ Model) | Equation (4.140) |
| Boundary Conditions for $\eta \rightarrow \infty$ | Equation (4.141) |
| Boundary Conditions for $\eta \rightarrow 0$ | Equation (4.142) |

The $\sin^2$ function is purely a curve fit: several other functions have been suggested, including forms that yield $\partial U/\partial y = 0$ at $y = \delta$ [which is not the case for Equation (4.149)]. Defect-layer solutions include sharp turbulent-nonturbulent interfaces so that the edge of the defect-layer lies at a finite value $\eta = \eta_e$. Thus, combining Equations (4.118) and (4.149) leads to the following expression for the wake-strength parameter.

$$\tilde{\pi} = \frac{1}{2}(u_0 - \ell n \eta_e) \tag{4.150}$$

Figure 4.9(a) compares the defect-layer solution for the three models with corresponding experimental data of Wieghardt as tabulated by Coles and Hirst (1969). The experimental data presented are those at the highest Reynolds number for which data are reported. This is consistent with the defect-layer solution that is formally valid for very large Reynolds number. As shown, all three models predict velocity profiles that differ from measured values by no more than about three percent of scale. Interestingly, the $k$-$\omega$ model shows the smallest differences from the Wieghardt data. Corresponding computed and measured skin friction values are summarized in the insert on Figure 4.9(a); the largest difference is less than three percent. Thus, based on analysis of the constant-pressure defect layer, there is little difference amongst the three models.

Turning now to the effect of pressure gradient, we consider defect-layer solutions for the equilibrium parameter, $\beta_T$, ranging from -0.5 to +9.0, where positive $\beta_T$ corresponds to an adverse pressure gradient. The choice of this range of $\beta_T$ has been dictated by the requirement of the perturbation solution that $\beta_T$ be constant. This appears to be the maximum range over which experimental data have been taken with $\beta_T$ more-or-less constant.

Figure 4.9(b) compares computed velocity profiles with experimental data of Clauser [see Coles and Hirst (1969)] for $\beta_T = 8.7$. As with the

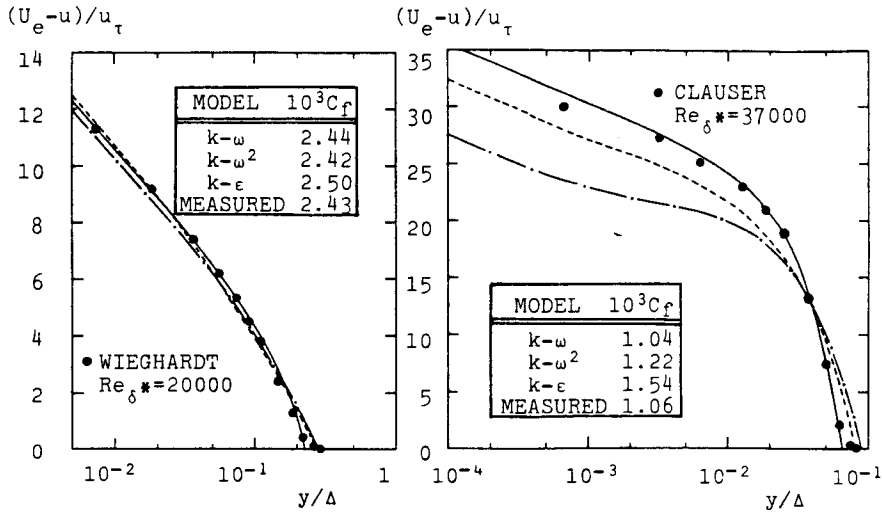


(a) $\beta_T = 0$ (b) $\beta_T = 8.7$

Figure 4.9: Computed and measured defect-layer velocity profiles; —— $k$-$\omega$ model; - - - $k$-$\omega^2$ model; – · – $k$-$\epsilon$ model. [From Wilcox (1988a) — Copyright © AIAA 1988 — Used with permission.]

constant pressure case, computed and measured skin friction are included in the insert. As shown, the $k$-$\omega$ model yields a velocity profile and skin friction closest to measurements while the $k$-$\epsilon$ model shows the greatest differences. The $k$-$\omega^2$ profile and skin friction lie about midway between those of the other two models.

Figure 4.10 compares computed wake strength, $\tilde{\pi}$, with values inferred by Coles and Hirst (1969) from experimental data. Inspection of Figure 4.10 reveals provocative differences amongst the three models. Most notably, the $k$-$\omega$ model yields wake strengths closest to values inferred from data over the complete range considered. Consistent with the velocity profile discrepancies shown in Figure 4.9(b), the $k$-$\epsilon$ model exhibits the largest differences, with predicted wake strength 50%-100% lower than inferred values when $\beta_T$ is as small as two!

The explanation of the $k$-$\epsilon$ model's poor performance for adverse pressure gradient can be developed from inspection of the asymptotic behavior

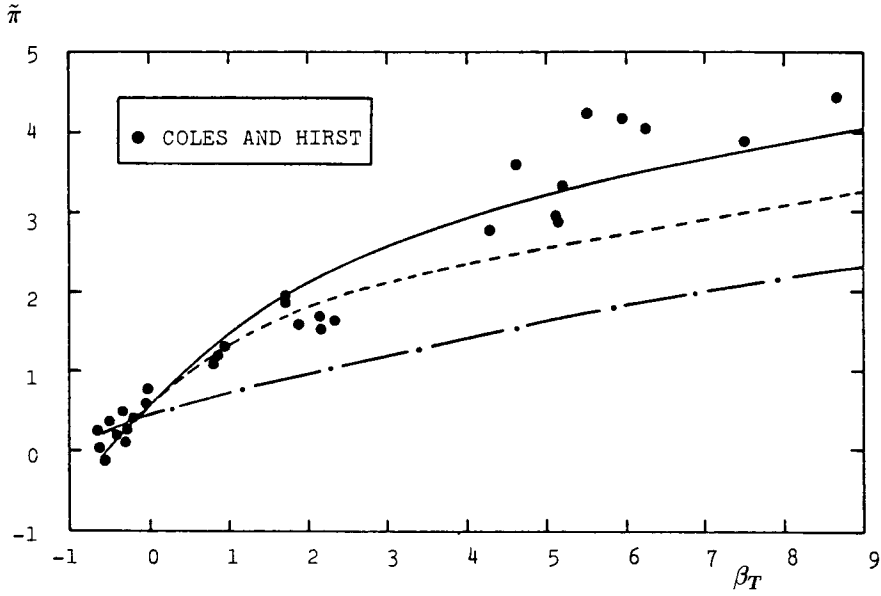


Figure 4.10: Computed and measured wake-strength parameter; —— $k$-$\omega$ model; - - - $k$-$\omega^2$ model; – · – $k$-$\epsilon$ model. [From Wilcox (1988a) — Copyright © AIAA 1988 — Used with permission.]

of solutions as $\eta \to 0$. For the models analyzed, the velocity behaves as

$$\frac{U_e - U}{u_\tau} \sim -\frac{1}{\kappa}\ell n\eta + A - \beta_T C\eta\ell n\eta + \cdots \quad \text{as} \quad \eta \to 0 \tag{4.151}$$

where Table 4.4 summarizes the constants $A$ and $C$. Note that, while the coefficient $A = u_0/\kappa$ is determined as part of the solution (from the integral constraint that mass be conserved), the coefficient $C = u_1/(\beta_T\kappa)$ follows directly from the limiting form of the solution as $\eta \to 0$. As seen from Table 4.4, $C$ is largest for the $k$-$\epsilon$ model and is smallest for the $k$-$\omega$ model. The presence of the $\eta\ell n\eta$ term gives rise to an inflection in the velocity profile as $\eta \to 0$ that is most pronounced for the $k$-$\epsilon$ model. In terms of turbulence properties, the turbulence length scale, $\ell$, behaves according to

$$\ell \sim (\beta^*)^{1/4}\kappa\eta[1 + \beta_T L\eta\ell n\eta + \cdots] \quad \text{as} \quad \eta \to 0 \tag{4.152}$$

Table 4.4 also includes the coefficient $L$ for each model. Again, we see that the contribution of the $\eta\ell n\eta$ term is largest for the $k$-$\epsilon$ model and smallest for the $k$-$\omega$ model. Thus, in the presence of adverse pressure gradient,

Table 4.4: Coefficients $A$, $C$ and $L$ for $\beta_T = 9$

| Model | $A$ | $C$ | $L$ |
|---|---|---|---|
| $k$-$\omega$ | 13.1 | 2.90 | -2.20 |
| $k$-$\omega^2$ | 9.8 | 6.39 | -3.62 |
| $k$-$\epsilon$ | 5.4 | 13.57 | -6.50 |

the $k$-$\epsilon$ model's turbulence length scale tends to be too large in the near-wall region. Note, of course, that this shortcoming is not evident in the constant-pressure case, which has $\beta_T = 0$.

The manner in which the $k$-$\omega$ model achieves smaller values of $\ell$ than does the $k$-$\epsilon$ model can be seen by changing dependent variables. That is, starting with the $k$-$\omega$ formulation and defining $\epsilon = \beta^* \omega k$, we can deduce the following incompressible equation for $\epsilon$ implied by the $k$-$\omega$ model.

$$U\frac{\partial \epsilon}{\partial x} + V\frac{\partial \epsilon}{\partial y} = (1+\alpha)k\left(\frac{\partial U}{\partial y}\right)^2 - (1+\beta/\beta^*)\frac{\epsilon^2}{k} + \frac{\partial}{\partial y}\left[\sigma\nu_T\frac{\partial \epsilon}{\partial y}\right] - 2\sigma\nu_T\frac{\partial k}{\partial y}\frac{\partial(\epsilon/k)}{\partial y} \tag{4.153}$$

All terms except the last on the right-hand side of Equation (4.153) are identical in form to those of the Standard $k$-$\epsilon$ model [see Equation (4.42)]. This so-called **cross-diffusion term** is negligibly small as $\eta \to 0$ for constant-pressure boundary layers because $k \to$ constant as $\eta \to 0$. However, $\partial k/\partial y$ is nonvanishing when $\beta_T \neq 0$ and $\partial(\epsilon/k)/\partial y$ generally is quite large as $\eta \to 0$. The net effect of this additional term is to suppress the rate of increase of $\ell$ close to the surface.

Unlike the three closure coefficients discussed in Section 4.4, simple arguments have not been found to establish the values of $\sigma$ and $\sigma^*$ for the $k$-$\omega$ model. In Subsection 4.6.3, we will find that using $\sigma = 1/2$ yields an excellent solution in the viscous sublayer, almost independent of the value of $\sigma^*$. Equation (4.145) shows that the coefficient $C$ is proportional to $\sigma^*$, so that smaller values of $\sigma^*$ should improve the model's predictions for boundary layers with variable pressure. The computed variation of $\tilde{\pi}$ with $\beta_T$ (Figure 4.10) closely matches experimental results when $\sigma^* = 1/2$, and this is the value that has been chosen for the $k$-$\omega$ model.

### 4.6.3 The Viscous Sublayer

In order to facilitate integration of the model equations through the viscous sublayer, we must, at a minimum, have molecular diffusion terms in the equations of motion. Potentially, we might also have to allow the various closure coefficients to be functions of viscosity (i.e., turbulence Reynolds number) as well. This should come as no surprise since even the mixing-length model requires the Van Driest damping factor and one-equation models need similar viscous damping [Wolfshtein (1967)]. In this section, we use perturbation methods to analyze viscous sublayer structure predicted by several two-equation models. As we will see, with the exception of some $k$-$\omega$ models, virtually all two-equation models require Reynolds number dependent corrections in order to yield a realistic sublayer solution.

We have already derived the sublayer solution in Subsection 4.6.1 when we discussed the **log layer**. Recapping the highlights of the expansion procedure, the velocity is given by an expansion of the form

$$U(x,y) \sim u_\tau[\hat{u}_0(y^+) + Re_{\delta^*}^{-1}\hat{u}_1(\xi, y^+) + o(Re_{\delta^*}^{-1})] \tag{4.154}$$

To leading order, the convective terms and pressure gradient are negligible. Thus, for example, the leading order equations for the $k$-$\omega$ model expressed in terms of dimensional quantities are given by

$$\left.\begin{aligned}
&(\nu + \nu_T)\frac{dU}{dy} = u_\tau^2 \\
&\frac{d}{dy}\left[(\nu + \sigma^*\nu_T)\frac{dk}{dy}\right] + \nu_T\left(\frac{dU}{dy}\right)^2 - \beta^*\omega k = 0 \\
&\frac{d}{dy}\left[(\nu + \sigma\nu_T)\frac{d\omega}{dy}\right] + \alpha\left(\frac{dU}{dy}\right)^2 - \beta\omega^2 = 0 \\
&\nu_T = \frac{k}{\omega}
\end{aligned}\right\} \tag{4.155}$$

Because the Reynolds shear stress is constant, the viscous sublayer is often referred to as the **constant-stress layer**. Five boundary conditions are needed for this fifth-order system, two of which follow from matching to the law of the wall as $y^+ \to \infty$, viz.,

$$k \to \frac{u_\tau^2}{\sqrt{\beta^*}} \quad \text{and} \quad \omega \to \frac{u_\tau}{\sqrt{\beta^*}\kappa y} \quad \text{as} \quad y^+ \to \infty \tag{4.156}$$

where $y^+ \equiv u_\tau y/\nu$. Two more boundary conditions follow from **no slip** at

the surface, which implies that $U$ and $k$ vanish at $y = 0$. Thus,

$$U = k = 0 \quad \text{at} \quad y^+ = 0 \tag{4.157}$$

The final condition follows from examination of the differential equations for $k$ and $\omega$ approaching the surface. The $k$-$\omega$ model possesses two kinds of solutions. The first type of solution has a finite value of $\omega$ at the surface. This fact was first observed by Saffman (1970) who speculated that the constant in the law of the wall, $B$, would vary with the surface value of $\omega$. This feature is unique to $k$-$\omega$ and $k$-$\omega^2$ models and will be explored in detail in Section 4.7. The second type of solution is common to all two-equation models and this is the one we will focus on now. Examination of the differential equations approaching $y = 0$ shows that for all two-equation models,

$$k \sim y^n \quad \text{and} \quad \beta^* y^2 \omega / \nu \sim \text{constant} \quad \text{as} \quad y \to 0 \tag{4.158}$$

Table 4.5 lists the values of $n$ and the constant for several models. As shown, none of the models predicts the exact theoretical value of 2 for both $n$ and $\beta^* y^2 \omega / \nu$. This can only be accomplished with additional modification of the model equations.

Table 4.5: Sublayer Behavior Without Viscous Damping

| Model | Type | $B$ | $n$ | $\beta^* y^2 \omega / \nu$ |
|---|---|---|---|---|
| Wilcox-Rubesin (1980) | $k$-$\omega^2$ | 7.1 | 4.00 | 12.00 |
| Saffman (1970) | $k$-$\omega^2$ | 6.0 | 3.7-4.0 | 12.00 |
| Launder-Spalding (1972) | $k$-$\omega^2$ | 5.7 | 3.79 | 12.00 |
| Wilcox (1988a) | $k$-$\omega$ | 5.1 | 3.23 | 7.20 |
| Kolmogorov (1942) | $k$-$\omega$ | 3.1 | 3.62 | 7.20 |
| Launder-Sharma (1974) | $k$-$\epsilon$ | -2.2 | 1.39 | 0.53 |
| Speziale (1990) | $k$-$\tau$ | -2.2 | 1.39 | 0.53 |
| Exact/Measured | | 5.0 | 2.00 | 2.00 |

The exact values follow from expanding the fluctuating velocity in Taylor series near a solid boundary. That is, we know that the fluctuating velocity satisfies the no-slip boundary condition and also satisfies conservation of mass (see Section 2.3). Consequently, the three velocity components must behave as follows.

$$\left.\begin{aligned} u' &\sim A(x,z,t)y + O(y^2) \\ v' &\sim B(x,z,t)y^2 + O(y^3) \\ w' &\sim C(x,z,t)y + O(y^2) \end{aligned}\right\} \quad \text{as} \quad y \to 0 \tag{4.159}$$

Hence, the turbulence energy and dissipation are given by

$$k \sim \frac{1}{2}\left(\overline{A^2+C^2}\right) y^2 + O(y^3) \quad \text{and} \quad \epsilon \sim \nu\left(\overline{A^2+C^2}\right) + O(y) \tag{4.160}$$

Assuming that $\epsilon = \beta^* \omega k$, Equation (4.160) tells us that

$$k \sim y^2 \quad \text{and} \quad \beta^* y^2 \omega/\nu \sim 2 \quad \text{as} \quad y \to 0 \tag{4.161}$$

Hence, using the asymptotic behavior of $\omega$ for $y \to 0$ appropriate to each model as the fifth boundary condition, we can solve the sublayer equations (see Subsection 7.2.1 for an explanation of how to handle the singular behavior of $\omega$ numerically). One of the most interesting features of the solution is the constant in the law of the wall, $B$, that is evaluated from the following limit.

$$B = \lim_{y^+ \to \infty} \left[ U^+ - \frac{1}{\kappa} \ell n y^+ \right] \tag{4.162}$$

Table 4.5 also lists the computed value of $B$ for the various two-equation models. As shown, the Spalding $k$-$\omega^2$ and Wilcox $k$-$\omega$ models are sufficiently close to the standard value of 5.0 to be used with no additional viscous modifications. The Standard $k$-$\epsilon$ model and the Speziale et al. $k$-$\tau$ model are farthest from the generally accepted value for $B$.

Figure 4.11(a) compares $k$-$\omega$ model velocity profiles with corresponding measurements of Laufer (1952), Anderson, Kays and Moffat (1972), and Wieghardt [as tabulated by Coles and Hirst (1969)]. As shown, computed velocities generally fall within experimental data scatter. In Figure 4.11(b), we compare computed turbulence production and dissipation terms with Laufer's (1952) near-wall pipe-flow measurements. Again, predictions fall well within experimental error bounds.

This concludes our perturbation analysis of the turbulent boundary layer. As we have seen, using perturbation analysis, we have been able to dissect model-predicted structure of the defect layer, log layer and sublayer, never having to solve more than an ordinary differential equation. This is a great advantage in testing a turbulence model in light of the ease and accuracy with which ordinary differential equations can be solved. The equations are not trivial to solve however since we are dealing with two-point boundary-value problems, and the resulting systems of equations are of sixth order for the defect layer and fifth order for the sublayer. However, this is far easier to handle than the partial differential equations we started with, and parametric studies (e.g., varying the equilibrium parameter, $\beta_T$) are much simpler in the context of the perturbation solution. As a final comment, results obtained in this section should make the following statement obvious.

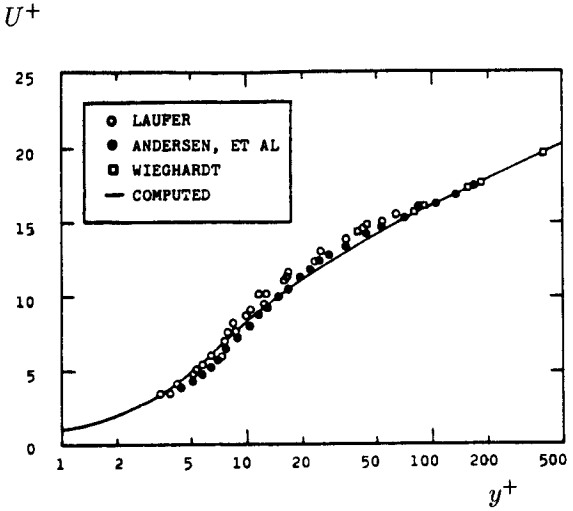


(a) Velocity

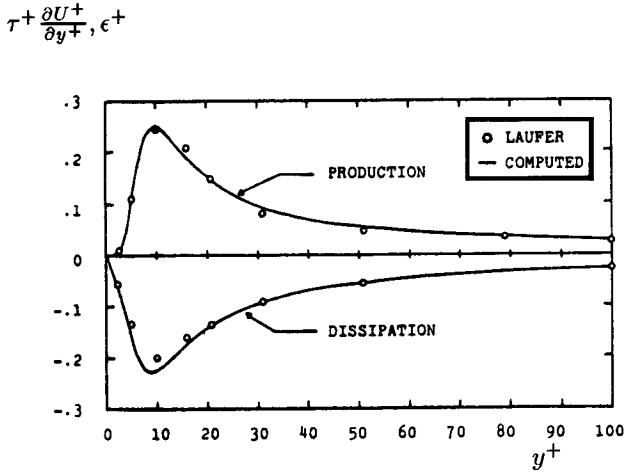


(b) Production and dissipation

Figure 4.11: Computed and measured sublayer properties; $k$-$\omega$ model. [From Wilcox (1988a) — Copyright © AIAA 1988 — Used with permission.]

**Given the demonstrated power and utility of perturbation analysis in analyzing the turbulent boundary layer, this type of analysis can, and should, be used in developing all turbulence models.**

## 4.7 Surface Boundary Conditions

In order to apply a two-equation turbulence model to wall-bounded flows, we must specify boundary conditions appropriate to a solid boundary for the velocity and the two turbulence parameters. As shown in the preceding section, most two-equation models fail to predict a satisfactory value of the constant $B$ in the law of the wall (see Table 4.5). Consequently, for most two-equation turbulence models, applying the no-slip boundary condition and integrating through the viscous sublayer yields unsatisfactory results. One approach we can take to remove this deficiency is to introduce viscous damping factors analogous to the Van Driest correction for the mixing-length model. Since introduction of damping factors accomplishes much more than allowing integration through the sublayer, we defer detailed discussion of such modifications to Section 4.9. An alternative approach is to circumvent the inability to predict a satisfactory log-layer solution by simply matching to the law of the wall using a suitable value for $B$. This is what we did in analyzing the defect layer, and the procedure is equally valid for general wall-bounded flows.

### 4.7.1 Wall Functions

Historically, researchers implementing this matching procedure have referred to the functional forms used in the limit $y \rightarrow 0$ as **wall functions**. This procedure uses the law of the wall as the constitutive relation between velocity and surface shear stress. That is, in terms of the velocity at the mesh point closest to the surface, we can regard the law of the wall, viz.,

$$U = u_\tau \left[ \frac{1}{\kappa} \ell n \left( \frac{u_\tau y}{\nu} \right) + B \right] \tag{4.163}$$

as a transcendental equation for the friction velocity and, hence, the shear stress. Once the friction velocity is known, we use Equations (4.100) for the $k$-$\omega$ model or Equations (4.105) for the $k$-$\epsilon$ model to define the values of $k$ and $\omega$ or $\epsilon$ at the grid points closest to the surface. Because $\omega$ and $\epsilon$ are odd functions of $u_\tau$ and both quantities are positive definite, care must be taken for separated flows. We can either use the absolute value of $u_\tau$ or

combine the equations for $k$ and $\omega$ or $k$ and $\epsilon$ so that the **wall functions** for $k$, $\omega$ and $\epsilon$ become:

$$k = \frac{u_\tau^2}{\sqrt{\beta^*}}, \quad \omega = \frac{k^{1/2}}{(\beta^*)^{1/4}\kappa y}, \quad \epsilon = (\beta^*)^{3/4}\frac{k^{3/2}}{\kappa y} \tag{4.164}$$

The wall-function approach is not entirely satisfactory for several reasons. Most importantly, numerical solutions generally are sensitive to the point above the surface where the wall functions are used, i.e., the point where the matching occurs (see Subsection 7.2.1 for an in-depth discussion of this problem). Furthermore, the law of the wall doesn't always hold for flow near solid boundaries, most notably for separated flows.

There is a more subtle danger attending the use of wall functions. Specifically, when poor results are obtained with a two-equation model, researchers sometimes mistakenly blame their difficulties on the use of non-optimum wall functions. This assessment is too often made when the wall functions are not the real cause of the problem. For example, the $k$-$\epsilon$ model just doesn't perform well for boundary layers with adverse pressure gradient. Many articles have appeared claiming that discrepancies between $k$-$\epsilon$ model predicted skin friction and corresponding measurements for such flows are caused by the wall functions. This incorrectly assumes that the surface shear is a localized force that depends only upon sublayer structure. As shown in the defect-layer solution of the preceding section, no viscous modification is likely to remove the curious inflection in the $k$-$\epsilon$ model's velocity profile unless viscous effects (unrealistically) penetrate far above the viscous sublayer. We mustn't lose sight of the fact that the momentum flux through a boundary layer affects the surface shear and vice versa [see Equation (4.122)]. Hence, inaccurate skin friction predictions go hand in hand with inaccuracies in the velocity profile throughout the layer.

As a final comment on wall functions, Wilcox (1989) demonstrates that pressure gradient must be included in order to achieve grid-independent solutions for flows with pressure gradient. Retaining pressure gradient in the log-layer equations (i.e., retaining $\beta_T/Re_{\delta^*}$), then the asymptotic behavior for the $k$-$\omega$ model approaching the surface is given by the following equations:

$$\left.\begin{aligned} U &= u_\tau\left[\frac{1}{\kappa}\ell n\left(\frac{u_\tau y}{\nu}\right) + B - 0.48\frac{u_\tau y}{\nu}\phi + O(\phi^2)\right] \\ k &= \frac{u_\tau^2}{\sqrt{\beta^*}}\left[1 + 1.16\frac{u_\tau y}{\nu}\phi + O(\phi^2)\right] \\ \omega &= \frac{u_\tau}{\sqrt{\beta^*}\kappa y}\left[1 - 0.32\frac{u_\tau y}{\nu}\phi + O(\phi^2)\right] \end{aligned}\right\} \tag{4.165}$$

where $\phi$ is the dimensionless pressure gradient parameter defined by

$$\phi = \frac{\nu}{\rho u_\tau^3} \frac{dP}{dx} \tag{4.166}$$

The expansions in Equation (4.165) have been derived assuming $\phi$ is a small parameter.

### 4.7.2 Surface Roughness

As noted in the preceding section, a key advantage of the $k$-$\omega^2$ and $k$-$\omega$ formulations over the $k$-$\epsilon$ formulation is the fact that $\omega$-oriented equations possess solutions in which the value of $\omega$ may be arbitrarily specified at the surface. This is an advantage because it provides a natural way to incorporate effects of surface roughness through surface boundary conditions. This feature of the equations was originally recognized by Saffman (1970). If we write the surface boundary condition on $\omega$ as

$$\omega = \frac{u_\tau^2}{\nu} S_R \quad \text{at} \quad y = 0 \tag{4.167}$$

we can generate sublayer solutions for arbitrary $S_R$, including the limiting cases $S_R \to 0$ and $S_R \to \infty$. Figure 4.12 shows the computed value of $B$ for a wide range of values of $S_R$. As shown, in the limit $S_R \to \infty$, $B$ tends to 5.1. In the limit $S_R \to 0$, an excellent correlation of the numerical predictions is given by

$$B \to 8.4 + \frac{1}{\kappa} \ell n (S_R/100) \quad \text{as} \quad S_R \to 0 \tag{4.168}$$

By experimental means, Nikuradse [see Schlichting (1979)] found that for flow over very rough surfaces,

$$B \to 8.5 + \frac{1}{\kappa} \ell n \left(1/k_R^+\right); \quad k_R^+ = u_\tau k_R/\nu \tag{4.169}$$

where $k_R$ is the average height of sand-grain roughness elements. (Note that the computations use $\kappa = 0.41$ while Nikuradse used $\kappa = 0.40$.) Thus, if we make the correlation

$$S_R = 100/k_R^+; \quad k_R^+ \gg 1 \tag{4.170}$$

then Equations (4.168) and (4.169) are nearly identical. Figure 4.13 compares computed velocity profiles with the analytical fit obtained by using Equations (4.168) and (4.169) in the law of the wall, viz.,

$$U^+ = \frac{1}{\kappa} \ell n \left(y/k_R\right) + 8.4 \tag{4.171}$$

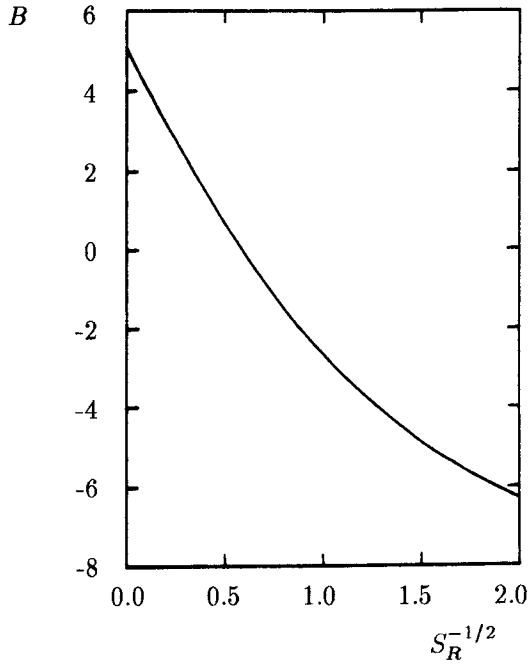


Figure 4.12: Variation of the constant in the law of the wall, $B$, with the surface value of the specific dissipation rate. [From Wilcox (1988a) — Copyright © AIAA 1988 — Used with permission.]

for three values of $k_R^+$. The correlation is nearly exact. The most remarkable fact about this correlation is that Equation (4.171) is the form the law of the wall assumes for flow over "completely-rough" surfaces, including the value of the additive constant (8.4 and 8.5 differ by one percent).

By making a qualitative argument based on flow over a wavy wall, Wilcox and Chambers (1975) [see Problems section] show that for small roughness heights, we should expect to have

$$S_R \sim (1/k_R^+)^2 \quad \text{as} \quad k_R^+ \to 0 \tag{4.172}$$

Comparison with Nikuradse's data shows that the following correlation between $S_R$ and $k_R^+$ reproduces measured effects of sand-grain roughness for values of $k_R^+$ up to about 400.

$$S_R = \begin{cases} (50/k_R^+)^2, & k_R^+ < 25 \\ \\ 100/k_R^+, & k_R^+ \geq 25 \end{cases} \tag{4.173}$$

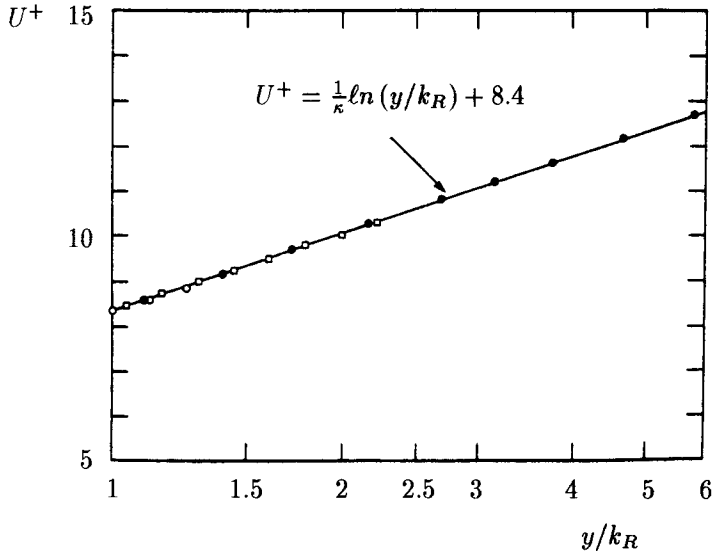


Figure 4.13: Sublayer velocity profiles for "completely rough" surfaces; o Computed, $k_R^+ = 400$; □ Computed, $k_R^+ = 225$; • Computed, $k_R^+ = 50$. [From Wilcox (1988a) — Copyright © AIAA 1988 — Used with permission.]

As a final comment, the solution for $k_R^+ \to 0$ is identical to the sublayer solution discussed in Subsection 4.6.3 [see Equation (4.158)]. The analysis of this section shows that the singular case corresponds to the perfectly-smooth surface. In practice, Equation (4.173) should be used rather than Equation (4.158) even if a perfectly-smooth surface is desired. The advantage in using Equation (4.173) is obvious for several reasons.

- Local geometry (e.g., distance normal to the surface) does not appear so it can be applied even in three-dimensional geometries.

- $k_R$ need only be small enough to have a hydraulically smooth surface, i.e., $u_\tau k_R/\nu < 5$. Resulting surface values of $\omega$ are rarely ever large enough to cause numerical error provided a sensible finite-difference grid is used (see Subsection 7.2.1).

- Experience has shown Equation (4.173) works well for separated flows.

### 4.7.3 Surface Mass Injection

For boundary layers with surface mass injection, the introduction of an additional velocity scale ($v_w$ = normal flow velocity at the surface) suggests that the scaling for $\omega$ at the surface may differ from Equation (4.167). Andersen, Kays and Moffat (1972) provide further evidence that the specific-dissipation-rate boundary condition must be revised when mass injection is present by showing, from correlation of their experimental data, that both $\kappa$ and $B$ are functions of $v_w^+ = v_w/u_\tau$. Because rough-surface computations show that the value of $B$ is strongly affected by the surface value of the specific dissipation rate, this suggests that the surface value of $\omega$ will depend in some manner upon $v_w$. Examination of the limiting form of the model equations for $y^+ \to \infty$ (i.e., in the log layer) shows immediately that the effective Kármán "constant", $\kappa_v$, varies with $v_w^+$ according to

$$\kappa_v = \frac{\kappa}{1 + \Xi v_w^+} \tag{4.174}$$

where $\Xi$ is given by

$$\Xi = 3.11 + 0.61 \ell n y^+ \tag{4.175}$$

The variation of $\kappa_v$ predicted in Equations (4.174) and (4.175) is consistent with the Andersen et al. data. Including appropriate convective terms in Equations (4.155), Wilcox (1988a) performed sublayer computations for the cases experimentally documented by Andersen et al. In each case, the surface value of $\omega$ is given by

$$\omega = \frac{u_\tau^2}{\nu} S_B \quad \text{at} \quad y = 0 \tag{4.176}$$

Wilcox varied the value of $S_B$ to achieve optimum agreement between measured and computed velocities. The correlation between $S_B$ and $v_w^+$ is given in analytical form as

$$S_B = \frac{20}{v_w^+(1 + 5v_w^+)} \tag{4.177}$$

Figure 4.14 compares measured velocities with values computed using Equations (4.176) and (4.177).

## 4.8 Application to Wall-Bounded Flows

Using the surface boundary conditions devised in Section 4.7, we can now turn to application of two-equation turbulence models to wall-bounded flows. Because of their relative simplicity, we consider pipe and channel

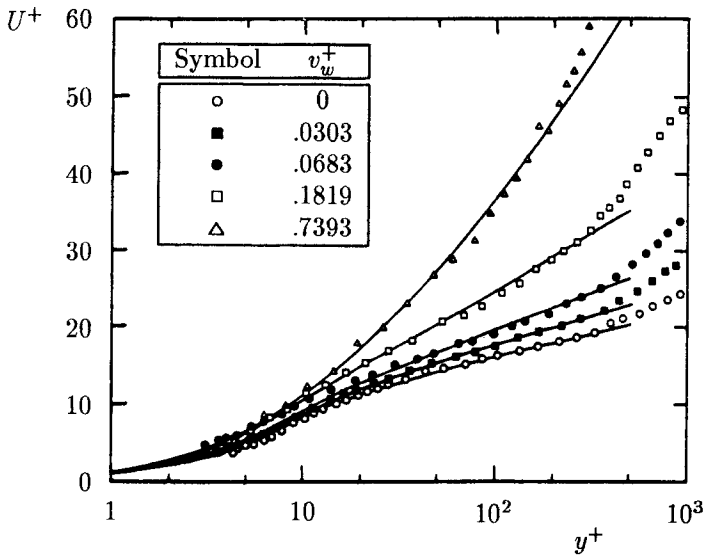


Figure 4.14: Sublayer velocity profiles for boundary layers with surface mass injection; —— $k$-$\omega$ model; ○ ■ ● □ △ Andersen, et al. [From Wilcox (1988a) — Copyright © AIAA 1988 — Used with permission.]

flow first using the $k$-$\omega$ model. Then, we will consider several incompressible boundary-layer applications. In these applications we exercise the $k$-$\omega$ model and the $k$-$\epsilon$ model.

### 4.8.1 Channel and Pipe Flow

Figures 4.15 and 4.16 compare computed and measured channel and pipe flow properties, respectively. Six different comparisons are shown in each figure, including mean velocity, skin friction, Reynolds shear stress, turbulence kinetic energy, turbulence energy production and dissipation rate.

Figure 4.15 compares $k$-$\omega$ model channel flow predictions with the Direct Numerical Simulation (DNS) computations performed by Mansour, Kim and Moin (1988). Reynolds number based on channel height and average velocity is 13,750. Velocity profiles and Reynolds shear stress profiles differ by less than 3%. Computed skin friction differs from Halleen and Johnston's (1967) correlation [Equation (3.137)] by less than about 2% except at the lowest Reynolds number shown. Although the model fails to predict the peak value of $k$ near the channel wall, the computed $k$ profile differs from the DNS profile by less than 5% over 80% of the channel. Despite

the fact that the model is not asymptotically consistent (Subsection 4.9.1) approaching the surface, even the turbulence-energy production, $\tau_{xy}\partial U/\partial y$, and dissipation, $\epsilon$, nearly duplicate the DNS results except very close to the surface. On balance, the $k$-$\omega$ results are a bit closer to the DNS results than either the Cebeci-Smith or Baldwin-Lomax models (Subsection 3.5.1).

Figure 4.16 compares $k$-$\omega$ model pipe flow results with Laufer's (1952) measurements at a Reynolds number based on pipe diameter and average velocity of 40,000. As shown, computed and measured velocity and Reynolds shear stress profiles differ by less than 6%. As with channel flow, computed and measured turbulence kinetic energy differ by about 4% except close to the surface where the sharp peak occurs. Although computed turbulence energy production and dissipation differ from measured values by less than 5%, it is unclear whether this is a desirable result. That is, some controversy exists about the accuracy of Laufer's dissipation measurements, and the model may be reproducing erroneous results. Finally, computed skin friction is within 4% of Prandtl's universal law of friction [Equation (3.138)]. Overall, predictions are as close to measurements as those obtained with the Cebeci-Smith and Baldwin-Lomax models.

It is interesting, and perhaps illuminating, that the most important flow properties are accurately predicted even though the sharp peak in turbulence energy is underestimated by 40% and 25%, respectively, for channel and pipe flow. That is, for engineering applications, the most important quantity is the skin friction. The next most important quantity typically is the velocity profile. Only for specialized applications is a subtle feature such as the peak value of $k$ important. Thus, we see that even though the $k$-$\omega$ model fails to predict this subtle feature, it is apparently of little consequence for most engineering applications.

### 4.8.2 Boundary Layers

We turn now to application of the $k$-$\omega$ and $k$-$\epsilon$ model equations to four incompressible boundary layers. All of the $k$-$\omega$ model results use the surface boundary conditions described in Subsections 4.7.2 and 4.7.3. By contrast, the $k$-$\epsilon$ model computations were done using wall functions.

The first application is for the constant-pressure incompressible boundary layer. The computation begins at a plate-length Reynolds number, $Re_x = 1 \cdot 10^6$ and continues to $Re_x = 10.9 \cdot 10^6$. Figures 4.17(a) and (b) compare computed and measured [Coles and Hirst (1969)] skin friction and velocity profiles. As shown, for the $k$-$\omega$ model, computed $c_f$ virtually duplicates measurements for the entire range of Reynolds numbers considered. Differences between computed and measured $k$-$\omega$ velocity profiles are no more than 3% of scale for the three Reynolds numbers indicated.

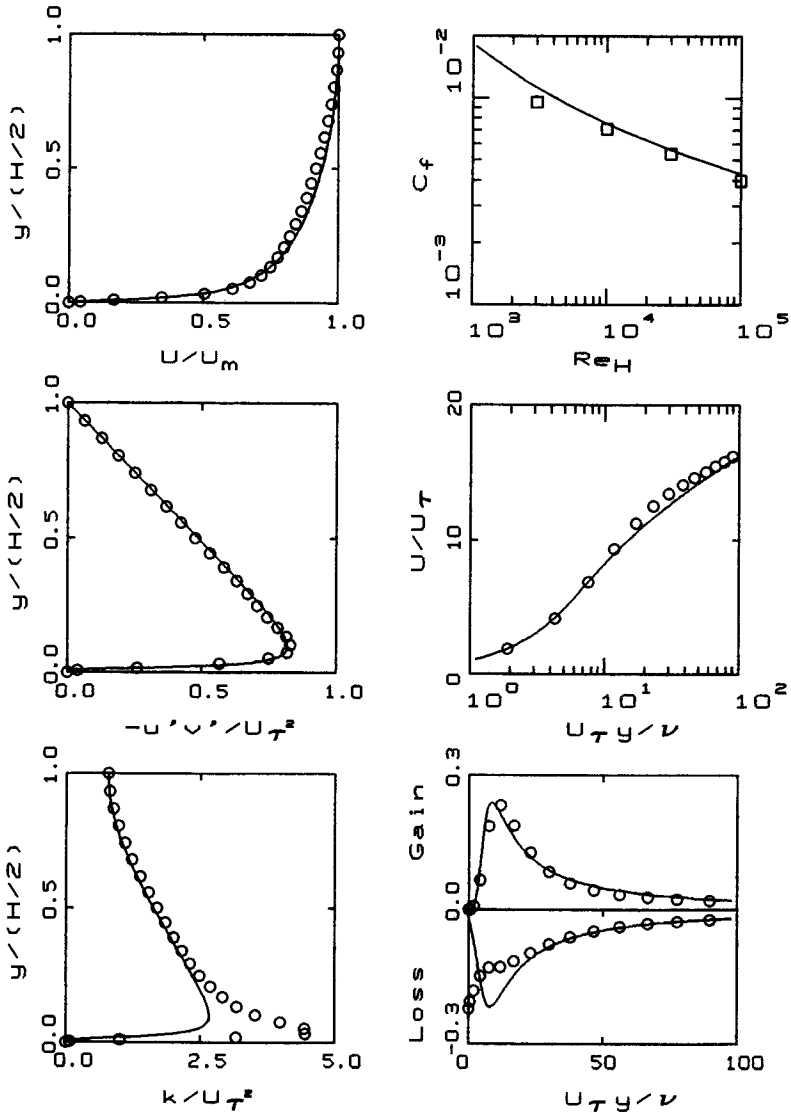


Figure 4.15: Comparison of computed and measured channel-flow properties, $Re_H = 13,750$. —— $k$-$\omega$ model; ○ Mansour et al. (DNS); □ Halleen-Johnston correlation.

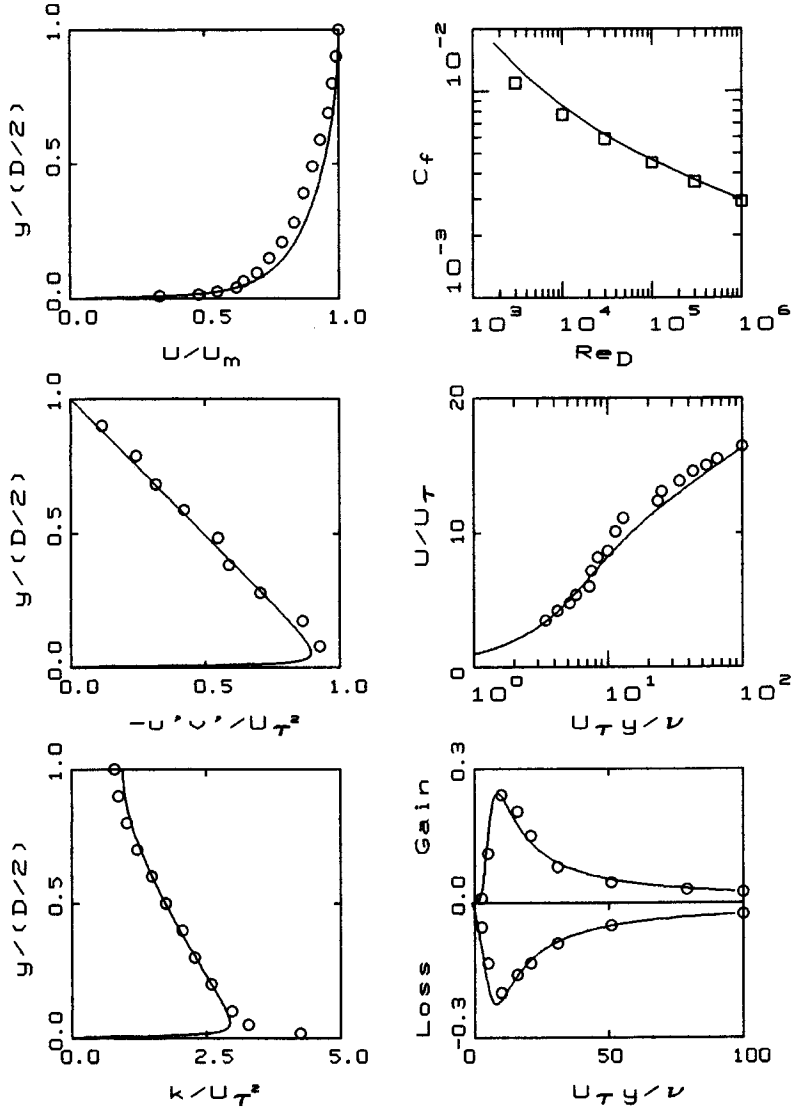


Figure 4.16: Comparison of computed and measured pipe-flow properties, $Re_D = 40,000$. —— $k$-$\omega$ model; ○ Laufer; □ Prandtl correlation.

Thus, as no great surprise, the $k$-$\omega$ model is quite accurate for the flat-plate boundary layer. Skin friction results [Chambers and Wilcox (1977)] for the $k$-$\epsilon$ model are included in Figure 4.17(a). Note that, as predicted in the defect-layer analysis of Subsection 4.6.2, computed $c_f$ is about 3% higher than measured.

The next two applications are for boundary layers with adverse pressure gradient. The first case is for moderate adverse pressure gradient, the experimental data being those of Bradshaw (1969). The second case has increasingly adverse pressure gradient, the experimental data being those of Samuel and Joubert [see Kline et al. (1981) - Flow 0141].

For the Bradshaw case, streamwise distance extends from $x = 2.5$ ft to $x = 7.0$ ft, corresponding to $Re_x$ increasing from about $2{\cdot}10^6$ to about $4{\cdot}10^6$. Figures 4.17(c) and (d) compare computed and measured skin friction and a velocity profile. Inspection of both graphs shows that differences between $k$-$\omega$ model predictions and experiment nowhere exceed 5% for this flow. The figure includes $k$-$\epsilon$ results obtained by Chambers and Wilcox (1977); computed $c_f$ exceeds measured values by as much as 20%. Because the equilibrium parameter $\beta_T \approx 2$ for this flow, the poor results for the $k$-$\epsilon$ model are unsurprising. Note also that the $k$-$\omega$ model's skin friction is much closer to measured values than either the Cebeci-Smith or Baldwin-Lomax models (see Figure 3.16).

In the Samuel-Joubert case, we integrate from $x = 1$ m to $x = 3.40$ m, corresponding to an $Re_x$ range of about $2{\cdot}10^6$ to $4{\cdot}10^6$. Figures 4.17(e) and (f) compare computed and measured skin friction and two velocity profiles for this flow. For the $k$-$\omega$ model, computed and measured skin friction differ by less than 5% of scale. Also, velocity profiles at $x = 2.87$ m are within 5% percent while those at $x = 3.40$ m differ by no more than 9%. The figure also shows skin friction for the $k$-$\epsilon$ model obtained by Rodi and Scheuerer (1986). Since $\beta_T$ exceeds 9 toward the end of the computation, the poor performance of the $k$-$\epsilon$ model (computed $c_f$ exceeds measured values by as much as 35%) is again consistent with the defect-layer analysis of Subsection 4.6.3.

As the final application of the models, we consider a boundary layer with surface mass injection. The case considered was included in the 1980-81 AFOSR-HTTM-Stanford Conference on Complex Turbulent Flows (Flow 0241) and data for the flow were taken by Andersen et al. (1972). Surface mass injection rate, $v_w$, is $.00375U_e$, where $U_e$ is the constant boundary-layer-edge velocity, i.e., the flow has constant pressure. Figures 4.17(g) and (h) compare computed and measured skin friction and velocity profiles. As shown, for the $k$-$\omega$ model computed and measured skin friction differ by less than 4% of scale while computed and measured velocity profiles are within 3% of each other. Although this flow has zero pressure gradient,

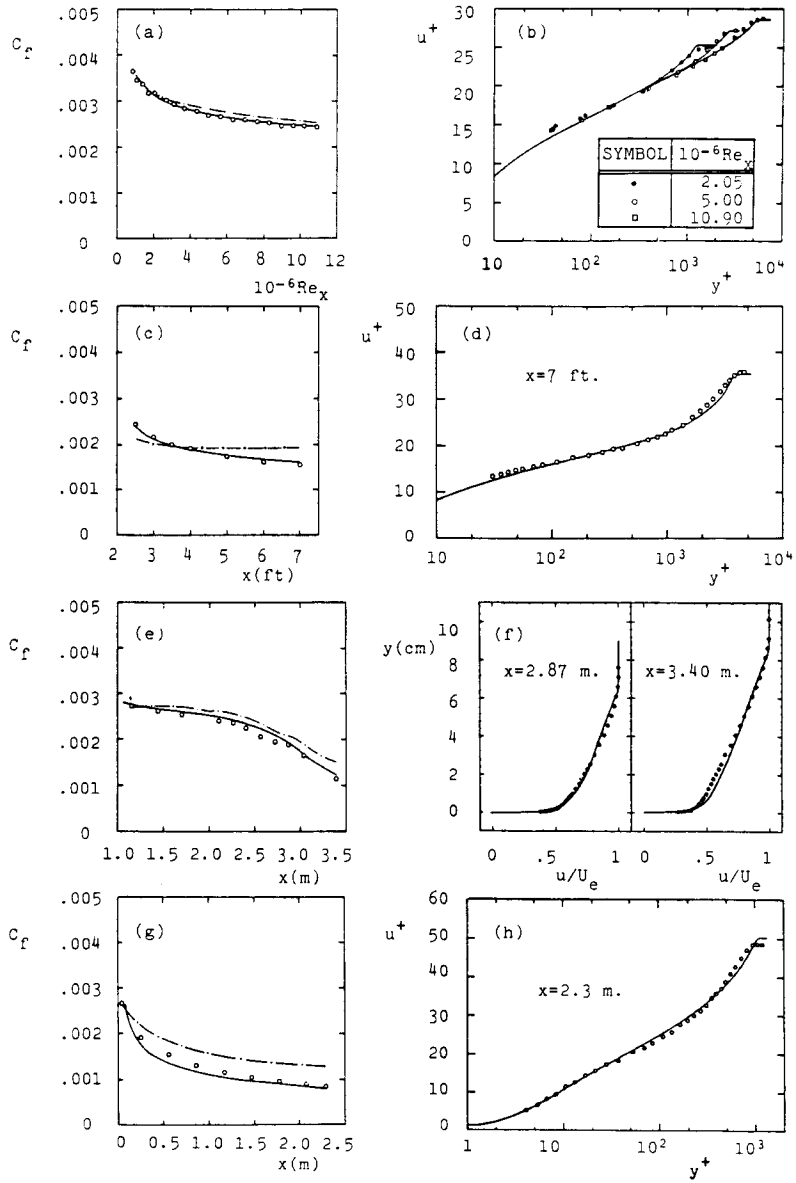


Figure 4.17: Computed and measured skin-friction and velocity profiles for incompressible boundary layers; —— $k$-$\omega$ model; – · – $k$-$\epsilon$ model; o • measured. [From Wilcox (1988a) — Copyright © AIAA 1988 — Used with permission.]

corresponding skin friction predicted by the $k$-$\epsilon$ model [see Kline et al. (1981)] is as much as 50% higher than measured.

## 4.9 Low-Reynolds-Number Effects

Thus far, the turbulence models we have considered are restricted to high-Reynolds number applications. Even in the case of the $k$-$\omega$ model, while we have been able to integrate through the viscous sublayer, we have paid no attention to low-Reynolds-number effects. For example, the model fails to predict the sharp peak in turbulence kinetic energy close to the surface for pipe and channel flow (see Figures 4.15 and 4.16). Most importantly, most two-equation models fail to predict a realistic value of the additive constant, $B$, in the law of the wall. All such models require viscous damping in order to achieve a realistic value for $B$. Finally, there are applications for which viscous effects must be accurately represented, and this section will discuss commonly used low-Reynolds-number corrections.

### 4.9.1 Asymptotic Consistency

In formulating viscous corrections for two-equation models, we can obtain some guidance from looking at the limiting behavior of the fluctuating velocities approaching a solid boundary. That is, we assume standard Taylor series expansions for each of the fluctuating velocities and substitute into the exact equations of motion, viz., the instantaneous continuity and Navier-Stokes equations. We did this in Subsection 4.6.3 when we were formulating surface boundary conditions for the viscous sublayer perturbation solution. Thus, we again begin by assuming

$$\left.\begin{aligned} u' &\sim A(x,z,t)y + O(y^2) \\ v' &\sim B(x,z,t)y^2 + O(y^3) \\ w' &\sim C(x,z,t)y + O(y^2) \end{aligned}\right\} \quad \text{as} \quad y \to 0 \tag{4.178}$$

where $A(x,z,t)$, $B(x,z,t)$ and $C(x,z,t)$ must have zero time average and satisfy the equations of motion. Note that the no-slip surface boundary condition dictates the fact that $\mathbf{u}'$ must go to zero as $y \to 0$. Since we expect Navier-Stokes solutions to be analytic everywhere, we conclude that the fluctuating velocity components $u'$ and $w'$ vary linearly with $y$. Also, substituting Equations (4.178) into the continuity equation shows that $v'$ varies quadratically with $y$. While we don't know the precise values of $A$, $B$ and $C$ without solving the complete Navier-Stokes equation, we can still use the exact asymptotic variations of $u'$, $v'$ and $w'$ with $y$ to deduce the

limiting behavior of time-averaged properties approaching the surface. For example, the turbulence kinetic energy and dissipation are

$$k \sim \frac{1}{2}(\overline{A^2 + C^2})y^2 + O(y^3) \quad \text{and} \quad \epsilon \sim \nu\,(\overline{A^2 + C^2}) + O(y) \tag{4.179}$$

Also, the Reynolds shear stress is given by

$$\tau_{xy} \sim -\overline{AB}y^3 + O(y^4) \tag{4.180}$$

A model that duplicates the exact limiting forms of $k$, $\epsilon$ and $\tau_{xy}$ given in Equations (4.179) and (4.180) is said to be **asymptotically consistent** with the near-wall behavior of the exact equations of motion.

Many researchers have attempted to devise viscous corrections for the $k$-$\epsilon$ model to permit its integration through the viscous sublayer. All have achieved some degree of **asymptotic consistency**. Jones and Launder (1972) were the first to propose viscous modifications for the $k$-$\epsilon$ model. Other proposals have been made by Launder and Sharma (1974), Hoffmann (1975), Reynolds (1976), Hassid and Poreh (1978), Lam and Bremhorst (1981), Dutoya and Michard (1981), Chien (1982), Myong and Kasagi (1990), Speziale, Abid and Anderson (1990), Shih and Hsu (1991), Zhang, So, Speziale and Lai (1992), Yang and Shih (1993), and Fan, Lakshminarayana and Barnett (1993). For steady, incompressible boundary layers, all of these models can be written compactly as follows:

$$U\frac{\partial k}{\partial x} + V\frac{\partial k}{\partial y} = \nu_T\left(\frac{\partial U}{\partial y}\right)^2 - \epsilon + \frac{\partial}{\partial y}\left[(\nu + \nu_T/\sigma_k)\frac{\partial k}{\partial y}\right] \tag{4.181}$$

$$U\frac{\partial \tilde{\epsilon}}{\partial x} + V\frac{\partial \tilde{\epsilon}}{\partial y} = C_{\epsilon 1}f_1\frac{\tilde{\epsilon}}{k}\nu_T\left(\frac{\partial U}{\partial y}\right)^2 - C_{\epsilon 2}f_2\frac{\tilde{\epsilon}^2}{k} + E + \frac{\partial}{\partial y}\left[(\nu + \nu_T/\sigma_\epsilon)\frac{\partial \tilde{\epsilon}}{\partial y}\right] \tag{4.182}$$

where the dissipation, $\epsilon$, is related to the quantity $\tilde{\epsilon}$ by

$$\epsilon = \epsilon_o + \tilde{\epsilon} \tag{4.183}$$

The quantity $\epsilon_o$ is the value of $\epsilon$ at $y = 0$, and is defined differently for each model. The eddy viscosity is defined as

$$\nu_T = C_\mu f_\mu k^2/\tilde{\epsilon} \tag{4.184}$$

Equations (4.181) - (4.184) contain five empirical **damping functions**, $f_1$, $f_2$, $f_\mu$, $\epsilon_o$ and $E$. These functions depend upon one or more of the following three dimensionless parameters.

$$Re_T = \frac{k^2}{\tilde{\epsilon}\nu}, \quad R_y = \frac{k^{1/2}y}{\nu}, \quad y^+ = \frac{u_\tau y}{\nu} \tag{4.185}$$

The models devised by Jones and Launder (1972), Launder and Sharma (1974), Lam and Bremhorst (1981), and Chien (1982) exemplify most of the features incorporated in $k$-$\epsilon$ model viscous damping functions. The damping functions and closure coefficients for these four models are as follows.

**Jones-Launder Model**

$$\left.\begin{aligned} f_\mu &= e^{-2.5/(1+Re_T/50)} \\ f_1 &= 1 \\ f_2 &= 1 - 0.3e^{-Re_T^2} \\ \epsilon_o &= 2\nu\left(\frac{\partial\sqrt{k}}{\partial y}\right)^2 \\ E &= 2\nu\nu_T\left(\frac{\partial^2 U}{\partial y^2}\right)^2 \\ C_{\epsilon 1} &= 1.45, \quad C_{\epsilon 2} = 2.00, \quad C_\mu = 0.09, \quad \sigma_k = 1.0, \quad \sigma_\epsilon = 1.3 \end{aligned}\right\} \quad (4.186)$$

**Launder-Sharma Model**

$$\left.\begin{aligned} f_\mu &= e^{-3.4/(1+Re_T/50)^2} \\ f_1 &= 1 \\ f_2 &= 1 - 0.3e^{-Re_T^2} \\ \epsilon_o &= 2\nu\left(\frac{\partial\sqrt{k}}{\partial y}\right)^2 \\ E &= 2\nu\nu_T\left(\frac{\partial^2 U}{\partial y^2}\right)^2 \\ C_{\epsilon 1} &= 1.44, \quad C_{\epsilon 2} = 1.92, \quad C_\mu = 0.09, \quad \sigma_k = 1.0, \quad \sigma_\epsilon = 1.3 \end{aligned}\right\} \quad (4.187)$$

**Lam-Bremhorst Model**

$$\left.\begin{aligned} f_\mu &= \left(1 - e^{-0.0165R_y}\right)^2 \left(1 + 20.5/Re_T\right) \\ f_1 &= 1 + (0.05/f_\mu)^3 \\ f_2 &= 1 - e^{-Re_T^2} \\ \epsilon_o &= 0 \\ E &= 0 \\ C_{\epsilon 1} &= 1.44, \quad C_{\epsilon 2} = 1.92, \quad C_\mu = 0.09, \quad \sigma_k = 1.0, \quad \sigma_\epsilon = 1.3 \end{aligned}\right\} \quad (4.188)$$

**Chien Model**

$$\left.\begin{aligned} f_\mu &= 1 - e^{-0.0115y^+} \\ f_1 &= 1 \\ f_2 &= 1 - 0.22e^{-(Re_T/6)^2} \\ \epsilon_o &= 2\nu\frac{k}{y^2} \\ E &= -2\nu\frac{\tilde{\epsilon}}{y^2}e^{-y^+/2} \\ C_{\epsilon 1} &= 1.35, \quad C_{\epsilon 2} = 1.80, \quad C_\mu = 0.09, \quad \sigma_k = 1.0, \quad \sigma_\epsilon = 1.3 \end{aligned}\right\} \quad (4.189)$$

By examining the limiting behavior of each of these models close to a solid boundary where $y = 0$, it is easy to demonstrate that, consistent with Equation (4.179), all four models guarantee

$$k \sim y^2 \quad \text{and} \quad \epsilon/k \to 2\nu/y^2 \quad \text{as} \quad y \to 0 \qquad (4.190)$$

Additionally, the Lam-Bremhorst model predicts $\tau_{xy} \sim y^4$ while the other three models predict $\tau_{xy} \sim y^3$. Thus, all except the Lam-Bremhorst model are consistent with Equation (4.180) as well.

Surface boundary conditions for low-Reynolds-number $k$-$\epsilon$ models are not entirely straightforward. On the one hand, the no-slip boundary condition tells us that $k$ must vanish at a solid boundary. On the other hand, the strongest thing we can say about the surface value of $\epsilon$ is the second of Equations (4.190). That is, we invariably must tie the surface value of $\epsilon$ to the second derivative of $k$ at the surface. The Jones-Launder, Launder-Sharma and Chien models build in the proper asymptotic behavior through introduction of the function $\epsilon_o$. Consequently, the boundary conditions appropriate at the surface are

$$k = \tilde{\epsilon} = 0 \quad \text{at} \quad y = 0 \qquad (4.191)$$

By contrast, Lam and Bremhorst deal directly with $\epsilon$ and specify the surface boundary condition on $\epsilon$ by requiring

$$\epsilon = \nu\frac{\partial^2 k}{\partial y^2} \quad \text{at} \quad y = 0 \qquad (4.192)$$

As an alternative, Lam and Bremhorst also propose using

$$\frac{\partial \epsilon}{\partial y} = 0 \quad \text{at} \quad y = 0 \qquad (4.193)$$

While Equation (4.193) is easier to implement than Equation (4.192), there is no a priori reason to expect that the next term in the Taylor series expansion for $\epsilon$ should vanish.

In a review article, Patel, Rodi and Scheuerer (1985) compare seven low-Reynolds-number variants of the $k$-$\epsilon$ model and the Wilcox-Rubesin (1980) $k$-$\omega^2$ model. Figure 4.18 compares computed and measured velocity and $k^+ = k/u_\tau^2$ profiles for the flat-plate boundary layer. As shown, the Dutoya-Michard, Hassid-Poreh and Hoffmann models fail to provide accurate solutions for the incompressible flat-plate boundary layer. Figure 4.19(a) shows that for adverse pressure gradient, the Wilcox-Rubesin model (which was not designed with low-Reynolds-number applications in mind) most faithfully matches measured [Anderson et al. (1972)] skin friction. Figure 4.19(b) shows that none of the models reproduces the measured skin friction for the low-Reynolds-number, favorable pressure gradient flow of Simpson and Wallace (1975). This further demonstrates that the only thing low-Reynolds-number modifications do is fix the $k$-$\epsilon$ model's problems in predicting the constant $B$ in the law of the wall.

There is a popular misconception that low-Reynolds-number modifications to the $k$-$\epsilon$ model can remove its deficiencies for adverse pressure gradient flows. This mistaken notion overlooks the volumes of data on and physical understanding of turbulent boundary layers established during the twentieth century, most notably by Clauser and Coles. Recall from Subsection 4.6.1 that Coles describes the turbulent boundary layer as a "wake-like structure constrained by a wall" and notes that different scales and physical processes are dominant in the sublayer and defect layer. Since perturbation analysis shows that the $k$-$\epsilon$ model is inconsistent with observed defect-layer structure, we cannot reasonably expect viscous corrections (which are negligible in the physical defect layer) to correct the inconsistency.

Figure 4.20 clearly illustrates this point. The figure compares computed and measured skin friction for twelve incompressible boundary layers with adverse pressure gradient. Results are presented for the Jones-Launder, Launder-Sharma, Lam-Bremhorst, Chien, and Wilcox (1988a) $k$-$\omega$ models. Eleven of the cases are from the 1968 AFOSR-IFP-Stanford Conference, and the flow numbers from the conference are included for each case. Flow 0141 is the Samuel-Joubert case from the 1980-81 AFOSR-HTTM-Stanford Conference on Complex Turbulent Flows.

As shown, for Bradshaw Flow C (Flow 3300) and the Samuel-Joubert case (Flow 0141), skin friction is similar to results obtained with wall functions [see Figure 4.17(e)]. As categorized by Coles and Hirst (1969), Flows 1100, 2100, 2500 and 4800 have "mild" adverse pressure gradient, Flows 2400, 2600, 3300 and 4500 have "moderate" adverse pressure gradient, and Flows 0141, 1200, 4400 and 5300 have "strong" adverse pressure gradient. Discrepancies between computed and measured $c_f$ increase dramatically for all four $k$-$\epsilon$ models as the strength of the pressure gradient increases. By contrast, $k$-$\omega$ results are remarkably close to measured values for all twelve

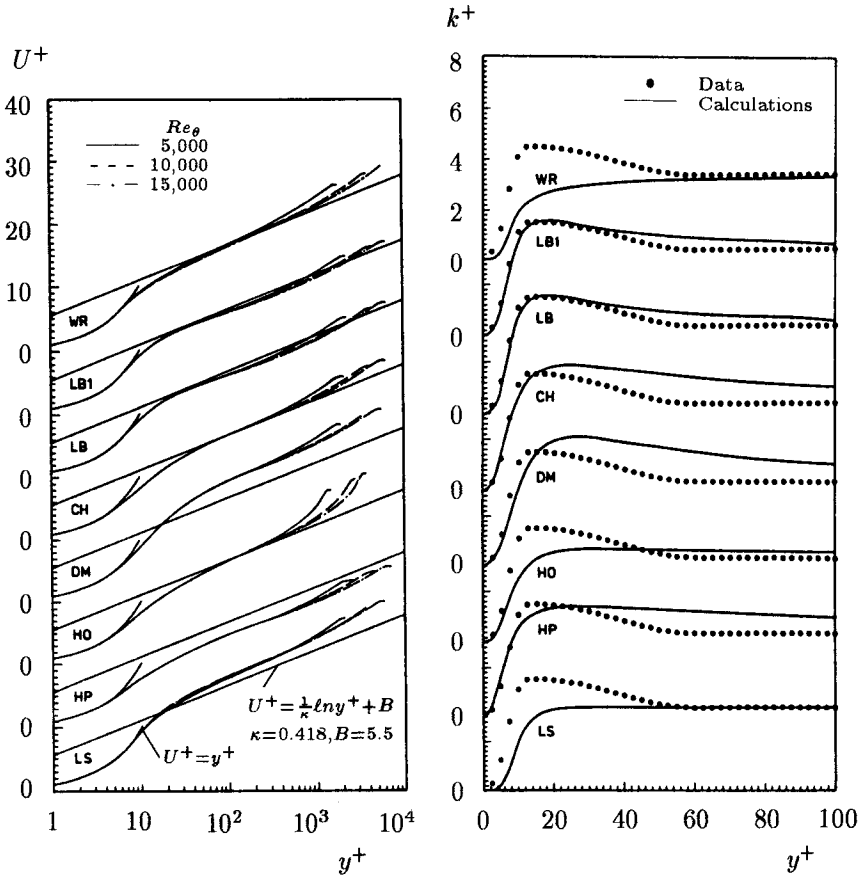


Figure 4.18: Flat-plate boundary layer properties. CH = Chien; DM = Dutoya-Michard; HO = Hoffman; HP = Hassid-Poreh; LB = Lam-Bremhorst with $\epsilon = \nu \partial^2 k / \partial y^2$; LB1 = Lam-Bremhorst with $\partial \epsilon / \partial y = 0$; LS = Launder-Sharma; WR = Wilcox-Rubesin. [From Patel, Rodi and Scheuerer (1985) — Copyright © AIAA 1985 — Used with permission.]

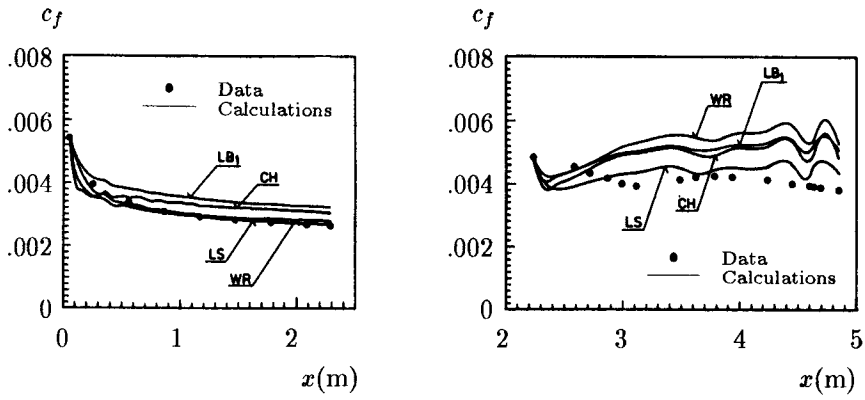


(a) Adverse Pressure Gradient (b) Favorable Pressure Gradient

Figure 4.19: Comparison of computed and measured skin friction for low-Reynolds-number flows with pressure gradient. CH = Chien; LB1 = Lam-Bremhorst with $\partial\epsilon/\partial y = 0$; LS = Launder-Sharma; WR = Wilcox-Rubesin. [From Patel, Rodi and Scheuerer (1985) — Copyright © AIAA 1985 — Used with permission.]

cases, including the nearly separated Flow 5300 (the Chien model predicts separation for this case). In terms of the final values of $c_f$, the average difference between computation and measurement is 7% for the $k$-$\omega$ model, 46% for the Launder-Sharma model, 46% for the Chien model, 58% for the Lam-Bremhorst model, and 74% for the Jones-Launder model.

These results confirm the defect-layer perturbation solution presented in Subsection 4.6.2, which shows that [see Equation (4.151)]:

$$\frac{U_e - U}{u_\tau} \sim -\frac{1}{\kappa}\ell n\eta + A - \beta_T C\eta\ell n\eta + O\left(\eta^2\ell n\eta\right) \quad \text{as} \quad \eta \to 0 \quad (4.194)$$

where the coefficient $C$ is given in Table 4.4. Combining Equation (4.194) with Equation (4.148), the effective law of the wall predicted by the $k$-$\epsilon$ model is

$$U^+ \sim \frac{1}{\kappa}\ell n y^+ + B + \beta_T C\eta\ell n\eta \quad \text{as} \quad y^+ \to \infty \quad (4.195)$$

Figure 4.21 compares the computed Launder-Sharma model near-wall velocity profile with experimental data, the standard law of the wall and Equation (4.195). Examination of the numerical solution shows that the implied constant in the law of the wall, $B$, is 5.5. As shown, the asymptotic

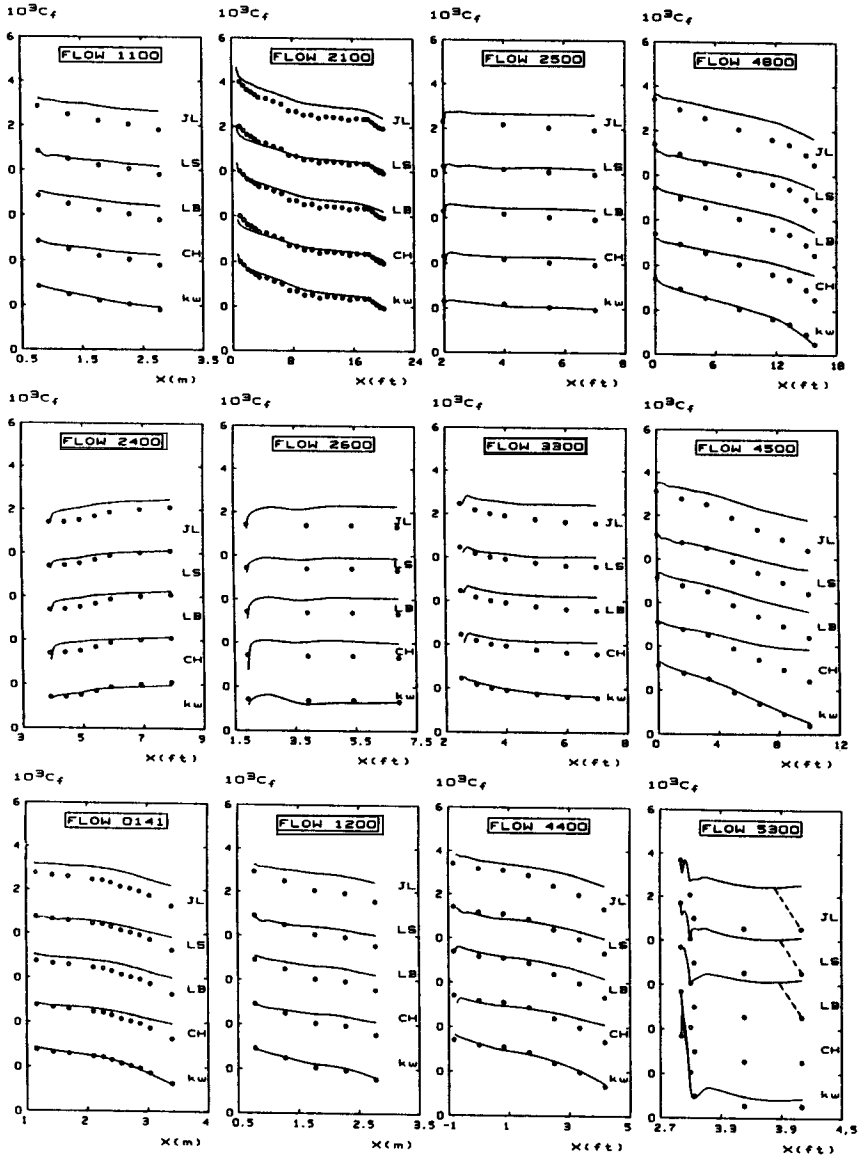


Figure 4.20: Computed and measured skin friction for boundary layers with adverse pressure gradient; CH = Chien; JL = Jones-Launder; LB = Lam-Bremhorst; LS = Launder-Sharma; kw = $k$-$\omega$.

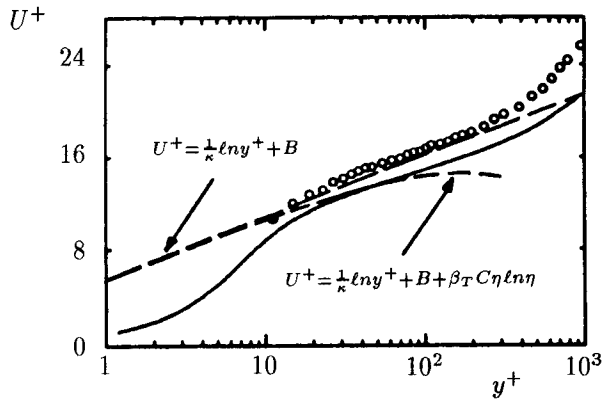


Figure 4.21: Computed and measured near-wall velocity profiles for Samuel and Joubert's adverse pressure gradient flow, $x = 3.40$ m.; —— Launder-Sharma model with $\kappa = .43$ and $B = 5.5$; o Samuel-Joubert.

formula provides an excellent approximation to the numerical results in the region between $y^+ = 20$ and 100. If we included the $O(\eta^2 \ell n\eta)$ term or used the exact defect-layer solution, the match would extend even farther above the sublayer. The important point to note is the impact of the term in Equation (4.195) proportional to the equilibrium parameter, $\beta_T$. Its effect is to distort the velocity profile throughout the defect layer, including its asymptotic form approaching the sublayer from above.

As a final comment on low-Reynolds-number corrections for the $k$-$\epsilon$ model, using the dimensionless parameters $R_y$ and $y^+$ [Equation (4.185)] is ill advised. Both depend upon distance normal to the surface, which can cause difficulty in complex geometries such as a wing-fuselage junction. Also, it is ironic that several additional closure coefficients and functions are needed for the $k$-$\epsilon$ model to behave properly in the near-wall region of a turbulent boundary layer. Dissipation is, after all, a phenomenon that occurs in the smallest eddies, and that is all we find in the near-wall region. This further underscores the fact that there is virtually no connection between the exact equation for $\epsilon$ and its modeled counterpart.

### 4.9.2 Transition

Turbulence model equations can be used to predict transition from laminar to turbulent flow, although most models predict transition to turbulence at Reynolds numbers that are at least an order of magnitude too low. To understand why and how the $k$-$\omega$ model predicts transition, consider the

flat-plate boundary layer. For the $k$-$\omega$ model, the incompressible, two-dimensional boundary-layer form of the equations for $k$ and $\omega$ is as follows.

$$\rho U\frac{\partial U}{\partial x}+\rho V\frac{\partial U}{\partial y}=\frac{\partial}{\partial y}\left[(\nu+\nu_T)\frac{\partial U}{\partial y}\right] \tag{4.196}$$

$$U\frac{\partial k}{\partial x}+V\frac{\partial k}{\partial y}=\nu_T\left(\frac{\partial U}{\partial y}\right)^2-\beta^*\omega k+\frac{\partial}{\partial y}\left[(\nu+\sigma^*\nu_T)\frac{\partial k}{\partial y}\right] \tag{4.197}$$

$$U\frac{\partial \omega}{\partial x}+V\frac{\partial \omega}{\partial y}=\alpha\frac{\omega}{k}\nu_T\left(\frac{\partial U}{\partial y}\right)^2-\beta\omega^2+\frac{\partial}{\partial y}\left[(\nu+\sigma\mu_T)\frac{\partial \omega}{\partial y}\right] \tag{4.198}$$

$$\nu_T=\alpha^* k/\omega \tag{4.199}$$

With one exception, all notation and closure coefficients are as defined in Equations (4.33) to (4.37). The only difference is the appearance of an additional closure coefficient $\alpha^*$ in Equation (4.199). This coefficient is equal to one for the standard high-Reynolds-number version of the $k$-$\omega$ model. We can most clearly illustrate how the model equations predict transition by rearranging terms in Equations (4.197) and (4.198) as follows.

$$U\frac{\partial k}{\partial x}+V\frac{\partial k}{\partial y}=P_k\beta^*\omega k+\frac{\partial}{\partial y}\left[(\nu+\sigma^*\nu_T)\frac{\partial k}{\partial y}\right] \tag{4.200}$$

$$U\frac{\partial \omega}{\partial x}+V\frac{\partial \omega}{\partial y}=P_\omega\beta\omega^2+\frac{\partial}{\partial y}\left[(\nu+\sigma\mu_T)\frac{\partial \omega}{\partial y}\right] \tag{4.201}$$

The **net production per unit dissipation** for the two equations, $P_k$ and $P_\omega$, are defined by:

$$P_k=\frac{\alpha^*}{\beta^*}\left(\frac{\partial U/\partial y}{\omega}\right)^2-1 \tag{4.202}$$

$$P_\omega=\frac{\alpha\alpha^*}{\beta}\left(\frac{\partial U/\partial y}{\omega}\right)^2-1 \tag{4.203}$$

There are two important observations worthy of mention at this point. **First**, if the turbulence energy is zero, Equation (4.201) has a well-behaved solution. That is, when $k=0$, the eddy viscosity vanishes and the $\omega$ equation uncouples from the $k$ equation. Consequently, the $k$-$\omega$ model has a nontrivial laminar-flow solution for $\omega$. **Second**, the signs of $P_k$ and $P_\omega$ determine whether $k$ and $\omega$ are amplified or reduced in magnitude. However, it is not obvious by inspection of Equations (4.202) and (4.203)

how the signs of these terms vary with Reynolds number as we move from the plate leading edge to points downstream. We can make the variation obvious by rewriting Equations (4.202) and (4.203) in terms of the Blasius transformation.

Before we introduce the Blasius transformation, we must determine the appropriate scaling for $\omega$. To do this, we note that close to the surface of a flat-plate boundary layer, the specific dissipation rate behaves according to [see Equation (4.158) and Table 4.5]:

$$\omega \to \frac{6\nu}{\beta y^2} \quad \text{as} \quad y \to 0 \tag{4.204}$$

In terms of the Blasius similarity variable, $\eta$, defined by

$$\eta = \frac{y}{\sqrt{\nu x / U_\infty}} \tag{4.205}$$

where $U_\infty$ is freestream velocity, the asymptotic behavior of $\omega$ approaching the surface is

$$\omega \to \frac{U_\infty}{x}\frac{6}{\beta\eta^2} \quad \text{as} \quad \eta \to 0 \tag{4.206}$$

Consequently, we conclude that the appropriate scaling for $\omega$ in the Blasius boundary layer is given by

$$\omega = \frac{U_\infty}{x} W(x, \eta) \tag{4.207}$$

where $W(x, \eta)$ is a dimensionless function to be determined as part of the solution. Hence, if we write the velocity in terms of dimensionless velocity, $\mathcal{U}(x, \eta)$, i.e.,

$$u = U_\infty \mathcal{U}(x, \eta) \tag{4.208}$$

the **net production per unit dissipation** terms become

$$P_k = \frac{\alpha^*}{\beta^*} Re_x \left( \frac{\partial \mathcal{U}/\partial\eta}{W} \right)^2 - 1 \tag{4.209}$$

$$P_\omega = \frac{\alpha\alpha^*}{\beta} Re_x \left( \frac{\partial \mathcal{U}/\partial\eta}{W} \right)^2 - 1 \tag{4.210}$$

Thus, both $P_k$ and $P_\omega$ increase linearly with Reynolds number, $Re_x$. From the exact laminar solution for $\mathcal{U}(\eta)$ and $W(\eta)$ [the $x$ dependence vanishes for the Blasius boundary layer], the maximum value of the ratio of $\partial\mathcal{U}/\partial\eta$ to $W$ is given by

$$\left( \frac{\partial \mathcal{U}/\partial\eta}{W} \right)_{max} \approx \frac{1}{300} \tag{4.211}$$

The precise value of this ratio is actually a weak function of the freestream value of $\omega$, ranging between 0.0025 and 0.0040. The maximum occurs about midway through the boundary layer ($y/\delta = 0.56$), a point above which the exact near-wall behavior of $\omega$ [Equation (4.206)] does not hold. Hence, a complete boundary-layer solution is needed to determine the maximum ratio of $\partial U/\partial\eta$ to $W$.

As long as the eddy viscosity remains small compared to the molecular viscosity, we can specify the precise points where $P_k$ and $P_\omega$ change sign. Using Equation (4.211), we conclude that the sign changes occur at the following Reynolds numbers.

$$(Re_x)_k = 9 \cdot 10^4 \frac{\beta^*}{\alpha^*} \tag{4.212}$$

$$(Re_x)_\omega = 9 \cdot 10^4 \frac{\beta}{\alpha\alpha^*} \tag{4.213}$$

With no viscous modifications, the closure coefficients $\alpha$, $\alpha^*$, $\beta$ and $\beta^*$ are 5/9, 1, 3/40 and 9/100, respectively. Using these **fully turbulent** values, we find $(Re_x)_k = 8,100$ and $(Re_x)_\omega = 12,150$. Thus, starting from laminar flow at the leading edge of a flat plate (see Figure 4.22), the following sequence of events occurs.

1. The computation starts in a laminar region with $k = 0$ in the boundary layer and a small freestream value of $k$.

2. Initially, because $P_k < 0$ and $P_\omega < 0$, dissipation of both $k$ and $\omega$ exceeds production. Turbulence energy is entrained from the freestream and spreads through the boundary layer by molecular diffusion. Neither $k$ nor $\omega$ is amplified and the boundary layer remains laminar.

3. At the **critical Reynolds number**, $Re_{x_c} = 8,100$, production overtakes dissipation in the $k$ equation. Downstream of $x_c$, production exceeds dissipation in the $k$ equation and turbulence energy is amplified. At some point in this process, the eddy viscosity grows rapidly and this corresponds to the transition point.

4. $k$ continues to be amplified and, beyond $Re_x = 12,150$ production overtakes dissipation in the $\omega$ equation. $\omega$ is now amplified and continues growing until a balance between production and dissipation is achieved in the $k$ equation. When this balance is achieved, transition from laminar to turbulent flow is complete.

Consistent with experimental measurements, the entire process is very sensitive to the freestream value of $k$. There is also a sensitivity to the freestream value of $\omega$, although the sensitivity is more difficult to quantify.

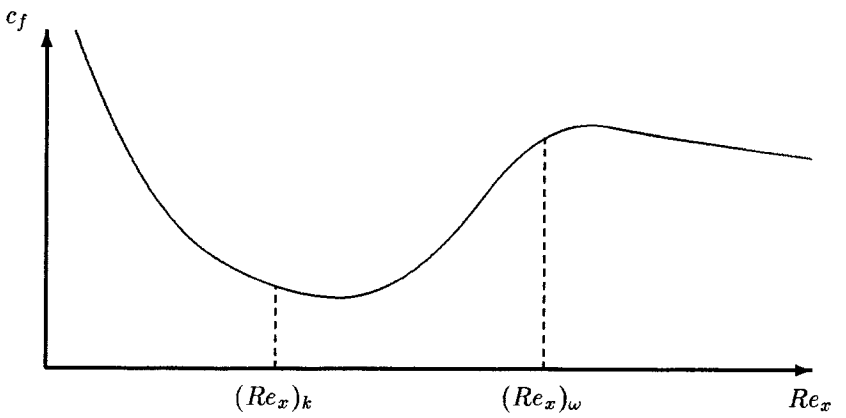


Figure 4.22: Skin friction variation for a boundary layer undergoing transition from laminar to turbulent flow.

Three key points are immediately obvious. **First**, $k$ begins growing at a Reynolds number of 8,100. By contrast, linear-stability theory tells us that Tollmien-Schlichting waves begin forming in the Blasius boundary layer at a Reynolds number of 90,000. This is known as the **minimum critical Reynolds number**. Correspondingly, we find that the model predicts transition at much too low a Reynolds number. **Second**, inspection of Equations (4.212) and (4.213) shows that the width of the transition region is controlled by the ratio of $\beta$ to $\alpha\alpha^*$. **Third**, transition will never occur if $P_\omega$ reaches zero earlier than $P_k$. Thus, occurrence of transition requires

$$\alpha\alpha^* < \alpha^*\beta/\beta^* \quad \text{as} \quad Re_T \to 0 \tag{4.214}$$

This fact must be preserved in any viscous modification to the model. Our goal is to devise viscous modifications that depend only upon $Re_T$. As noted in the preceding subsection, this quantity is independent of flow geometry and thus preserves the universal nature of the model. We also proceed with two key objectives in mind. The most important objective is to match the **minimum critical Reynolds number**. Reference to Equation (4.212) shows that we must require

$$\beta^*/\alpha^* \to 1 \quad \text{as} \quad Re_T \to 0 \tag{4.215}$$

Our secondary objective is to achieve **asymptotic consistency** with the exact behavior of $k$ and dissipation, $\epsilon = \beta^* k\omega$, approaching a solid boundary. That is, we would like to have $k/y^2 \to$ constant and $\epsilon/k \to 2\nu/y^2$

as $y \to 0$. Close to a solid boundary, the dissipation and molecular diffusion terms balance in both the $k$ and $\omega$ equations. The very-near-wall solution for $\omega$ is given by Equation (4.204). The solution for $k$ is of the form

$$k/y^n \to \text{constant} \quad \text{as} \quad y \to 0 \tag{4.216}$$

where n is given by

$$n = \frac{1}{2}\left[1 + \sqrt{1 + 24\frac{\beta^*}{\beta}}\right] \tag{4.217}$$

Noting that dissipation is related to $k$ and $\omega$ by

$$\epsilon = \beta^* k\omega \tag{4.218}$$

we can achieve the desired asymptotic behavior of $k$ provided

$$\beta^*/\beta \to 1/3 \quad \text{as} \quad Re_T \to 0 \tag{4.219}$$

Requiring this limiting behavior as $Re_T \to 0$ is sufficient to achieve the desired asymptotic behavior as $y \to 0$ since the eddy viscosity, and hence, $Re_T$ vanishes at a solid boundary.

If we choose to have $\beta$ constant for all values of $Re_T$, Equations (4.214), (4.215) and (4.219) are sufficient to determine the limiting values of $\alpha^*$ and $\beta^*$ and an upper bound for $\alpha\alpha^*$ as turbulence Reynolds number becomes vanishingly small. Specifically, we find

$$\left.\begin{array}{lcl} \alpha\alpha^* & < & \beta \\ \alpha^* & \to & \beta/3 \\ \beta^* & \to & \beta/3 \end{array}\right\} \quad \text{as} \quad Re_T \to 0 \tag{4.220}$$

Wilcox and Rubesin (1980) make the equivalent of $\alpha\alpha^*$ and $\alpha^*$ in their $k$-$\omega^2$ model approach the same limiting value and obtain excellent agreement with measured transition width for incompressible boundary layers. Numerical experimentation with the $k$-$\omega$ model indicates the optimum choice for incompressible boundary layers is $\alpha\alpha^* \to 0.74\beta$, or

$$\alpha\alpha^* \to 1/18 \quad \text{as} \quad Re_T \to 0 \tag{4.221}$$

Wilcox (1992a) postulates the following functional dependencies upon $Re_T$ that guarantee the limiting values in Equations (4.220) and (4.221), as well as the original fully turbulent values for $Re_T \to \infty$.

$$\alpha^* = \frac{\alpha_o^* + Re_T/R_k}{1 + Re_T/R_k} \tag{4.222}$$

$$\alpha = \frac{5}{9} \cdot \frac{\alpha_o + Re_T/R_\omega}{1 + Re_T/R_\omega} \cdot (\alpha^*)^{-1} \tag{4.223}$$

$$\beta^* = \frac{9}{100} \cdot \frac{5/18 + (Re_T/R_\beta)^4}{1 + (Re_T/R_\beta)^4} \tag{4.224}$$

$$\beta = 3/40, \quad \sigma^* = \sigma = 1/2, \quad \alpha_o^* = \beta/3, \quad \alpha_o = 1/10 \tag{4.225}$$

$$R_\beta = 8, \quad R_k = 6, \quad R_\omega = 27/10 \tag{4.226}$$

The quantity $Re_T$ is turbulence Reynolds number defined by

$$Re_T = \frac{k}{\omega\nu} \tag{4.227}$$

The three coefficients $R_\beta$, $R_k$ and $R_\omega$ control the rate at which the closure coefficients approach their fully-turbulent values. We can determine their values by using perturbation methods to analyze the viscous sublayer. Using the procedure discussed in Subsection 4.6.3, we can solve for the constant in the law of the wall, $B$. For given values of $R_\beta$ and $R_k$, there is a unique value of $R_\omega$ that yields a constant in the law of the wall of 5.0. For small values of $R_\beta$ the peak value of $k$ near the surface is close to the value achieved without viscous corrections, viz., $u_\tau^2/\sqrt{\beta^*}$. As $R_\beta$ increases, the maximum value of $k$ near the surface increases. Comparison of computed sublayer structure with Direct Numerical Simulation (DNS) results of Mansour, Kim and Moin (1988) indicates the optimum choice for these three coefficients is as indicated in Equation (4.226).

The only flaw in the model's asymptotic consistency occurs in the Reynolds shear stress, $\tau_{xy}$. While the exact asymptotic behavior is $\tau_{xy} \sim y^3$, the model as formulated predicts $\tau_{xy} \sim y^4$. This discrepancy could easily be removed with another viscous modification. However, as will be shown later in this subsection, this is of no significant consequence. It has no obvious bearing on either the model's ability to predict transition or properties of interest in turbulent boundary layers. The additional complexity and uncertainty involved in achieving this subtle feature of the very-near-wall behavior of $\tau_{xy}$ does not appear to be justified.

Given the information developed above, it is a simple matter to explain why little progress has been made in predicting transition with the $k$-$\epsilon$ model. The primary difficulties can be easily demonstrated by focusing upon incompressible boundary layers. If we use the standard form of the $k$-$\epsilon$ model, Equations (4.197) - (4.199) are replaced by

$$U\frac{\partial k}{\partial x}+V\frac{\partial k}{\partial y}=\nu_T\left(\frac{\partial U}{\partial y}\right)^2-\epsilon+\frac{\partial}{\partial y}\left[(\nu+\nu_T/\sigma_k)\frac{\partial k}{\partial y}\right] \tag{4.228}$$

$$U\frac{\partial \epsilon}{\partial x}+V\frac{\partial \epsilon}{\partial y}=C_{\epsilon 1}\frac{\epsilon}{k}\nu_T\left(\frac{\partial U}{\partial y}\right)^2-C_{\epsilon 2}\frac{\epsilon^2}{k}+\frac{\partial}{\partial y}\left[(\nu+\mu_T/\sigma_\epsilon)\frac{\partial \epsilon}{\partial y}\right] \tag{4.229}$$

$$\nu_T=C_\mu k^2/\epsilon \tag{4.230}$$

One critical difference from the $k$-$\omega$ model is obvious by inspection of Equations (4.228) - (4.230). Specifically, if the turbulence energy is zero, $\epsilon$ must also be zero. We cannot simply drop the eddy viscosity in the $\epsilon$ equation because of the presence of $k$ in the denominator of the $\epsilon$ equation's dissipation term. The model does possess a laminar-flow solution for the ratio of $\epsilon$ to $k$. That is, if we make the formal change of variables

$$\epsilon=C_\mu k\omega \tag{4.231}$$

and assume $\nu_T \ll \nu$, the following laminar-flow equation for $\omega$ results.

$$U\frac{\partial \omega}{\partial x}+V\frac{\partial \omega}{\partial y}=(C_{\epsilon 1}-1)f_\mu\left(\frac{\partial U}{\partial y}\right)^2-(C_{\epsilon 2}-1)C_\mu\omega^2+\nu\frac{\partial^2\omega}{\partial y^2}+\frac{2\nu}{k}\frac{\partial k}{\partial y}\frac{\partial \omega}{\partial y} \tag{4.232}$$

Equation (4.232) is nearly identical to the limiting form of Equation (4.198) for $\nu_T/\nu \to 0$. The only significant difference is the last term on the right-hand side of Equation (4.232). Except close to the surface where $k$ must be exactly zero, this term is unlikely to have a significant effect on the solution for small nonzero values of $k$. However, in a numerical solution, products of dependent-variable gradients are generally destabilizing, and the problem can only be aggravated by having a coefficient inversely proportional to $k$. This is not an insurmountable problem. However, establishing starting conditions is clearly more difficult with the $k$-$\epsilon$ model than with the $k$-$\omega$ model.

Given the diverse nature of viscous modifications that have been proposed for the $k$-$\epsilon$ model, it is impossible to make any universal statements about why a specific model fails to predict realistic transition Reynolds numbers. Perhaps the strongest statement that can be made is, **no one has approached the problem from the transition point of view**. Most researchers have sought only to achieve asymptotic consistency (Subsection 4.9.1) and attempted transition predictions only as an afterthought.

We can gain some insight by examining the net production per unit dissipation terms for the $k$ and $\epsilon$ equations that are analogous to Equations (4.209) and (4.210), viz.,

$$P_k = \frac{f_\mu}{C_\mu} Re_x \left( \frac{\partial U/\partial \eta}{W} \right)^2 - 1 \tag{4.233}$$

$$P_\epsilon = \frac{C_{\epsilon 1} f_\mu}{C_{\epsilon 2} C_\mu} Re_x \left( \frac{\partial U/\partial \eta}{W} \right)^2 - 1 \tag{4.234}$$

**On the one hand**, without viscous damping, if we assume Equation (4.211) is valid, we find $(Re_x)_k = 8,100$ and $(Re_x)_\epsilon = 10,800$. Consequently, as with the high-Reynolds-number version of the $k$-$\omega$ model, transition will occur at too low a Reynolds number. **On the other hand**, because $C_\mu$, $C_{\epsilon 2}$ and sometimes $C_{\epsilon 1}$ are multiplied by functions of distance from the surface and/or functions of $Re_T$ (c.f. $f_\mu$, $f_1$ and $f_2$ in Subsection 4.9.1) in low-Reynolds-number $k$-$\epsilon$ models, we cannot simply use Equation (4.211). Furthermore, as discussed in the preceding subsection, some modelers add terms to the $k$ and $\epsilon$ equations in addition to damping the closure coefficients. Each set of values for the closure coefficients and additional terms must be used in solving Equation (4.232) to determine the laminar-flow solution for $\epsilon/k$. While it is clearly impossible to make a quantitative evaluation of all variants of the $k$-$\epsilon$ model, we can nevertheless make some general observations.

From the analysis of the $k$-$\omega$ model, it is obvious that having $f_\mu < 1$ will tend to delay transition. Virtually all modelers implement an $f_\mu$ that will accomplish this end. However, the modifications of Jones and Launder (1972), Chien (1982), and Lam and Bremhorst (1981), for example, damp $C_{\epsilon 2}$ to the extent that $(Re_x)_\epsilon$ is smaller than $(Re_x)_k$. This is the opposite of what is needed and will have an undesirable effect on both the onset of and the extent of the transition region.

This discussion is not intended as an exhaustive survey of the numerous low-Reynolds-number versions of the $k$-$\epsilon$ model. Rather, it is intended to illustrate how difficult it is to apply the model to the transition problem. Given enough additional closure coefficients and damping functions, the $k$-$\epsilon$ model can probably be modified to permit satisfactory transition predictions. However, even if this is done, establishing starting conditions will ultimately require a solution to Equation (4.232). That is, to initialize the computation, we must effectively transform to the $k$-$\omega$ model. Since this is the natural starting point, it seems illogical to perform subsequent computations in terms of $k$ and $\epsilon$.

Figure 4.23 compares computed channel-flow skin friction, $c_f$, with the Halleen and Johnston (1967) correlation [see Equation (3.137)] for Reynolds

number based on channel height, $H$, and average velocity ranging from $10^3$ to $10^5$ using the $k$-$\omega$ model. As shown, computed $c_f$ differs from the correlation by less than 3% except at the lowest Reynolds number shown where the correlation probably is inaccurate. Velocity, Reynolds shear stress, and turbulence kinetic energy profiles differ by less than 7%. Most notably, the model predicts the peak value of $k$ near the channel wall to within 4% of the DNS value. The low-Reynolds-number modifications have been designed to capture this feature. Additionally, approaching the surface, the turbulence-energy production, $\tau_{xy}\partial U/\partial y$, and dissipation, $\epsilon$, are within 10% of the DNS results except very close to the surface.

Figure 4.24 compares computed pipe flow $c_f$ with Prandtl's universal law of friction [see Equation (3.138)]. Reynolds number based on pipe diameter, $D$, and average velocity varies from $10^3$ to $10^6$. As with channel flow, computed $c_f$ falls within 5% of the correlation except at the lowest Reynolds number shown where the correlation is likely to be in error.

Computed and measured velocity and Reynolds shear stress profiles differ by less than 8%. As with channel flow, computed and measured turbulence kinetic energy differ by about 5% including close to the surface where the sharp peak occurs. Note that, at this high a Reynolds number, the $k$ profile has a sharp spike near $y = 0$ and this feature is captured in the computations. Except very close to the surface, computed turbulence energy production and dissipation differ from measured values by less than 10%. This may actually be a desirable result. That is, some controversy exists about the accuracy of Laufer's dissipation measurements close to the surface.

Turning now to transition, Figure 4.25 compares computed and measured transition Reynolds number, $Re_{\theta_t}$, for an incompressible flat-plate boundary layer. We define the transition Reynolds number as the point where the skin friction achieves its minimum value. Results are displayed as a function of freestream turbulence intensity, $T'$, defined by

$$T' = 100\sqrt{\frac{2}{3}\frac{k_e}{U_e^2}} \tag{4.235}$$

where subscript $e$ denotes the value at the boundary-layer edge. As shown, consistent with the data compiled by Dryden (1959), $Re_{\theta_t}$ increases as the freestream intensity decreases. Because $\omega$ can be thought of as an averaged frequency of the freestream turbulence, it is reasonable to expect the predictions to be sensitive to the freestream value of $\omega$. To assess the effect, the freestream value of the turbulence length scale $\ell = k^{1/2}/\omega$ has been varied from $.001\delta$ to $.100\delta$ where $\delta$ is boundary-layer thickness. As shown, computed $Re_{\theta_t}$ values bracket virtually all of the data. Unlike the situation for

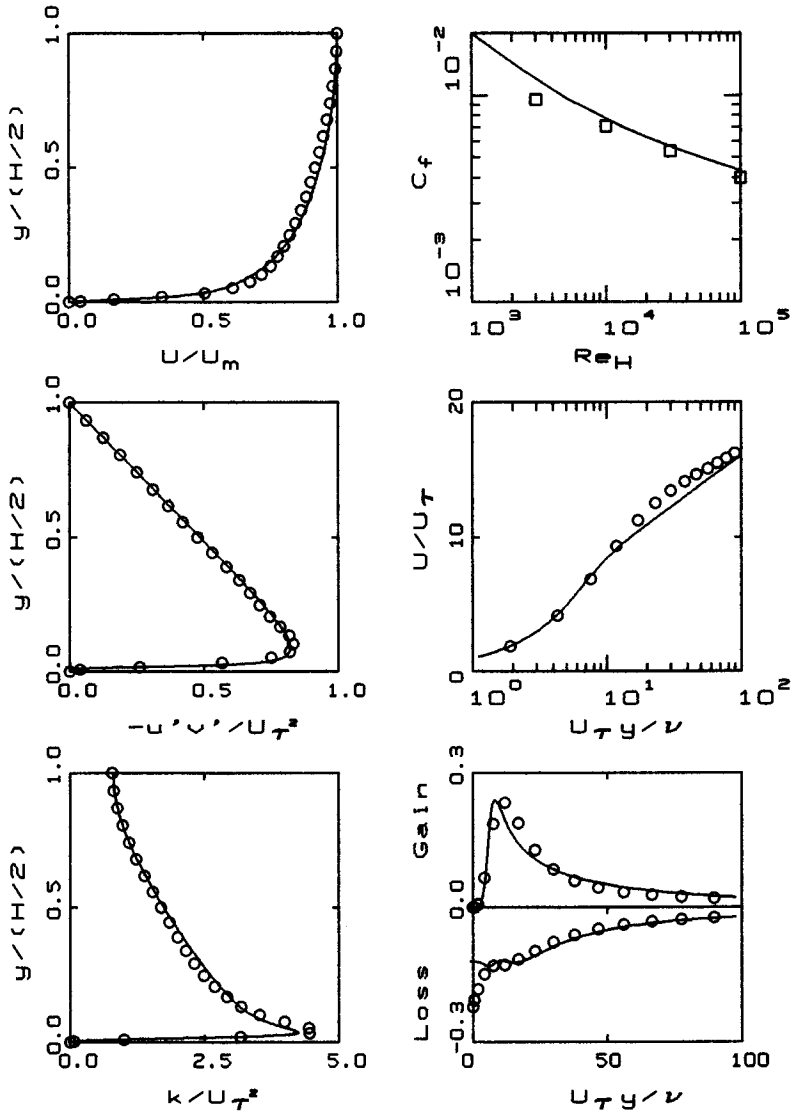


Figure 4.23: Comparison of computed and measured channel-flow properties, $Re_H = 13,750$. —— Low-Reynolds-number $k$-$\omega$ model; o Mansour et al. (DNS); □ Halleen-Johnston correlation.

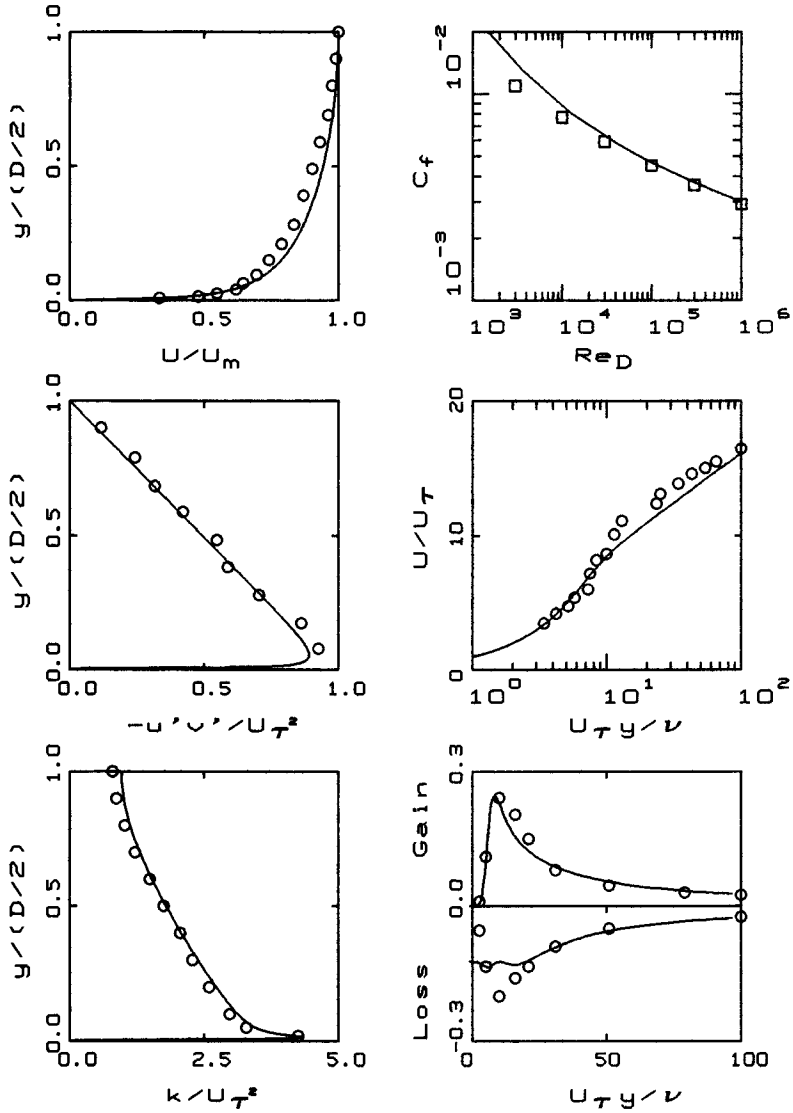


Figure 4.24: Comparison of computed and measured pipe-flow properties, $Re_D = 40,000$. —— Low-Reynolds-number $k$-$\omega$ model; ○ Laufer; □ Prandtl correlation.

free shear flows, the $k$-$\omega$ model's sensitivity to the freestream value of $\omega$ is a **desirable** feature for transition applications. Physical transition location is not simply a function of $T'$, but rather is frequency dependent. While it is unclear how the freestream value of $\omega$ should be specified, consistent with measurements, the model is not confined to a single transition location for a given $T'$ regardless of the frequency of the disturbance.

Figure 4.26 compares computed width of the transition region with measurements of Dhawan and Narasimha (1958), Schubauer and Skramstad (1948), and Fisher and Dougherty (1982). We define transition width, $\Delta x_t$, as the distance between minimum and maximum skin-friction points. The computed width, $Re_{\Delta x_t}$, falls within experimental data scatter for $10^4 < Re_{x_t} < 10^7$. $\Delta x_t$ is unaffected by the freestream value of $\omega$.

While these transition results are interesting, keep in mind that transition is a complicated phenomenon. Transition is triggered by a disturbance in a boundary layer only if the frequency of the disturbance falls in a specific band. Reynolds averaging has masked all spectral effects, and all the model can represent with $k$ and $\omega$ is the intensity of the disturbance and an average frequency. Hence, it is possible for the turbulence model to predict transition when it shouldn't occur. The model equations thus are sensible in the transition context only if the triggering disturbance is broad band, i.e., contains all frequencies.

Additionally, we have only guaranteed that the point where $k$ is first amplified matches the minimum critical Reynolds number for the incompressible, flat-plate boundary layer. To simulate transition with complicating effects such as pressure gradient, surface heat transfer, surface roughness, compressibility, etc., the values of $\alpha_o^*$ and $\alpha_o$ must change [see Wilcox (1977)]. Their values can be deduced from linear-stability theory results, or perhaps from a correlation based on stability theory. Nevertheless, some information must be provided regarding the minimum critical Reynolds number for each new application.

Perhaps the most practical way to use the model for transitional flows is in describing the transitional region. Of course, the question of sensitivity to spectral effects in the transition region must be raised. Using linear-stability computations, Wilcox (1981a) shows that after the initial disturbance has grown to a factor of $e^4$ times its initial value, the turbulence model closure coefficients lose all memory of spectral effects. Thus, we can conclude that not far downstream of the minimum critical Reynolds number, Reynolds averaging is sensible.

As a final comment regarding low-Reynolds-number corrections for two-equation turbulence models, note that the complexity of the model increases significantly. The Standard $k$-$\omega$ model has just 5 closure coefficients. The low-Reynolds-number version described in this subsection has 10 closure

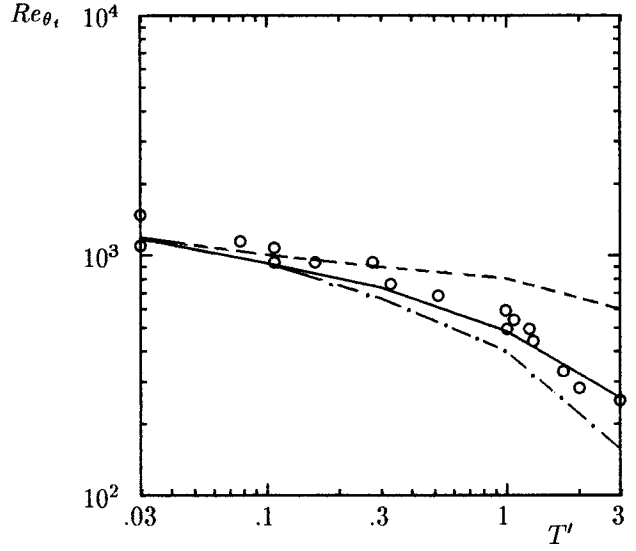


Figure 4.25: Transition location for an incompressible flat-plate boundary layer; - - - $\ell/\delta = .001$; —— $\ell/\delta = .010$; - · - $\ell/\delta = .100$; o Dryden.

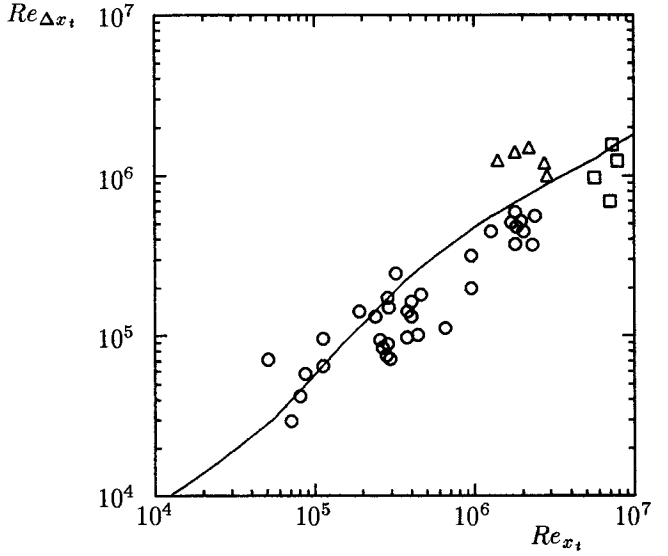


Figure 4.26: Transition width for an incompressible flat-plate boundary layer; —— $k$-$\omega$ model; o Dhawan-Narasimha; △ Schubauer-Skramstad; □ Fisher-Dougherty.

coefficients and 3 empirical damping functions. The various low-Reynolds-number models discussed in Subsection 4.9.1 involve a similar increase in the number of closure coefficients and damping functions. If viscous effects are insignificant for a given application, it is advisable to use the simpler high-Reynolds-number version of the model. In the case of the $k$-$\epsilon$ model, if you need to integrate through the viscous sublayer, you have no choice but to use one of the low-Reynolds-number models, preferably one that yields a satisfactory solution for simple flows such as the incompressible flat-plate boundary layer. In the case of the $k$-$\omega$ model, integration through the sublayer can be done without introducing the viscous corrections, and there is virtually no difference in model-predicted skin friction and velocity profiles with and without viscous corrections for boundary layers.

## 4.10 Separated Flows

Turning to separated flows, we first consider the axisymmetric flow with strong adverse pressure gradient that has been experimentally investigated by Driver (1991). Figure 4.27 compares Menter's (1992b) computed and measured skin friction and surface pressure for the $k$-$\omega$ model. As shown, the $k$-$\omega$ model yields results almost as close to measurements as those obtained with the Johnson-King model [see Figure 3.19], although pressure downstream of reattachment is somewhat higher than measured. Results are clearly much closer to measurements than those obtained with the Baldwin-Lomax and Baldwin-Barth models.

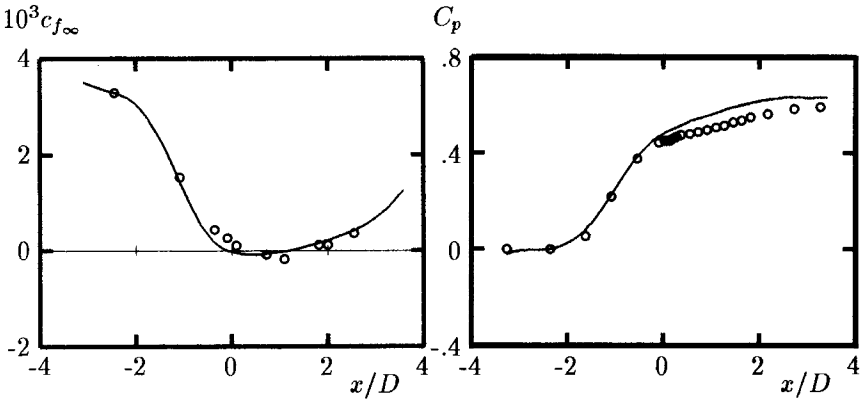


Figure 4.27: Computed and measured flow properties for Driver's separated flow; —— $k$-$\omega$ model; o Driver.

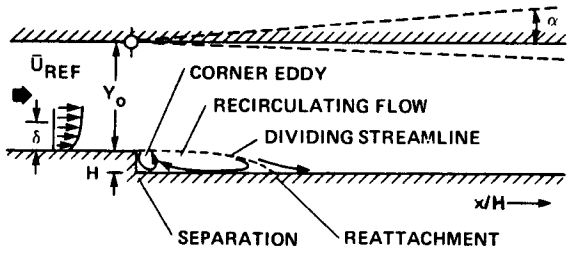


TUNNEL GEOMETRY: H = 1.27 cm, $Y_o$ = 8H
TUNNEL SPAN: 12H
TOP-WALL ANGLES: $-2^\circ \leq \alpha \leq 10^\circ$

INLET CONDITIONS: $U_{REF}$ = 44.2 m/sec, $M_{REF}$ = 0.128
$\delta_{BL}$ = 1.9 cm, $Re_\theta$ = 5000

Figure 4.28: Backward-facing step flow geometry and inlet conditions for the Driver-Seegmiller (1985) experiments. [From Driver and Seegmiller (1985) — Copyright © AIAA 1985 — Used with permission.]

The backward-facing step (Figure 4.28) is a popular test case for turbulence models because the geometry is simple. Additionally, separation occurs at the sharp corner so the flow is easier to predict than a flow for which the separation point is unknown a priori. Figure 4.29 compares computed and measured [Driver and Seegmiller (1985)] skin friction for backstep flow with the upper channel wall inclined to the lower wall at 0° and 6°. Computed results are shown for the Standard $k$-$\omega$ model and for the Standard $k$-$\epsilon$ model with wall functions; neither model includes viscous corrections. As summarized in Table 4.6, the $k$-$\epsilon$ model predicts reattachment well upstream of the measured point for both cases, while the $k$-$\omega$ model is within 3% of the measured location for both cases.

Table 4.6: Backstep Reattachment Length

| Model | Reference | $\alpha = 0°$ | $\alpha = 6°$ |
|---|---|---|---|
| $k$-$\epsilon$ | Launder-Sharma (1974) | 5.20 | 5.50 |
| $k$-$\omega$ | Wilcox (1988a) | 6.40 | 8.45 |
| Measured | Driver-Seegmiller (1985) | 6.20 | 8.10 |

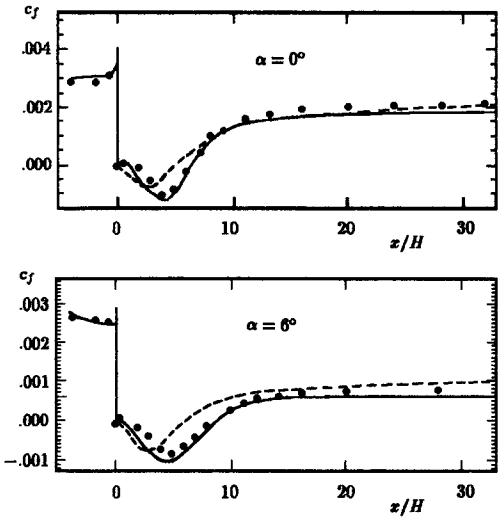


Figure 4.29: Computed and measured skin friction for flow past a backward-facing step; —— $k$-$\omega$ model; - - - $k$-$\epsilon$ model; • Driver-Seegmiller data. [Partially taken with permission from Menter (1992c).]

Many researchers have proposed modifications to the $k$-$\epsilon$ model aimed at improving its predictions for this flow. Driver and Seegmiller (1985), for example, compare four different versions of the model with their experimental data. We will discuss some of the proposed fixes for the $k$-$\epsilon$ model in Chapter 6. By contrast, the $k$-$\omega$ model's solution for flow past the backward-facing step is satisfactory with no special modifications.

Han (1989) has applied the $k$-$\epsilon$ model with wall functions to flow past a simplified three-dimensional bluff body with a ground plane. The object considered is known as Ahmed's body [Ahmed et al. (1984)] and serves as a simplified automobile-like geometry. In his computations, Han considers a series of afterbody slant angles. Figure 4.30(a) illustrates the shape of Ahmed's body with a 30° slant angle afterbody. Figure 4.30(b) compares computed and measured surface pressure contours on the rear-end surface for a 12.5° slant angle. As shown, computed pressure contours are similar on the slanted surface, but quite different on the vertical base. For slant angles up to 20°, the computed base pressures are significantly lower than measured. Consequently, the computed drag coefficient is about 30% higher than measured. Considering how poorly the $k$-$\epsilon$ model performs for

boundary layers in adverse pressure gradient and for the two-dimensional backward-facing step, it is not surprising that the model would predict such a large difference from the measured drag in this extremely complicated three-dimensional, massively-separated flow.

This is a quintessential example of how important turbulence modeling is to Computational Fluid Dynamics. Recall that there are three key elements to CFD, viz., the numerical algorithm, the grid and the turbulence model. Han uses an efficient numerical procedure and demonstrates grid convergence of his solutions. Han's computational tools also include state-of-the-art grid-generation procedures. Han's research efforts on this problem are exemplary on both counts. However, using the $k$-$\epsilon$ model undermines the entire computation for the following reasons. Because the model fails to respond in a physically realistic manner to the adverse pressure gradient on the read-end surface, the predicted skin friction is too high. This means the vorticity at the surface is too large, so that too much vorticity diffuses from the surface. This vorticity is swept into the main flow and too strong a vortex forms when the flow separates. This, of course, reduces the base pressure. Thus, the $k$-$\epsilon$ model's inability to accurately respond to adverse pressure gradient distorts the entire flowfield.

## 4.11 Range of Applicability

Turbulence-energy equation models include both **incomplete** one-equation models and **complete** two-equation models. As discussed in Section 4.2, only a modest advantage is gained in using a one-equation model rather than an algebraic model. The primary difficulty is the need to specify the length scale for each new application. There is no natural way to accommodate an abrupt change from a wall-bounded flow to a free shear flow such as near an airfoil trailing edge or beyond the trunk lid of an automobile. The only real advantage of using a one-equation model rather than a two-equation model stems from the relative difficulty often encountered in solving the model equations numerically. One-equation models tend to be nearly as well behaved as algebraic models. By contrast, two-equation models, especially the $k$-$\epsilon$ model, are often very difficult to solve. However, the user must establish his or her priorities on a key issue. Specifically, the user must decide if it is more desirable to have an easy-to-implement, inaccurate model, or a more-difficult-to-implement, accurate model. Those preferring the latter should probably select a two-equation model.

Certainly the $k$-$\epsilon$ model is the most widely used two-equation model. It has been applied to many flows with varying degrees of success. Unfortunately, it is inaccurate for flows with adverse pressure gradient and

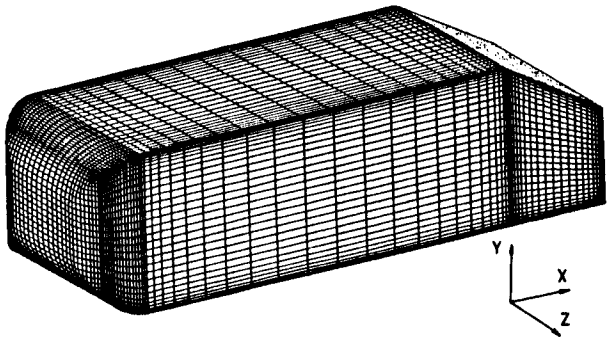


(a) Body geometry and surface grid

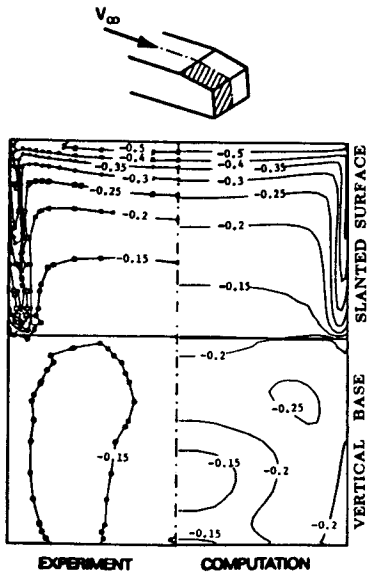


(b) Static-pressure contours

Figure 4.30: Flow past Ahmed's body. [From Han (1989) — Copyright © AIAA 1989 — Used with permission.]

that poses a serious limitation to its general utility. The model is also extremely difficult to integrate through the viscous sublayer and requires viscous corrections to simply reproduce the law of the wall for an incompressible flat-plate boundary layer. No consensus has been achieved on the optimum form of the viscous corrections as evidenced by the number of researchers who have created low-Reynolds-number versions of the model (see Subsection 4.9.1). While the model can be fine tuned for a given application, it is not clear that this represents an improvement over algebraic models. The primary shortcoming of algebraic models is their need of fine tuning for each new application. While saying the $k$-$\epsilon$ model always needs such fine tuning would be a bit exaggerated, it still remains that such tuning is too often needed.

The $k$-$\omega$ model, although not as popular as the $k$-$\epsilon$ model, enjoys several advantages. Most importantly, the model is very accurate for two-dimensional boundary layers with variable pressure gradient (both adverse and favorable). Also, without any special viscous corrections, the model can be easily integrated through the viscous sublayer. Finally, for the limited cases tried to date, the model appears to match measured properties of recirculating flows with no changes to the basic model and its closure coefficients. With viscous corrections included, the $k$-$\omega$ model accurately reproduces subtle features of turbulence kinetic energy behavior close to a solid boundary and even describes boundary-layer transition reasonably well. The only weakness of the $k$-$\omega$ model appears to be its sensitivity to freestream boundary conditions for free shear flows. While the $k$-$\epsilon$ model does not share this sensitivity, its predicted spreading rate matches measurements only for the plane jet.

Other two-equation models have been created, but they have had even less use than the $k$-$\omega$ model. Before such models can be taken seriously, they should be tested for simple incompressible boundary layers with adverse pressure gradient. How many interesting flows are there, after all, with constant pressure?

While two-equation models, especially the $k$-$\omega$ model, are far more general than less complex models, they nevertheless fail in some applications. In Chapter 5, we will see that these models are unreliable for boundary-layer separation induced by interaction with a shock wave. In Chapter 6, we will see that two-equation models are inaccurate for flows over curved surfaces. Also, two-equation models as presented in this chapter cannot predict secondary motions in noncircular duct flow. In all three of these examples, the difficulty can be traced to the Boussinesq eddy-viscosity approximation.

# Problems

**4.1** Verify that the exact equation for the dissipation, $\epsilon$, is given by Equation (4.39). That is, derive the equation that follows from taking the following moment of the Navier-Stokes equation.

$$\overline{2\nu \frac{\partial u_i'}{\partial x_j} \frac{\partial}{\partial x_j} [\mathcal{N}(u_i)]} = 0$$

where $\mathcal{N}(u_i)$ is the Navier-Stokes operator defined in Equation (2.26).

**4.2** Starting with Equations (4.4) and (4.39), define $\epsilon = \beta^* \omega k$ and derive an "exact" $\omega$ equation.

**4.3** Derive the exact equation for the **enstrophy**, $\omega^2$, defined by

$$\omega^2 \equiv \frac{1}{2}\overline{\omega_i' \omega_i'} \quad \text{where} \quad \omega_i' = \epsilon_{ijk} \partial u_k' / \partial x_j$$

That is, $\omega_i'$ is the fluctuating vorticity. **HINT:** First derive the equation for the vorticity, multiply by $\omega_i'$, and time average.

**4.4** We wish to create a new two-equation turbulence model. Our first variable is turbulence kinetic energy, $k$, while our second variable is the "eddy acceleration," $a$. Assuming $a$ has dimensions (length)/(time)$^2$, use dimensional arguments to deduce plausible algebraic dependencies of eddy viscosity, $\nu_T$, turbulence energy dissipation rate, $\epsilon$, and turbulence length scale, $\ell$, upon $k$ and $a$.

**4.5** Beginning with the $k$-$\omega$ model and with $\sigma = \sigma^*$, make the formal change of variables $\epsilon = \beta^* \omega k$ and derive the implied $k$-$\epsilon$ model. Express your final results in standard $k$-$\epsilon$ model notation and determine the implied values for $C_\mu$, $C_{\epsilon 1}$, $C_{\epsilon 2}$, $\sigma_k$ and $\sigma_\epsilon$ in terms of $\alpha$, $\beta$, $\beta^*$, $\sigma$ and $\sigma^*$.

**4.6** Beginning with the $k$-$\epsilon$ model, make the formal change of variables $\epsilon = C_\mu \omega k$ and derive the implied $k$-$\omega$ model. Express your final results in standard $k$-$\omega$ model notation and determine the implied values for $\alpha$, $\beta$, $\beta^*$, $\sigma$ and $\sigma^*$ in terms of $C_\mu$, $C_{\epsilon 1}$, $C_{\epsilon 2}$, $\sigma_k$ and $\sigma_\epsilon$.

**4.7** Simplify the $k$-$\epsilon$, $k$-$k\ell$, $k$-$k\tau$ and $k$-$\tau$ models for homogeneous, isotropic turbulence. Determine the asymptotic decay rate for $k$ as a function of the closure coefficient values quoted in Equations (4.43), (4.49), (4.56) and (4.59). Make a table of your results and include the decay rate of $t^{-1.20}$ for the $k$-$\omega$ model. (**NOTE:** You can ignore the $(\ell/y)^6$ contribution to $C_{L2}$ for the $k$-$k\ell$ model.)

**4.8** Simplify the $k$-$\epsilon$, $k$-$k\ell$, $k$-$k\tau$ and $k$-$\tau$ models for the log layer. Determine the value of Kármán's constant, $\kappa$, implied by the closure coefficient values quoted in Equations (4.43), (4.49), (4.56) and (4.59). Make a table of your results and include the value 0.41 for the $k$-$\omega$ model. **NOTE:** For all models, assume a solution of the form $dU/dy = u_\tau/(\kappa y)$, $k = u_\tau^2/\sqrt{C_\mu}$ and $\nu_T = \kappa u_\tau y$. Also, $C_\mu = C_D$ for the $k$-$k\ell$ model.

**4.9** Beginning with Equations (4.73), derive the self-similar form of the $k$-$\omega$ model equations for the mixing layer between a fast stream moving with velocity $U_1$ and a slow stream with velocity $U_2$.

(a) Assuming a streamfunction of the form $\psi(x, y) = U_1 x F(\eta)$, transform the momentum equation, and verify that $\mathcal{V}$ is as given in Table 4.1.

(b) Transform the equations for $k$ and $\omega$.

(c) State the boundary conditions on $\mathcal{U}$ and $K$ for $|\eta| \to \infty$ and for $\mathcal{V}(0)$. Assume $k \to 0$ as $|y| \to \infty$.

(d) Verify that if $\omega \neq 0$ in the freestream, the only boundary conditions consistent with the similarity solution are:

$$W(\eta) \to \begin{cases} \dfrac{1}{\beta}, & \eta \to +\infty \\ \dfrac{U_1/U_2}{\beta}, & \eta \to -\infty \end{cases}$$

**4.10** Exercise Programs WAKE, MIXER and JET (Appendix C) and verify the results quoted in Table 4.2. Cover the following ranges of values for WTIN:

| | |
|---|---|
| Far Wake | $10^{-6} \leq \text{WTIN} \leq 1$ |
| Mixing Layer | $10^{-6} \leq \text{WTIN} \leq 1$ |
| Plane Jet | $10^{-6} \leq \text{WTIN} \leq 10$ |
| Round Jet | $10^{-6} \leq \text{WTIN} \leq 100$ |

**4.11** Derive Equation (4.118).

**4.12** Demonstrate the integral constraint on the defect-layer solution, Equation (4.124).

**4.13** Determine the shape factor to $O(u_\tau/U_e)$ according to the defect-layer solution. Express your answer in terms of an integral involving $U_1(\eta)$.

**4.14** For the $k$-$\omega$ model, very close to the surface and deep within the viscous sublayer, dissipation balances molecular diffusion in the $\omega$ equation. Assuming a solution of the form $\omega = \omega_w/(1+Ay)^2$, solve this equation for $\omega = \omega_w$ at $y = 0$. Determine the limiting form of the solution as $\omega_w \to \infty$.

**4.15** Consider a flow with freestream velocity $U_\infty$ past a wavy wall whose shape is

$$y = \frac{1}{2} k_R \sin\left(\frac{2\pi x}{N k_R}\right)$$

where $k_R$ is the peak to valley amplitude and $Nk_R$ is wavelength. The linearized incompressible solution valid for $N \gg 1$ is $U = U_\infty + u'$, $V = v'$ where

$$u' = \frac{\pi U}{N} \exp\left(-\frac{2\pi y}{N k_R}\right) \sin\left(\frac{2\pi y}{N k_R}\right)$$

$$v' = \frac{\pi U}{N} \exp\left(-\frac{2\pi y}{N k_R}\right) \cos\left(\frac{2\pi y}{N k_R}\right)$$

Making an analogy between this linearized solution and the fluctuating velocity field in a turbulent flow, compute the specific dissipation rate, $\omega = \epsilon/(\beta^* k)$. Ignore contributions from the other fluctuating velocity component, $w'$.

**4.16** Using Program SUBLAY (Appendix C), determine the variation of the constant $B$ in the law of the wall for the $k$-$\omega$ model with the surface value of $\omega$. Do your computations with ($nvisc = 0$) and without ($nvisc = 1$) viscous modifications. Let $\omega_w^+$ assume the values 1, 3, 10, 30, 100, 300, 1000 and $\infty$. Be sure to use the appropriate value for input parameter *iruff*. Present your results in tabular form.

**4.17** Consider incompressible Couette flow with constant pressure, i.e., flow between two parallel plates separated by a distance $H$, the lower at rest and the upper moving with constant velocity $U_w$.

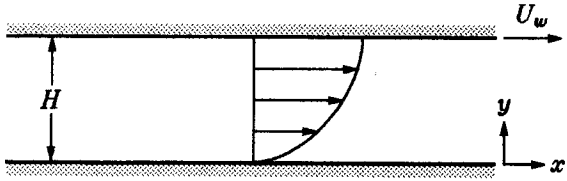

(a) Assuming the plates are infinite in extent, simplify the conservation of mass and momentum equations and verify that

$$(\nu + \nu_T)\frac{dU}{dy} = u_\tau^2$$

(b) Now ignore molecular viscosity. What boundary condition on $U$ is appropriate at the lower plate?

(c) Introducing the mixing length given by

$$\ell_{mix} = \kappa y(1 - y/H)$$

solve for the velocity across the channel. **HINT: Using partial fractions:**

$$\frac{1}{y(1-y/H)} = \frac{1}{y} + \frac{1}{(H-y)}$$

**Don't forget to use the boundary condition stated in Part (b).**

(d) Develop a relation between friction velocity, $u_\tau$, and the average velocity,

$$U_{avg} = \frac{1}{H}\int_0^H U(y)\, dy$$

(e) Using the $k$-$\omega$ model, simplify the equations for $k$ and $\omega$ with the same assumptions made in Parts (a) and (b).

(f) Deduce the equations for $k$ and $\omega$ that follow from changing independent variables from $y$ to $U$ so that

$$\nu_T \frac{d}{dy} = u_\tau^2 \frac{d}{dU}$$

(g) Assuming $k = u_\tau^2/\sqrt{\beta^*}$, simplify the equation for $\omega$. NOTE: You might want to use the fact that $(\beta - \alpha\beta^*) = \sigma\sqrt{\beta^*}\kappa^2$.

**4.18** For incompressible, laminar Couette flow, we know that the velocity is given by

$$U = U_w \frac{y}{H}$$

where $U_w$ is the velocity of the moving wall, $y$ is distance form the stationary wall, and $H$ is the distance between the walls.

(a) What is the maximum Reynolds number,

$$Re_{H_c} = U_w H/\nu$$

at which the flow remains laminar according to the high-Reynolds-number version of the $k$-$\omega$ model? To arrive at your answer, you may assume that

$$\omega = \begin{cases} \dfrac{6\nu}{\beta y^2}, & 0 \le y \le H/2 \\ \dfrac{6\nu}{\beta(H-y)^2}, & H/2 \le y \le H \end{cases}$$

(b) Above what Reynolds number is $\omega$ amplified?

**4.19** This problem studies the effect of viscous-modification closure coefficients for the $k$-$\omega$ model using Program SUBLAY (Appendix C).

(a) Modify Subroutine START to permit inputting the values of $R_k$ and $R_\omega$ (program variables *rk* and *rw*). Determine the value of $R_\omega$ that yields a smooth-wall constant in the law of the wall, $B$, of 5.0 for $R_k = 4$, 6, 8, 10 and 20.

(b) Now make provision for inputting the value of $R_\beta$ (program variable *rb*). For $R_k = 6$, determine the value of $R_\omega$ that yields $B = 5.0$ when $R_\beta = 0$, 4, 8, and 12. Also, determine the maximum value of $k^+$ for each case.